

AD A O 49066

12  
B.S.

AD-E300 039

DNA 4275F

**FINAL REPORT ON AURORAL  
SIMULATION EFFECTS**  
HAES Report No. 62

UJ NO. \_\_\_\_\_  
DDC FILE COPY

Mission Research Corporation  
735 State Street  
Santa Barbara, California 93101

31 March 1977

Final Report for Period 1 November 1975—31 March 1977

CONTRACT No. DNA 001-76-C-0138

APPROVED FOR PUBLIC RELEASE;  
DISTRIBUTION UNLIMITED.

THIS WORK SPONSORED BY THE DEFENSE NUCLEAR AGENCY  
UNDER RDT&E RMSS CODE B322076462 L25AAXYX96629 H2590D.

Prepared for  
Director  
DEFENSE NUCLEAR AGENCY  
Washington, D. C. 20305

DDC  
RECEIVED  
JAN 30 1978  
REGISTERED  
A

## **DISCLAIMER NOTICE**

**THIS DOCUMENT IS BEST QUALITY PRACTICABLE. THE COPY FURNISHED TO DTIC CONTAINED A SIGNIFICANT NUMBER OF PAGES WHICH DO NOT REPRODUCE LEGIBLY.**

Destroy this report when it is no longer  
needed. Do not return to sender.





UNCLASSIFIED

SECURITY CLASSIFICATION OF THIS PAGE(When Data Entered)

20. ABSTRACT (Continued)

calculations. These comparisons, along with those from earlier studies, are used to draw conclusions and recommendations related to IR modeling in the nuclear environment.

A new and more accurate procedure for calculating electron temperatures was devised and incorporated into the auroral code ARCTIC. The results were used, along with ion mass spectrometer measurements in an aurora, to infer enhanced values for the NO concentration.

UNCLASSIFIED

SECURITY CLASSIFICATION OF THIS PAGE(When Data Entered)

ACCESSION NO.	
NTIS	Write Section <input checked="" type="checkbox"/>
DOC	Off Section <input type="checkbox"/>
UNANNOUNCED	<input type="checkbox"/>
JUSTIFICATION	
BY	
DISTRIBUTION/AVAILABILITY CODES	
SIBL	AVAIL. AND OR SPECIAL
A	

PREFACE

The High Altitude Effects Simulation (HAES) Program sponsored by the Defense Nuclear Agency since the early 1970 time period, comprises several groupings of separate, but interrelated technical activities, e.g., ICECAP (Infrared Chemistry Experiments - Coordinated Auroral Program). Each of the latter have the common objective of providing information ascertained as essential for the development and validation of predictive computer codes designed for use with high priority DoD radar, communications, and optical defensive systems.

Since the inception of the HAES Program, significant achievements and results have been described in reports published by DNA, participating service laboratories, and supportive organizations. In order to provide greater visibility for such information and enhance its timely applications, significant reports published since early calendar 1974 shall be identified with an assigned HAES serial number and the appropriate activity acronym (e.g., ICECAP) as part of the report title. A complete and current bibliography of all HAES reports issued prior to and subsequent to HAES Report No. 1, dated 5 February 1974 entitled, "Rocket Launch of an SWIR Spectrometer into an Aurora (ICECAP 72)," AFCRL Environmental Research Paper No. 466, is maintained and available on request from DASIAC, DoD Nuclear Information and Analysis Center, 816 State Street, Santa Barbara, California 93102, Telephone (805) 965-0551.

This is the sixty second report in the HAES series and covers technical work performed under DNA contract 001-76-C-0138 from 1 November 1975 to 31 March 1977. The main purpose of the work reported herein is to

interpret and analyze data obtained from the ICECAP program so that models can be verified and/or constructed to describe the nuclear-disturbed environment.

We would like to acknowledge the full cooperation of numerous people involved in the ICECAP and EXCEDE programs and their aid in freely making available to us their data prior to its publication elsewhere. Special thanks go to Mr. James Ulwick, Dr. A. T. Stair, Mr. Ned Wheeler, Mr. Robert O'Neil, Mr. Philip Doyle (all of AFGL), Mr. Richard Hegblom (Boston College), Mr. William Grieder (Visidyne, Inc.), Dr. Irving Kofsky (Photometrics), Dr. Kay Baker (Utah State University), and Dr. Murray Baron (SRI). The encouragement of Dr. Charles Blank (DNA) is also appreciated.

## CONTENTS

	PAGE
PREFACE	1
LIST OF ILLUSTRATIONS	5
LIST OF TABLES	8
SECTION 1 INTRODUCTION	9
SECTION 2 AURORAL EVENT OF 12 MARCH 1975 (Sergeant Hydac IC 519.07-1B)	11
PRELIMINARY	11
QUALITATIVE DESCRIPTION OF EVENT	11
ARC AND EXO-ARC ENVIRONMENT	16
ARCTIC CODE CALCULATIONS	19
Model Flux and Environment	19
Results and Comparisons with Data	22
SUMMARY AND CONCLUSIONS	40
SECTION 3 AURORAL EVENT OF 10 MARCH 1975 (Nike Hydac IC 507.11-2A)	41
PRELIMINARY	41
ENERGY DEPOSITION	42
COMPARISONS WITH DATA IN 5.3- $\mu$ m BAND	42
SUMMARY AND COMMENTS	48
SECTION 4 CODE CALCULATION OF THE ELECTRON TEMPERATURE	49
PRELIMINARY	49
HEATING AND COOLING RATES	49
OLD SOLUTION TO EQUATION 4-1	51
NEW SOLUTION TO EQUATION 4-1	53

	HEATING BY N( <sup>2</sup> D) QUENCHING	57
	COMPARISONS WITH SRI RADAR DATA	58
SECTION 5	NO IN THE AURORAL ENVIRONMENT	62
	PRELIMINARY	62
	[NO] INFERRED FROM SLOPE OF 5.3- $\mu$ m ZENITH INTENSITY PROFILES	62
	[NO] INFERRED FROM ION MASS SPECTROMETER MEASUREMENTS	66
	SUMMARY	69
SECTION 6	ICECAP SUMMARY AND CONCLUSIONS	70
	PRELIMINARY	70
	PRINCIPAL RESULTS	71
	5.3- $\mu$ m Radiation	72
	2.7- $\mu$ m Radiation	74
	4.3- $\mu$ m Radiation	75
	NO Concentration	76
	IMPLICATIONS TO THE NUCLEAR ENVIRONMENT	76
SECTION 7	COMMUNICATIONS RELATED WORK	78
	INTRODUCTION	78
	AURORAL IONIZATION EFFECTS DUE TO STRUCTURED PARTICLE FLUXES	79
	ELECTRON BEAM EXCITATION OF F-REGION ATOMIC OXYGEN	80
	Deposition and Partition by 325 eV Electrons at 300-km Altitude	80
	Conclusion	86
	REFERENCES	87
APPENDIX A	PARTITION OF ELECTRON ENERGY ( $\geq$ 1 keV) IN ATMOSPHERIC GASES	A-1
APPENDIX B	PARTITION OF ELECTRON ENERGY ( $\leq$ 25 eV) IN ATMOSPHERIC GASES	B-1
APPENDIX C	ON OPTICAL MEASUREMENT OF AURORAL NO PROFILES	C-1

## ILLUSTRATIONS

FIGURE		PAGE
2-1.	Energy flux inferred from three complete meridian scans of 4278Å photometer at Chatanika, Alaska.	13
2-2.	Energy flux data (scintillator; $E > 4$ keV); Sergeant Hydac IC 519.07-1B.	14
2-3.	Pictorial representation in magnetic meridian plane showing rocket (IC 519.07-1B) trajectory and approximate location of arc complex.	15
2-4.	Energy deposition rate during and prior to flight of Multi rocket IC 519.07-1B, as inferred from Lockheed's three-beam photometer.	17
2-5.	Measured electron flux inside and outside arc complex corresponding to positions shown in Figure 2-2.	18
2-6.	Incident electron flux assumed for arc complex of 12 March 1975 (Sergeant Hydac IC 519.07-1B).	20
2-7.	Calculated energy deposition rate in auroral arc (Sergeant Hydac IC 519.07-1B).	23
2-8.	Calculated volume emission rates in auroral arc of 12 March 1975 (Sergeant Hydac IC 519.07-1B).	24
2-9.	Electron density along rocket (IC 519.07-1B) trajectory inferred from SRI radar data.	25
2-10.	Zenith radiance at 3914Å (Sergeant Hydac IC 519.07-1B); data and theory compared.	27
2-11.	Calculated and observed zenith radiance in 5.3- $\mu$ m band (Sergeant Hydac IC 519.07-1B).	29
2-12.	Calculated CVF spectrometer spectrum for the (1,0) band of NO at 250 °K.	32

FIGURE		PAGE
2-13.	Typical CVF spectrometer feature near 5.3 $\mu\text{m}$ (from rocket IC 519.07-1B) compared with the theoretical (1,0) band spectrum of NO at 250 $^{\circ}\text{K}$ .	33
2-14.	Observed zenith radiance near 4.3 $\mu\text{m}$ compared with calculated CO <sub>2</sub> emission (Sergeant Hydac IC 519.07-1B).	35
2-15.	Possible contribution of NO <sup>+</sup> chemiluminescence to observed emission in radiometer band near 4.3 $\mu\text{m}$ .	38
3-1.	Measured electron density and inferred energy deposition rate profiles for auroral event of 10 March 1975.	43
3-2.	Calculated volume emission rate near 5.3 $\mu\text{m}$ from NO chemiluminescence for auroral event of 10 March 1975.	44
3-3.	Measured 5.3- $\mu\text{m}$ band emission compared with calculated NO chemiluminescence for 10 March 1975 auroral event (IC 507.11-2A).	46
4-1.	Behavior of $T_e$ and $T_{ss}$ under approximations 4-9 and 4-10.	52
4-2.	Behavior of $T_e$ and $T_{ss}$ using Equation 4-12 and 4-13.	54
4-3.	Calculated electron temperature in '75 Multi arc as function of time for three different altitudes.	56
4-4.	Calculated electron temperature in '74 Multi drizzle as function of time for two different altitudes.	56
4-5.	Fraction, $f$ , of total electron heating rate at 194 km due to deexcitation of N(2D) after onset of '75 Multi arc flux.	59
4-6.	Electron temperature calculations compared with SRI radar data.	60
5-1.	Auroral NO concentrations inferred from slope of 5.3- $\mu\text{m}$ radiometer data.	65
5-2.	NO Concentration inferred from auroral data of 27 March 1973 (Rocket A18.205-1).	68
6-1.	Zenith peak spectral radiance (Paiute Tomahawk A10.205-2).	73

FIGURE		PAGE
7-1.	Depicting geometrical arrangement for viewing 6300Å emission from ground.	84
A-1.	Schematic illustration of the dependence of $P_e$ on $f_e$ .	A-11
A-2.	Calculated fractional energy deposited in electron gas as function of initial fractional ionization.	A-13
B-1.	Fraction of electron energy deposited in electron gas for parametric values of the fractional ionization in pure $N_2$ .	B-2
B-2.	Fraction of electron energy deposited in electron gas for parametric values of the fractional ionization in pure $O_2$ .	B-3
B-3.	Fraction of electron energy deposited in electron gas for parametric values of the fractional ionization in pure N.	B-4
B-4.	Fraction of electron energy deposited in electron gas for parametric values of the fractional ionization in pure O.	B-5
B-5.	Fraction of electron energy deposited in vibrational excitation of $N_2$ for zero fractional ionization.	B-7
B-6.	Fraction of electron energy deposited in vibrational excitation of $O_2$ for zero fractional ionization.	B-8
B-7.	Number of nitrogen atoms formed per electron deposited in $N_2$ gas.	B-9
B-8.	Number of oxygen atoms formed per electron deposited in $O_2$ gas.	B-10
B-9.	Number of $N(^2D)$ and $N(^2P)$ atoms formed per electron deposited in N gas.	B-11
B-10.	Number of $O(^1D)$ atoms formed per electron deposited in O gas.	B-12
C-1.	Calculated intensity in $5025\text{Å} \leq \lambda \leq 5075\text{Å}$ band.	C-7
C-2.	Calculated intensity in $5025\text{Å} \leq \lambda \leq 5075\text{Å}$ band.	C-8
C-3.	Calculated intensity in $4750\text{Å} \leq \lambda \leq 4850\text{Å}$ band.	C-9

## TABLES

TABLE		PAGE
2-1	Deposition atmosphere used for ARCTIC code calculations (Sergeant Hydac IC 519.07-1B).	21
6-1	Classification of auroral events studied.	71
7-1	Photon emission rate in various permitted lines of atomic oxygen at 300-km altitude by a 325 eV electron beam of unit ampere current.	82
7-2	Radiative recombination rate constants for the process $O^+ + e \rightarrow O + h\nu$ at $T_e = 2000^\circ\text{K}$ .	82
7-3	Computed airglow intensity for 200-km vertical path and selected values of ambient electron density.	83
7-4	Estimated intensity of 6300-Å emission excited by a 325 eV electron beam of unit ampere current at 300-km altitude.	86
A-1	Partition in a pure N <sub>2</sub> gas.	A-5
A-2	Partition in a pure O <sub>2</sub> gas.	A-6
A-3	Partition in a pure O gas.	A-7
A-4	Partition in a pure N gas.	A-7
B-1	Species formed in low energy electron deposition.	B-13
C-1	Fluorescence bands in two wavelength regions.	C-2

## SECTION 1 INTRODUCTION

This is the last in a series of reports describing work performed at Mission Research Corporation in support of DNA's field programs in Alaska, especially ICECAP and EXCEDE. It extends the analyses described before (References 1 through 4) by including the results of studies on two new auroral events, and presenting additional work related to the earlier events.

The main purpose of the work has been to understand and interpret the field data from an aurorally-excited atmosphere, especially data related to short wavelength infrared radiation (SWIR), so that better models could be constructed to describe the nuclear environment. In this endeavor, we have availed ourselves of ICECAP data from five different auroral events, and have made extensive use of the ARCTIC code that was devised specifically for auroral calculations and comparisons with the field data.

An attempt is made to summarize the main results and conclusions of our work, especially as it impacts on SWIR radiation processes, and to relate it to the nuclear environment.

Sections 2 and 3 describe results and conclusions from our study of the auroral events of 12 March 1975, and 10 March 1975, respectively.

Section 4 describes the modifications introduced into the ARCTIC code that are necessary for the correct calculation of the electron temperature.

Section 5 presents the results of our efforts to infer NO profiles for several different auroral events.

Section 6 contains a summary of the principal results of our analyses of five different auroral events.

Section 7 gives a brief discussion of work done in support of DNA's satellite communications effort, especially the Wideband Satellite experiment.

Three appendices are included. Appendices A and B are in support of Section 4, and give details related to the heating of the electron gas by high energy ( $\geq 1$  keV) and low energy ( $\leq 25$  eV) electrons, respectively. Appendix C describes a proposed method for measuring the NO concentration in an auroral environment.

SECTION 2  
AURORAL EVENT OF 12 MARCH 1975  
(Sergeant Hydac IC 519.07-1B)

PRELIMINARY

On 12 March 1975, at 0748:10 UT, a multi-instrumented Sergeant Hydac rocket (IC 519.07-1B) was launched from Poker Flat, Alaska into an active aurora, reaching an apogee of about 184 km at 225 sec after launch. On-board instrumentation that obtained data included particle detectors (scintillator, electrostatic analyzer), a CVF spectrometer (SWIR), vertical radiometers (4.3, 5.3  $\mu\text{m}$ ), a 3914Å photometer (vertical), 3914Å and 5577Å photometers (horizontal), and a mass spectrometer.

Ground-support data for the event were also obtained from All-Sky cameras, meridian scanning photometers, and the SRI incoherent backscatter radar.

The rocket data, along with what ground-support data we could assemble, were used as the basis for making an ARCTIC code calculation for the event. The following subsections give a brief description of the event, of the calculations, and of the comparisons with field data.

QUALITATIVE DESCRIPTION OF EVENT

The region traversed by the rocket was part of a system of arcs that originated north of Poker Flat (Reference 5), but within 20 minutes before the rocket launch had moved rapidly southward (Reference 6). Study of the Lockheed scanning photometer data taken at Chatanika (Reference 7),

the scintillator data, and the All-Sky camera pictures from Poker Flat, leads to the following qualitative picture of the event.

At the time of rocket launch, an arc complex was located approximately 40 km to the north of Poker Flat. The structure changed in width, appearance, and position as multiple arcs of varying intensities merged, decayed, reformed, etc. Figure 2-1 shows a piece of the data inferred from the Lockheed 4278Å meridian scanning photometer for the time interval spanning the rocket flight. The photometer scanned from north (N) through zenith (Z) to south (S) and back through zenith to north again in a repetitive pattern. The main arc complex is located a few degrees to the north of zenith in each scan. The times of rocket launch, apogee, and impact are indicated in the figure. The changing width, structure, and intensity of the arc complex are apparent in the seven times the structure was scanned in the sample shown in Figure 2-1.\*

Figure 2-2 shows particle data from the rocket-borne scintillator (Reference 8) that responded to flux from electrons with energy  $>4$  keV. Note the sharp increase in flux as the rocket ascended from 100- to 130-km altitude. We believe this occurred as the rocket penetrated the southern edge of the arc complex, reaching the intense inner arc at about 120 sec after launch. The smaller flux values at 100 km, however, are probably due partly to degradation of the incident flux at this lower altitude. As Figure 2-2 indicates, the flux of electrons with  $E > 4$  keV encountered by the rocket as it traversed the arc complex was quite irregular. Exit from the northern edge appears to have occurred near apogee and the rocket then descended through a region of low particle precipitation.

Figure 2-3 shows a pictorial representation of the rocket trajectory with superimposed arc complex, as inferred from the description above. The

---

\* In Figure 2-1 another strong arc can be seen north of Fort Yukon ( $70^\circ$  north from zenith at Chatanika (near Poker Flat)) at about 0753 UT.

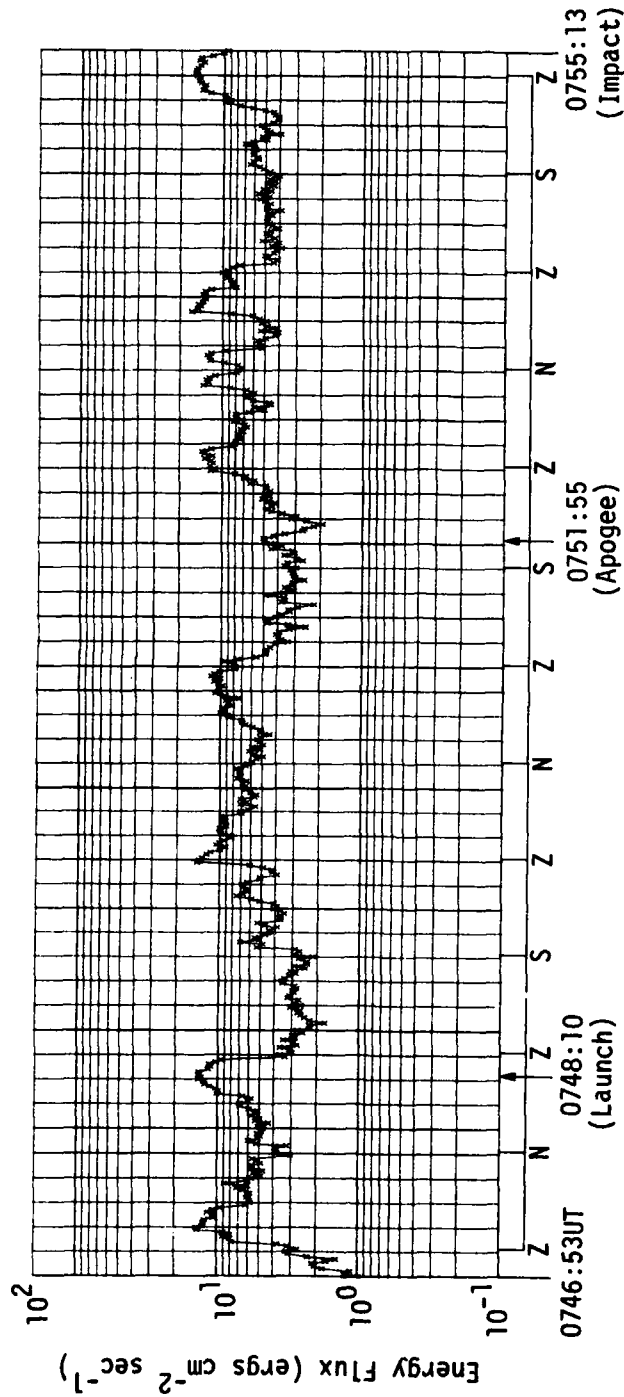


Figure 2-1. Energy flux inferred from three complete meridian scans of 4278A photometer at Chatanika, Alaska, during 500-sec time interval that spans flight of Multi rocket IC 519.07-1B. The symbols Z, N, S indicate, respectively, zenith pointing angles of the photometer of 0°, 80°(north), and 80°(south). Grid spacing on the abscissa represents 10 sec of time and 20° angular change in photometer pointing direction. (Data from Reference 9).

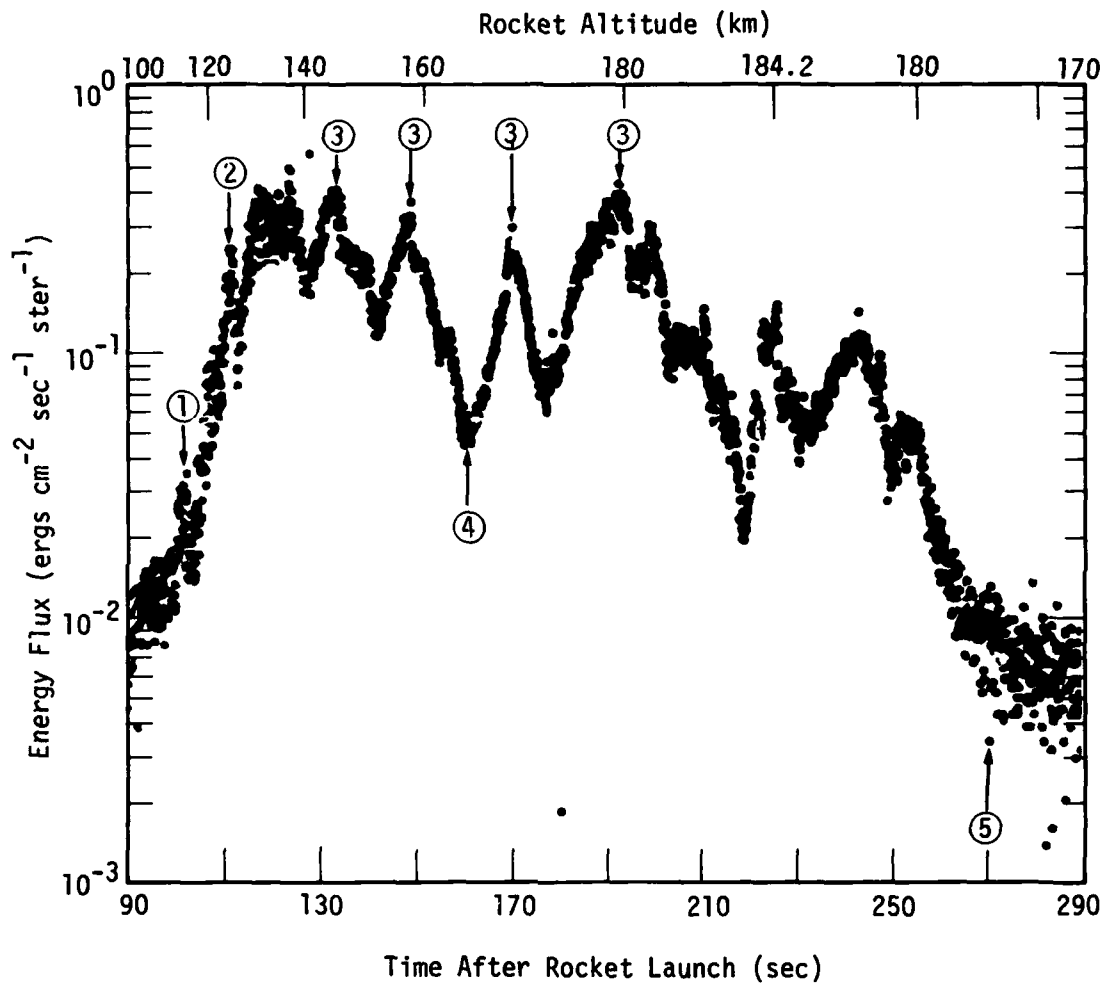


Figure 2-2. Energy flux data (scintillator;  $E > 4$  keV);  
Sergeant Hydac IC 519.07-1B (Reference 8).

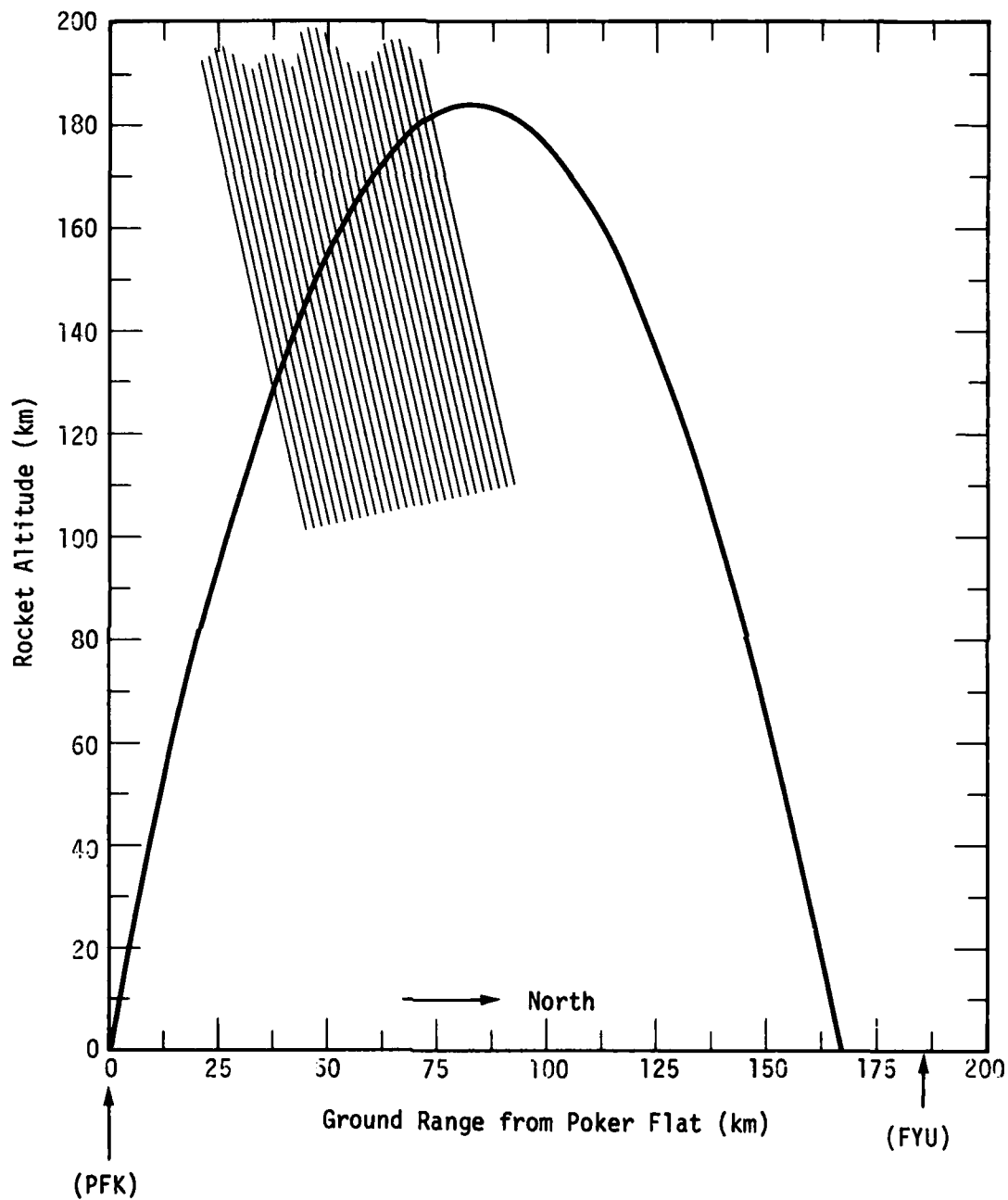


Figure 2-3. Pictorial representation in magnetic meridian plane showing rocket (IC 519.07-1B) trajectory and approximate location of arc complex.

location of Poker Flat (PKF) and Fort Yukon (FYU) are also shown. Precipitation occurred, of course, over the entire trajectory, but it was most intense in the region indicated in Figure 2-3.

Figure 2-4 (from Reference 9) shows the energy deposition rate due to electron precipitation and to Joule heating during and for about one hour prior to the rocket flight. The relatively low deposition rate is clearly evident until the arc system moved into the region after about 0740 UT. Predosing of the rocket airspace, therefore, would not seem to have been very significant.

#### ARC AND EXO-ARC ENVIRONMENT

A quantitative description of the arc system, including its north-south width and motion is difficult to obtain from the scanning photometer data available to us from Chatanika and Fort Yukon. Camera malfunction at Ester Dome precluded data from that station. Plots of peak intensity as functions of elevation angle obtained from the two stations lead to arc positions and motions that are not entirely consistent. However, if one assumes that the arc system was fairly stationary while the rocket traversed it, the scintillator data (Figure 2-2) implies that the system extended for approximately 50 km in the magnetic meridian plane. At the time of rocket traversal, its position is approximately as indicated in Figure 2-3.

The spectral flux of precipitated electrons with energy in the range from about 1 to 30 keV was measured with the rocket-borne electrostatic analyzer. Figure 2-5 shows several measured spectra corresponding to regions inside and outside the arc complex. The numbered spectra correspond to times and altitudes indicated on the scintillator plot in Figure 2-2. Thus, spectra ① and ② correspond to the region just south of the arc where the flux is lower; spectra ③ and ④ are typical of the flux at the maxima and minima, respectively, in the arc complex; and ⑤ was measured at 270 sec on the downleg of the trajectory in a region north of the arc system.

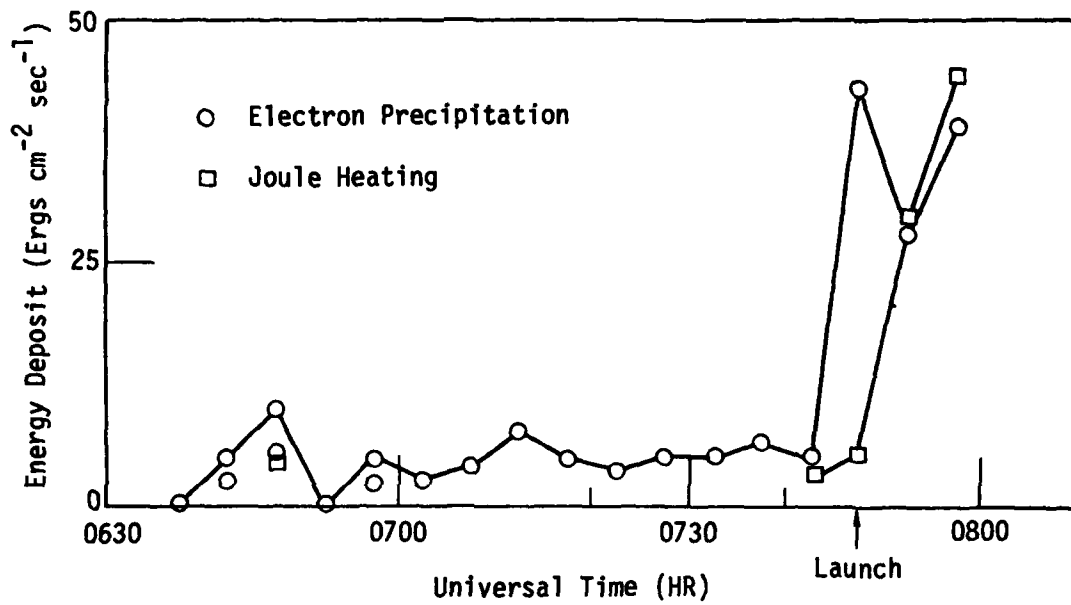


Figure 2-4. Energy deposition rate during and prior to flight of Multi rocket IC 519.07-1B, as inferred from Lockheed's three-beam photometer (Reference 9).

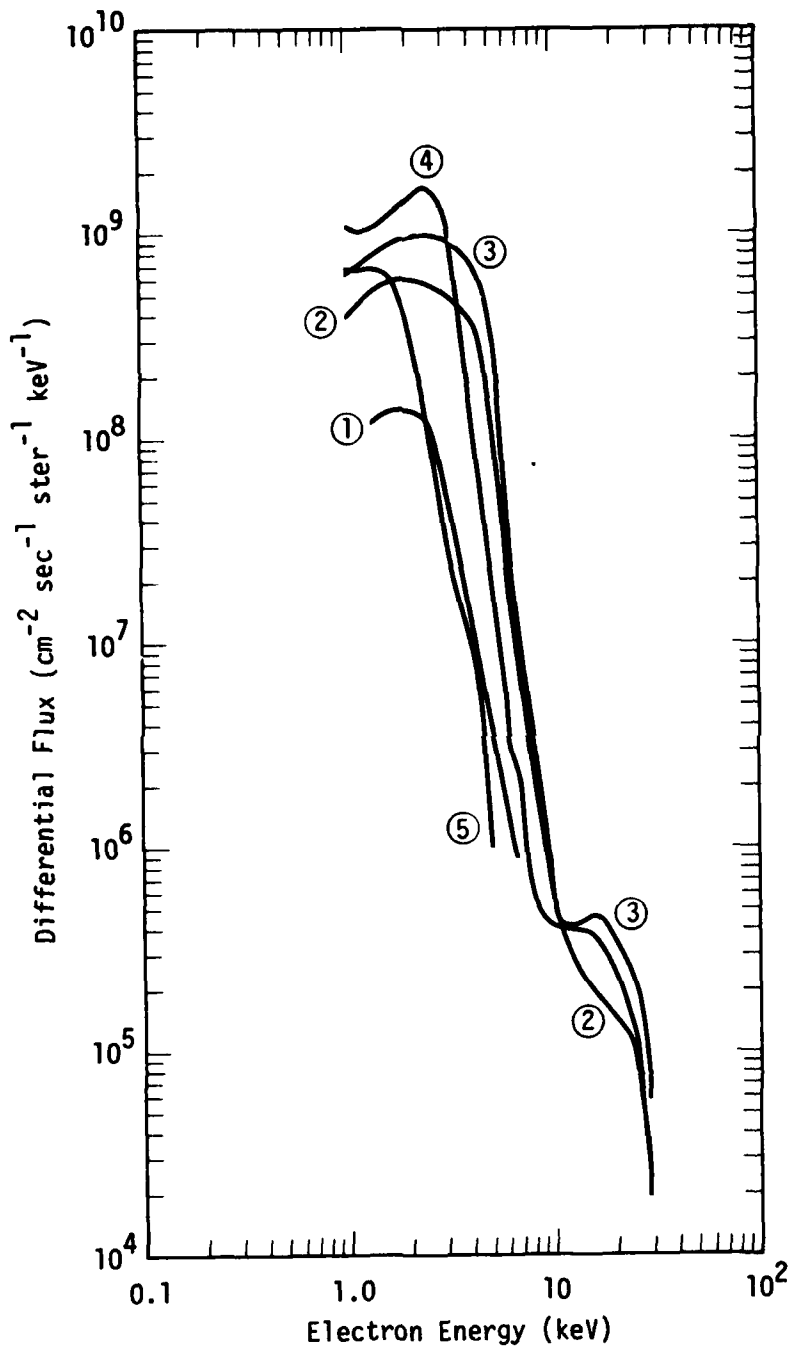


Figure 2-5. Measured electron flux inside and outside arc complex corresponding to positions shown in Figure 2-2 (Sergeant Hydac IC 519.07=1B) (from Reference 8).

## ARCTIC CODE CALCULATIONS

### Model Flux and Environment

As described in References 2 and 4, the procedure used in making previous ARCTIC code calculations has been to deposit the arc flux in a pre-dosed atmosphere resulting from 30 minutes of "drizzle" bombardment. The drizzle flux in turn was assumed to be deposited in an initial, high-latitude atmosphere that was described in Reference 2, p. 28.

In the present case it was felt that we had insufficient information to define adequately the drizzle flux. Consequently, the arc flux was deposited directly into the initial high-latitude atmosphere, and no attempt was made to calculate an exo-arc drizzle environment.

Figure 2-6 shows the electron flux spectrum input to the ARCTIC code. It is spectrum ③ from Figure 2-5 (corresponding to one measured at 132 sec when the rocket was at 145-km altitude on ascent) with an arbitrary extrapolation at the low energy end to 0.1 keV. Pitch-angle isotropy in the downward hemisphere has been assumed because this is consistent with the scintillator data over the range measured from about 33° to 77°. The energy input rate to the atmosphere from this spectrum is about  $52 \text{ ergs cm}^{-2} \text{ sec}^{-1}$ .

The energy was deposited in a grid of 25 cells extending in the vertical direction from 89- to 199-km altitude. Table 2-1 shows the assumed deposition atmosphere, with species concentrations in units of  $\text{cm}^{-3}$  and temperature (electron=neutral) in °K. The first two columns are: cell altitude (km), and cell thickness (km), respectively. The NO profile assumed is the high latitude one shown in Reference 2, Figure 2-11.

The energy deposition rate in the calculational volume between 89 and 199 km is  $41 \text{ ergs cm}^{-2} \text{ sec}^{-1}$ . Of the remaining  $11 \text{ ergs cm}^{-2} \text{ sec}^{-1}$ , part is deposited in the atmosphere above 199 km and the rest is backscattered to space.

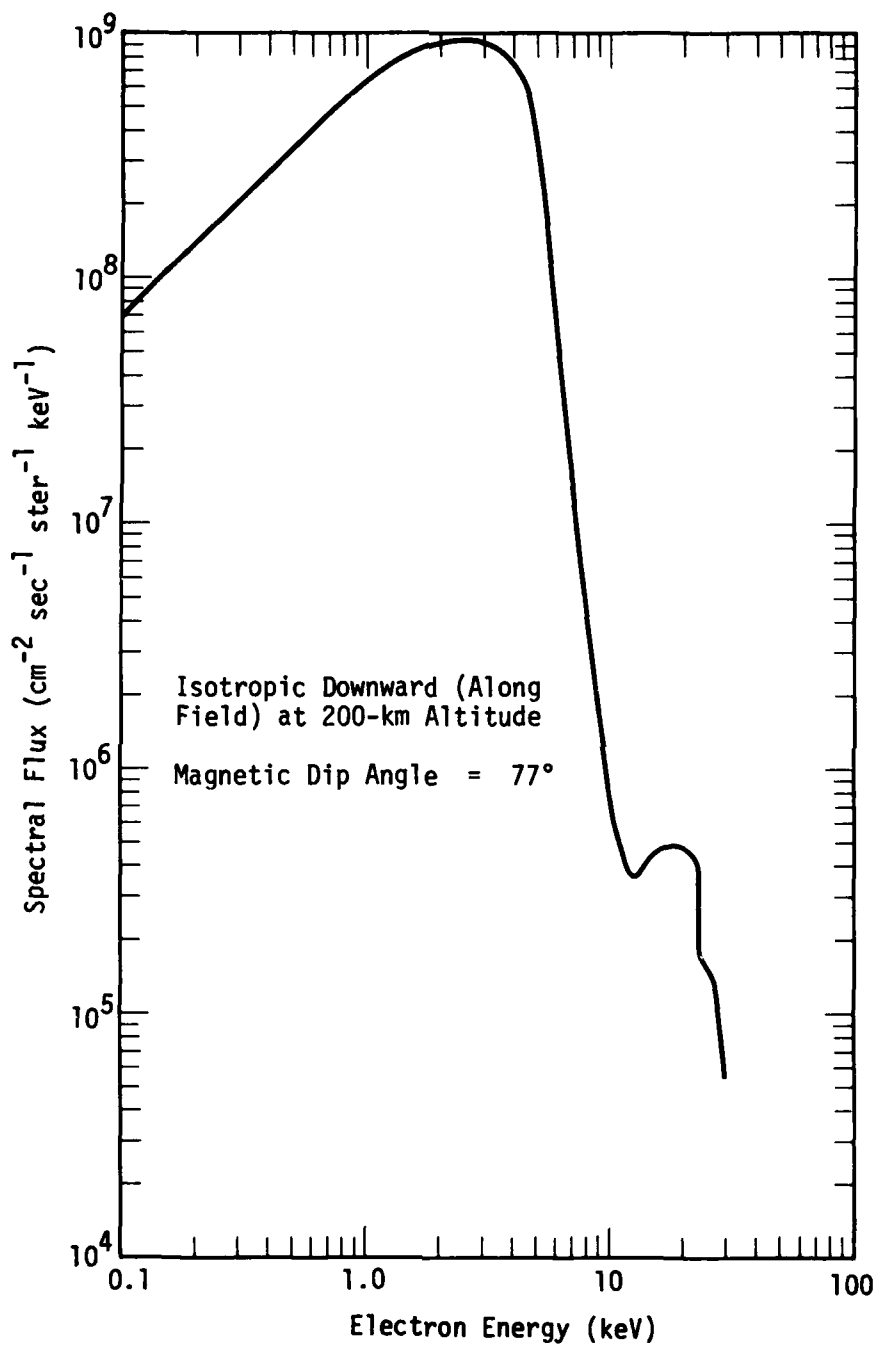


Figure 2-6. Incident electron flux assumed for arc complex of 12 March 1975 (Sergeant Hydac IC 519.07-1B).

Table 2-1. Deposition atmosphere used for ARCTIC code calculation.  
(Sergeant Hydac IC 519.07-1B).

h (cell center) (km)	$\Delta h$ (km)	$N_2$ ( $cm^{-3}$ )	$O_2$ ( $cm^{-3}$ )	$O$ ( $cm^{-3}$ )	$Ne$ ( $cm^{-3}$ )	$T = T$ ( $^{\circ}K$ ) <sup>e</sup>
90	2	$4.98^{13}$	$1.34^{13}$	$1.30^{11}$	$2.05^3$	186
92	2	$3.43^{13}$	$9.19^{12}$	$1.88^{11}$	$2.72^3$	191
94	2	$2.36^{13}$	$6.30^{12}$	$2.81^{11}$	$3.67^3$	196
96	2	$1.65^{13}$	$4.31^{12}$	$3.68^{11}$	$4.96^3$	200
98	2	$1.16^{13}$	$2.94^{12}$	$4.29^{11}$	$6.70^3$	204
100	2	$8.22^{12}$	$2.01^{12}$	$4.83^{11}$	$8.76^3$	208
102	2	$5.82^{12}$	$1.39^{12}$	$4.39^{11}$	$9.52^3$	216
104	2	$4.12^{12}$	$9.59^{11}$	$3.86^{11}$	$1.01^4$	225
106	2	$2.98^{12}$	$6.76^{11}$	$3.22^{11}$	$1.06^4$	233
108	2	$2.20^{12}$	$4.87^{11}$	$2.54^{11}$	$1.13^4$	242
110	2	$1.62^{12}$	$3.50^{11}$	$2.01^{11}$	$1.21^4$	251
113	3	$1.11^{12}$	$2.31^{11}$	$1.58^{11}$	$1.36^4$	277
116	3	$7.09^{11}$	$1.42^{11}$	$1.18^{11}$	$1.58^4$	308
119	4	$4.59^{11}$	$8.74^{10}$	$8.45^{10}$	$1.89^4$	345
123	4	$2.91^{11}$	$5.29^{10}$	$6.07^{10}$	$2.26^4$	398
127	4	$1.89^{11}$	$3.29^{10}$	$4.47^{10}$	$2.66^4$	454
132	5	$1.22^{11}$	$2.03^{10}$	$3.29^{10}$	$3.10^4$	513
137	5	$8.23^{10}$	$1.32^{10}$	$2.52^{10}$	$3.56^4$	567
142	5	$5.73^{10}$	$8.81^9$	$1.98^{10}$	$4.03^4$	617
147	5	$4.20^{10}$	$6.25^9$	$1.61^{10}$	$4.20^4$	658
154	10	$2.77^{10}$	$3.93^9$	$1.23^{10}$	$4.56^4$	712
164	10	$1.67^{10}$	$2.23^9$	$8.89^9$	$5.09^4$	770
174	10	$1.06^{10}$	$1.34^9$	$6.70^9$	$5.35^4$	814
184	10	$6.99^9$	$8.35^8$	$5.18^9$	$5.81^4$	848
194	10	$4.71^9$	$5.35^8$	$4.08^9$	$6.77^4$	876

The calculated energy partition and resulting production rates of species were input to the chemistry subroutine that was then run for times to 1800 sec. A great deal of output is obtained from each running of the code. Included are volume production rates of over 200 states of excitation, species concentrations and temperatures as functions of time, and volume production rates of photons in numerous optical and IR bands. However, only a small fraction of this output will be shown since most of it cannot be compared directly with field data.

#### Results and Comparisons with Data

The calculated energy deposition rate profile is shown in Figure 2-7. Due to the softness of the energy spectrum (see Figure 2-6), the peak of the deposition is seen to occur near the relatively high altitude of 120 km. The inflection point at 100-km altitude arises from the secondary peak in the electron flux spectrum at 20 keV.

Figure 2-8 shows selected volume emission rates calculated for the arc. The results for O, NO, and  $\text{NO}^+$  are applicable at both 100 sec and 1000 sec. Quenching of the 4.3- $\mu\text{m}$  emission from  $\text{NO}^+$  is not included.

#### ELECTRON DENSITY

Unfortunately, no electron density data from the rocket are available since both the plasma frequency probe and the retarding potential analyzer failed. The only direct ionization data we have are from the SRI incoherent backscatter radar that was in a meridian scan mode during the rocket flight. From the resulting electron density contour maps (Reference 6) we have inferred the ascent and descent profiles shown in Figure 2-9. Plotted, for comparison, is our calculated profile based on the arc spectrum shown in Figure 2-6. Agreement between the calculated and measured (ascent) profiles is seen to be good up to 120 km, but the two curves diverge above

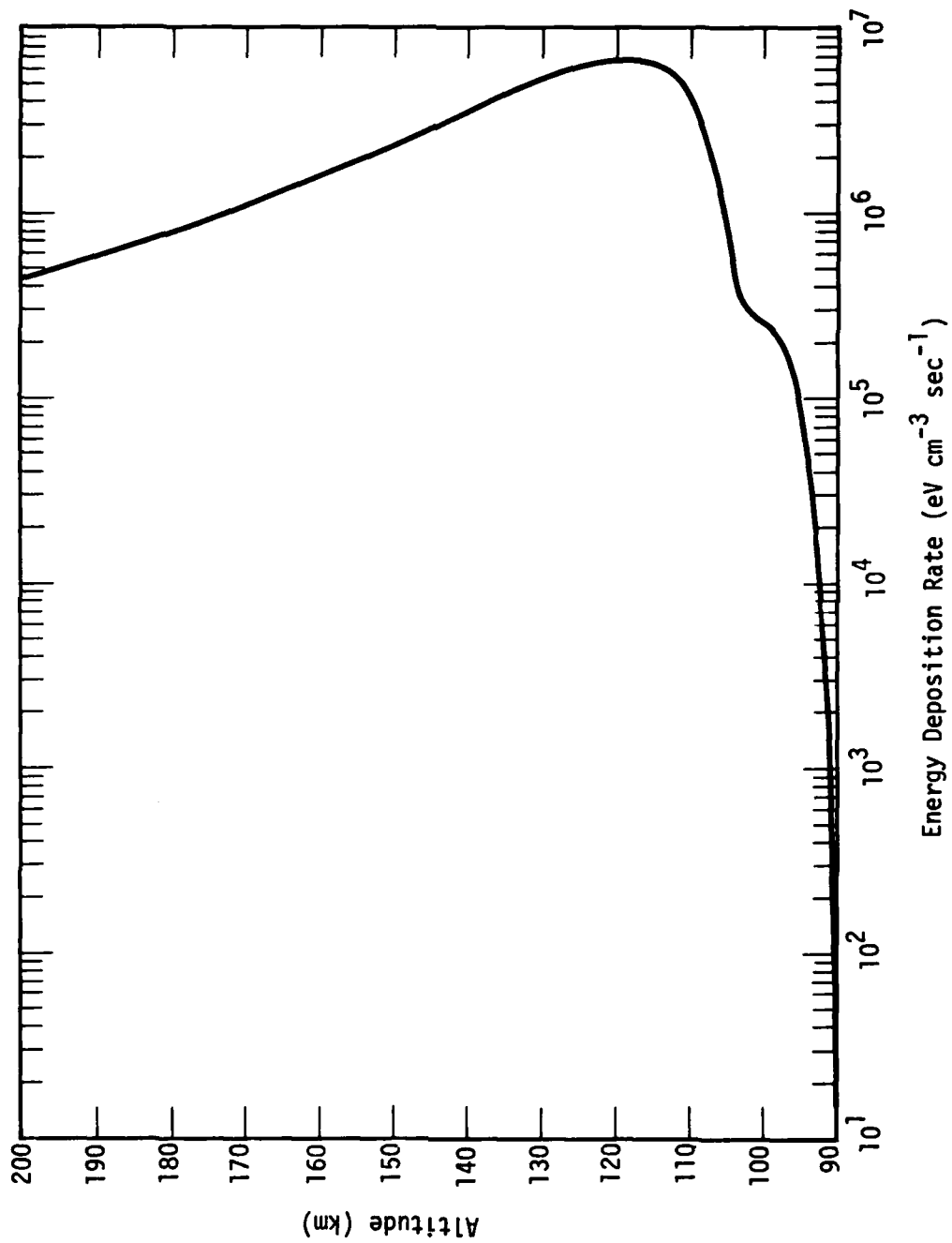


Figure 2-7. Calculated energy deposition rate in auroral arc (Sergeant Hydac IC 519.07-1B).

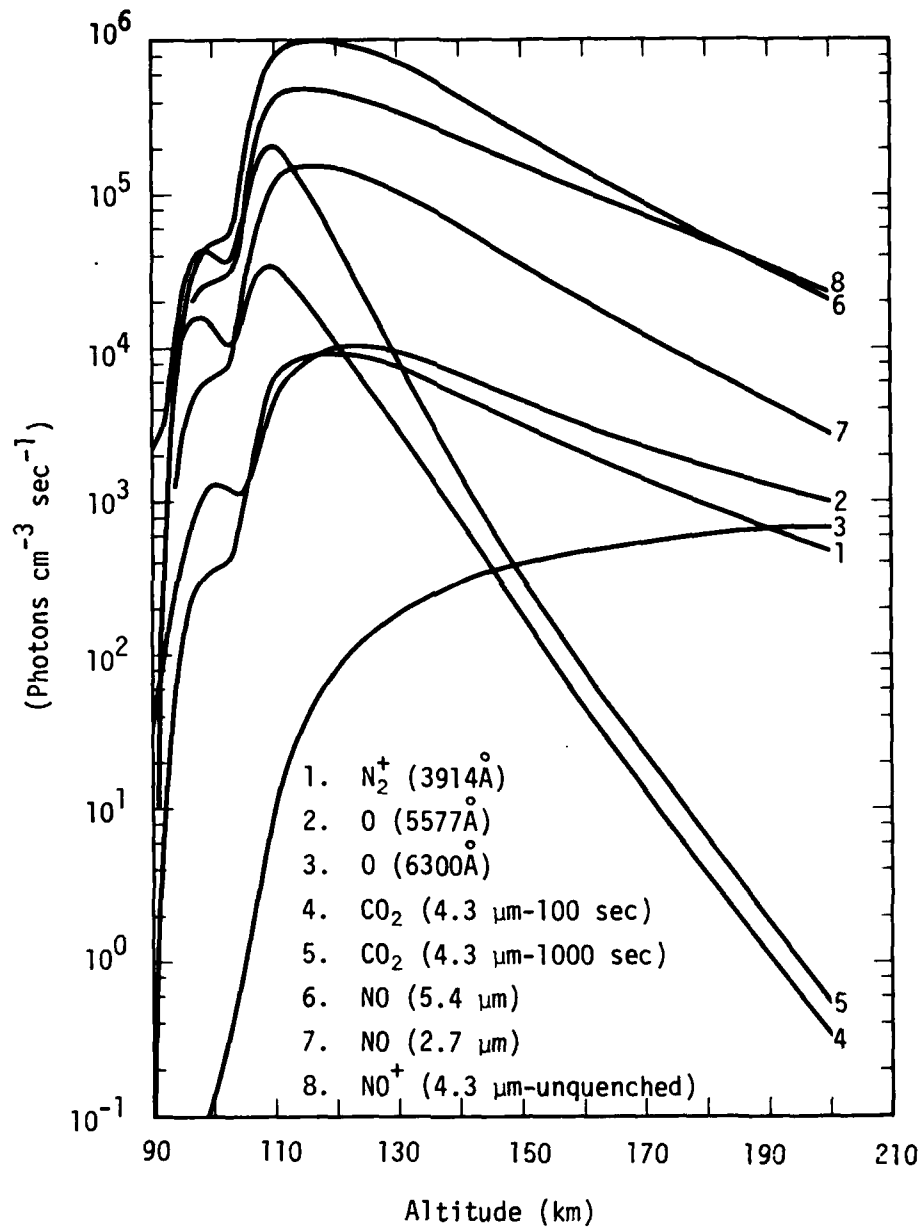


Figure 2-8. Calculated volume emission rates in auroral arc of 12 March 1975 (Sergeant Hydac IC 519.07-1B).

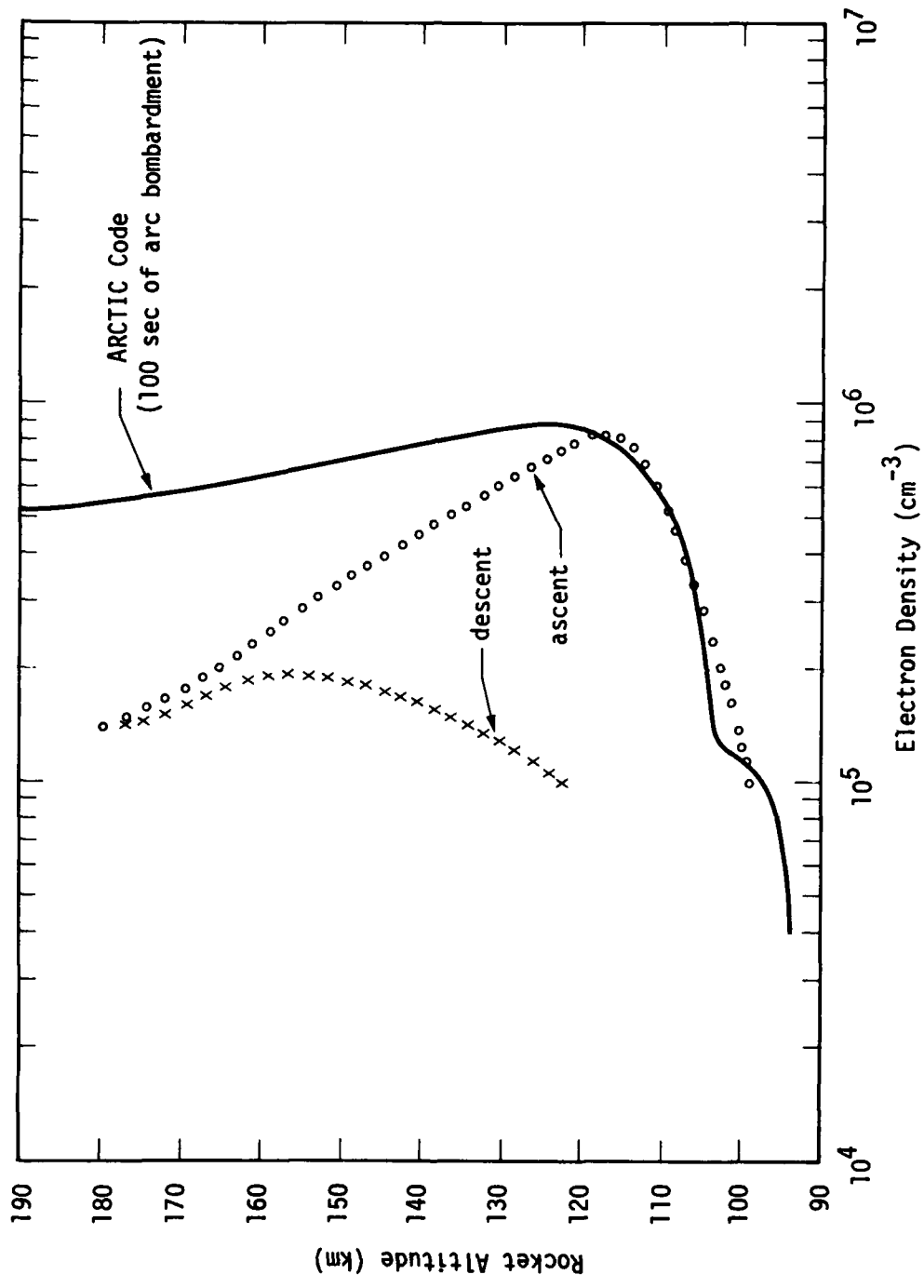


Figure 2-9. Electron density along rocket (IC 519.07-1B) trajectory, inferred from SRI radar data (Reference 6).

that altitude. The theoretical value at 180 km is 3 to 4 times larger than the radar data. If our input particle spectrum (Figure 2-6) is a reasonable representation of the precipitation into the arc system, then we are unable to account for the difference.\*

### 3914-Å EMISSION

In Figure 2-10 the zenith intensity at 3914Å measured by the rocket-borne photometer (Reference 10) is compared with the ARCTIC code calculations and with the intensity inferred from the SRI radar data. The latter was obtained by first computing a steady state volume emission rate and then integrating it over altitude. The volume emission rate,  $\dot{\phi}_{3914}$ , is proportional to the energy deposition rate which, in steady state, is proportional to  $n_e^2$ . Therefore,

$$\dot{\phi}_{3914} = \dot{\phi}_{3914 \text{ ARCTIC}} \frac{(n_e^2)_{\text{SRI}}}{(n_e^2)_{\text{ARCTIC}}}$$

where the subscripts "ARCTIC" and "SRI" refer to values obtained from the ARCTIC code and from the SRI radar, respectively. An altitude plot of  $(\dot{\phi}_{3914})_{\text{ARCTIC}}$  is shown in Figure 2-8.

In comparing the 3914-Å rocket data (ascent) with the code results, it should be borne in mind that the rocket did not enter the main arc until it was at about 125-km altitude (see Figure 2-3). When it was below this altitude, only part of the photometer sight path intersected the main arc

---

\* An overestimate of the input flux for electron energies between 0.1 and 0.7 keV cannot account for it. The input flux in this energy range is  $2.4 \times 10^{11}$  eV cm<sup>-2</sup> sec<sup>-1</sup>. The energy deposition rate required to produce, in steady state, the SRI and ARCTIC code profiles of  $n_e$  above 120-km altitude are, respectively,  $6.8 \times 10^{12}$  and  $2.0 \times 10^{13}$  eV cm<sup>-2</sup> sec<sup>-1</sup>. The difference is  $1.32 \times 10^{13}$  eV cm<sup>-2</sup> sec<sup>-1</sup> and this is 55 times larger than the assumed incident energy flux in the 0.1 to 0.7 keV range.

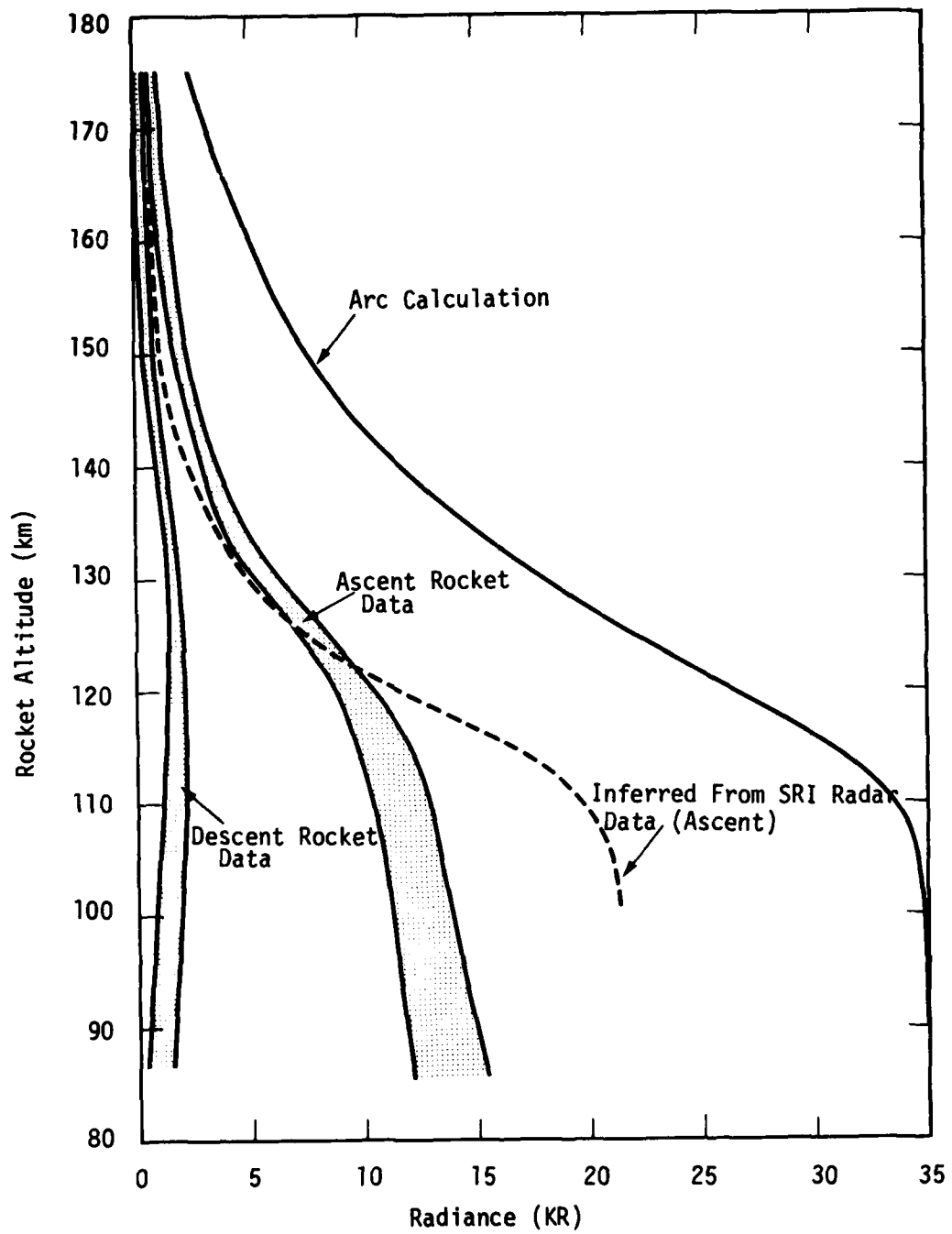


Figure 2-10. Zenith radiance at  $3914\text{\AA}$  (Sergeant Hydac IC519.07-1B); data and theory compared.

complex. The calculations, however, are based on a vertical sight path entirely within the arc. Therefore, until the rocket entered the arc, one might expect the measured intensity to be somewhat lower than the calculated values. The comparison shows, however, that the measured intensity is almost uniformly lower (factor 3 to 4) than that calculated over the height interval from 90 to 175 km. This discrepancy is consistent with earlier comparisons, especially those for the '73 and '74 Multi events reported in References 2 and 4. The reason for this persistent difference between the photometer data and our calculations, based on the particle data, is not known.

The 3914Å intensity profile inferred from the radar data, shown in Figure 2-10, is also larger than the rocket data below about 120 km. However, above about 125-km altitude it is smaller, thus tending to substantiate the notion that the energy deposition rate inferred from the radar data shown in Figure 2-9 may be too small in this altitude region.

#### 5.3- $\mu\text{m}$ EMISSION

Figure 2-11 shows a comparison between the rocket data (Reference 10) at 5.3  $\mu\text{m}$  and the code calculation of NO chemiluminescence. Both the radiometer and the CVF spectrometer data are shown. The latter was obtained by integration over the spectral features from 5.0 to 5.6  $\mu\text{m}$ . The integrated CVF data are seen to be larger than the radiometer data by a factor of about 2 on rocket descent and somewhat less than that on ascent. Part of this difference is probably attributable to the fact that the integrated CVF data covers a band of width 0.6  $\mu\text{m}$ , whereas the full width at half maximum of the radiometer response (Reference 11) is only about 0.3  $\mu\text{m}$ . The solid curve in Figure 2-11 is the calculated contribution to the emission from NO chemiluminescence. It is the total calculated band emission reduced by a factor of 0.23 (as explained in Reference 2, p. 65) to allow for the radiometer relative response function.

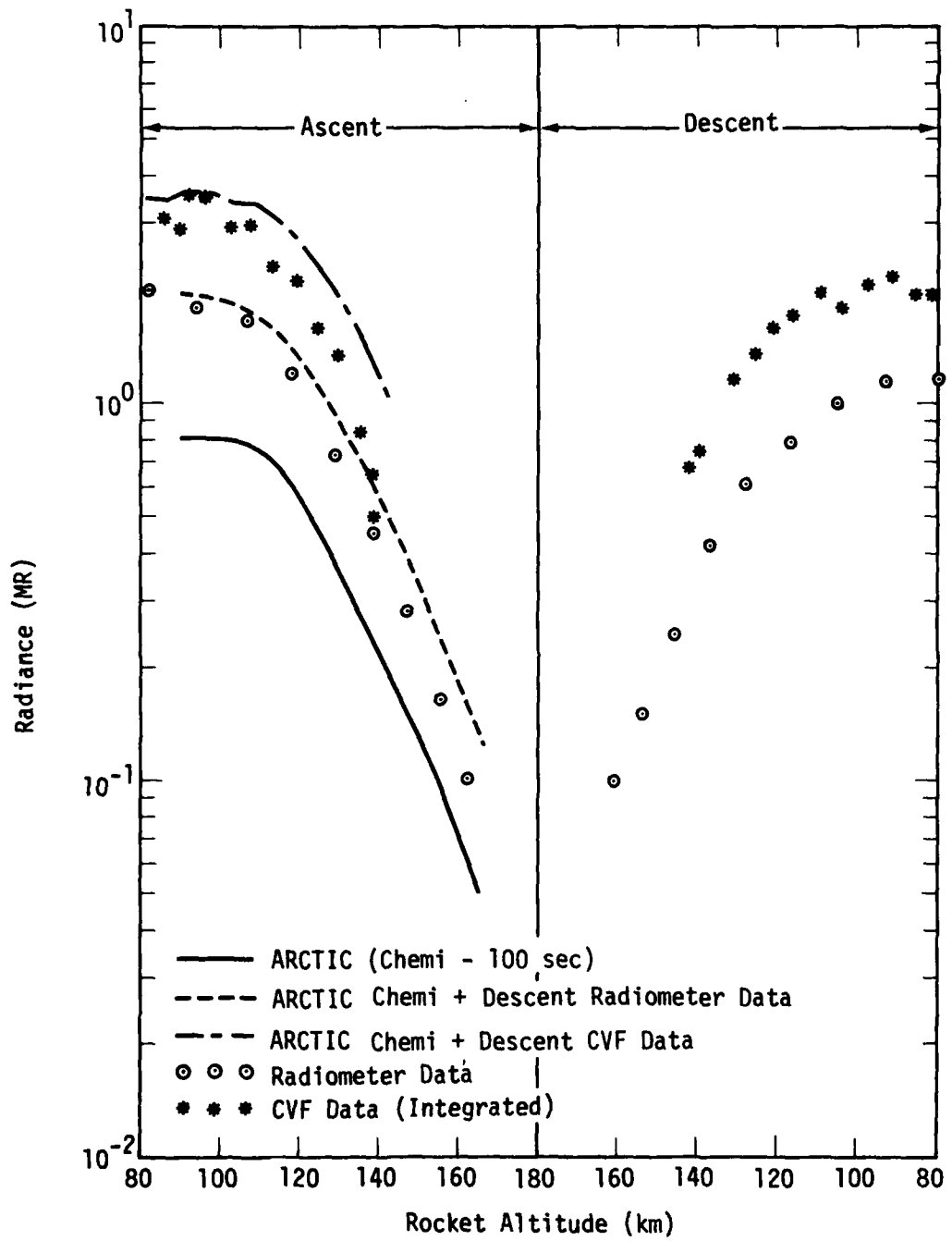


Figure 2-11. Calculated and observed zenith radiance in 5.3- $\mu$ m band (Sergeant Hydac IC 519.07-1B).

The calculated chemiluminescence (solid curve in Figure 2-11) is seen to be smaller than the ascent data. However, if we add to it the radiance measured by the radiometer on rocket descent, the resulting curve (dashed) is in reasonable agreement with the ascent radiometer data. Similarly, if we add to the chemiluminescence the radiance measured by the CVF spectrometer on descent, the resulting curve (dot dash) is in reasonable agreement with the ascent CVF data, especially below about 130 km.\* The rationale for doing this is the assumption that the descent data, taken in a region of low particle precipitation, is attributable to NO emission excited by the atom interchange reaction  $\text{NO}(v=0) + \text{O}^{\cdot} \rightarrow \text{NO}^{\cdot}(v=1) + \text{O}$  and by earthshine scatter from NO that operate equally on ascent through the arc and on descent outside the arc. Thus, we assume that the proper amount to add to the calculated chemiluminescence on ascent to allow for these additional excitation mechanisms is just the measured descent radiance. The NO profile required to match the descent radiometer data is shown in Figure 5-1.

It should be emphasized that the chemiluminescent contribution to the NO emission is based on certain assumptions that have not yet been verified experimentally. The principal assumption is that, following chemical formation of NO, the vibrational states are populated with equal probability up to the maximum allowed by energy conservation.† This leads to the emission spectrum shown in Figure 2-9 of Reference 4. A different assumption would have led to a different spectrum and to a different fraction of the energy emitted in the radiometer pass band and in the 5.0 to 5.6- $\mu\text{m}$  wavelength interval.

---

\* For comparison with the CVF data, we have taken the chemiluminescent contribution equal to 0.44 of the total calculated band emission. This is because 44 percent of the energy in the calculated chemiluminescent spectrum (Figure 2-9 of Reference 4) is contained in the wavelength band from 5.0 to 5.6  $\mu\text{m}$ .

† In our model, most of the NO chemiluminescence arises from the reaction  $\text{N}(^2\text{D}) + \text{O}_2 \rightarrow \text{NO}^{\cdot} + \text{O}$ .

The CVF spectra provide some basis for understanding the emission mechanisms and radiating species involved, although their usefulness in this regard is limited by the instrument resolution and the long wavelength cut-off at about 5.64  $\mu\text{m}$ . Assuming that the (1,0) band of NO is a principal contributor, we have calculated what the corresponding CVF spectrum should look like for a rotational temperature of 250  $^{\circ}\text{K}$ . The results are shown in Figure 2-12. Three different spectra are shown, each representing a different instrument resolution. For the instrument used on rocket IC 519.07-1B, the resolution near 5.3  $\mu\text{m}$  is about 0.13  $\mu\text{m}$  (Reference 12). However, our theoretical curves are based on a flat response over the resolution element whereas, in practice, it is more nearly triangular, or at least gaussian. Therefore, with respect to our calculated spectra, the lower one in Figure 2-12, corresponding to 0.12- $\mu\text{m}$  resolution, is probably the most applicable.

Figure 2-13 compares this theoretical spectrum with a typical CVF feature. The two spectra have been normalized so that the magnitude of their peaks coincide. Although the observed feature is broader than the theoretical one, the positions of the CVF peaks are in striking agreement with the R- and P-branch peaks of the (1,0) band of NO.

One might be tempted to attribute the broader CVF features to contributions from higher vibrational transitions of the  $\Delta v=1$  sequence. However, although this could account for broadening on the long wavelength side of the feature, it could not account for broadening on the short wavelength side unless the rotational temperature is effectively much higher than what we have assumed. In fact, it is likely that the emission at 5.0  $\mu\text{m}$ , which appears persistently in CVF data from all ICECAP rockets, arises from some source other than NO.\*

---

\* The suggestion has been made that  $\text{CO}_2$  may be a principal contributor near 5.0  $\mu\text{m}$ . However, the altitude dependence of the emission does not support this hypothesis.

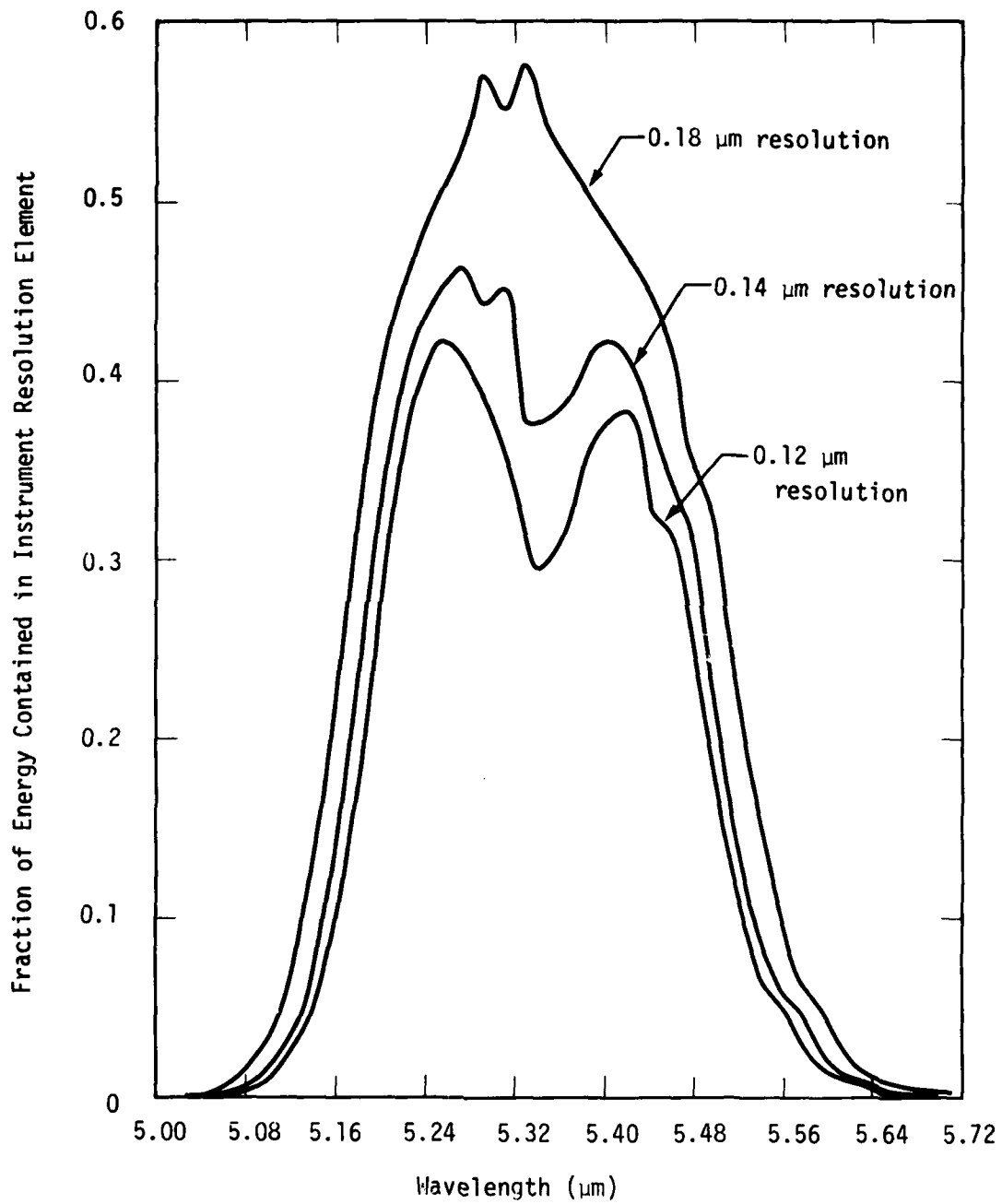


Figure 2-12. Calculated CVF spectrometer spectrum for the (1,0) band of NO at 250 °K.

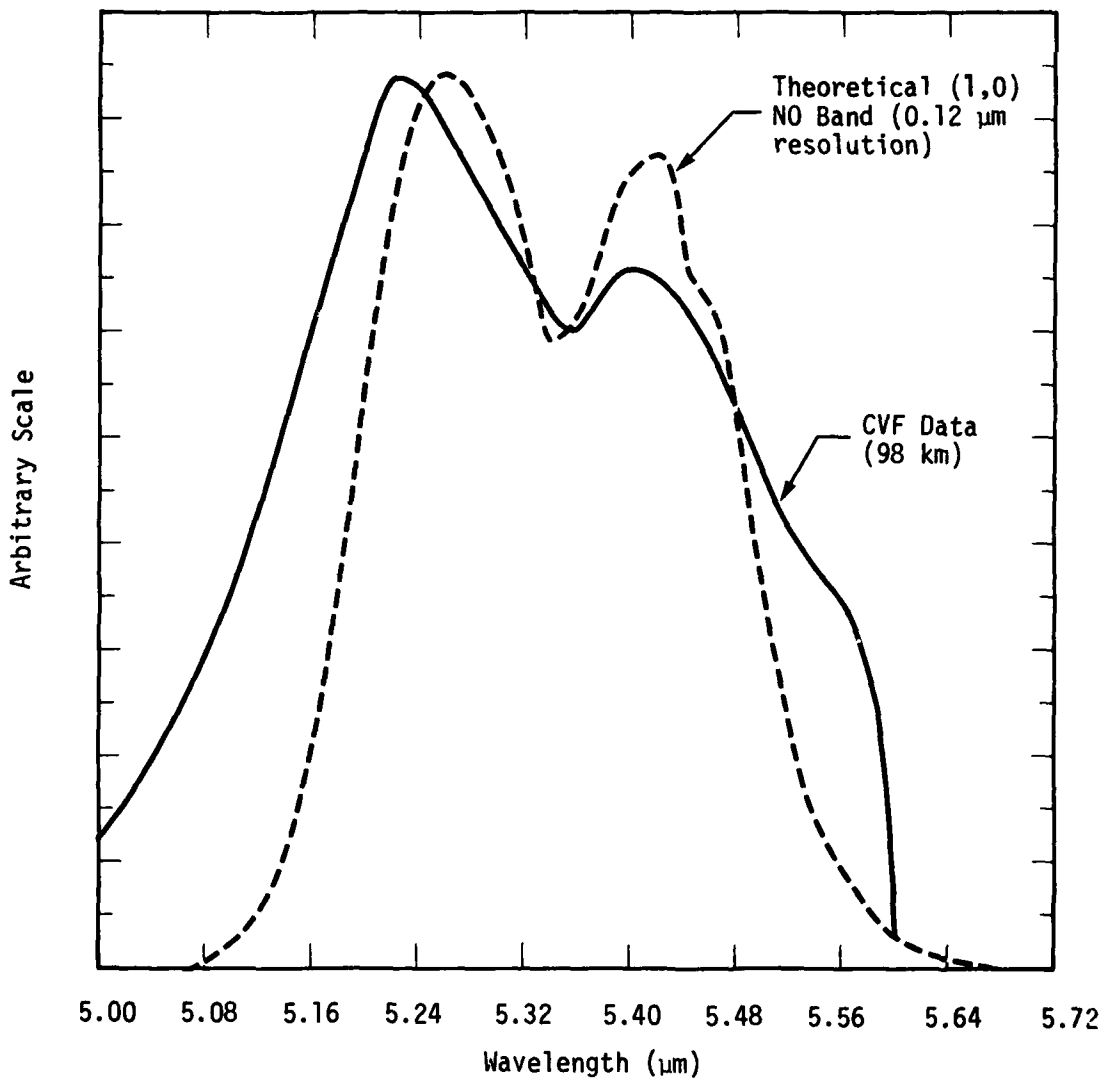


Figure 2-13. Typical CVF spectrometer feature near 5.3  $\mu\text{m}$  (from rocket IC 519.07-1B) compared with the theoretical (1,0) band spectrum of NO at 250  $^{\circ}\text{K}$ .

The observed CVF features are not consistent with the calculated NO chemiluminescent spectrum (based on  $v = 0$  to 18 equally populated) shown in Reference 4 (Figure 2-9b). This spectrum exhibits considerable emission at wavelengths longer than the spectrometer cut-off at  $5.64 \mu\text{m}$ . But the observed features usually drop below noise, even at  $5.60 \mu\text{m}$ , indicating little or no signal at  $5.64 \mu\text{m}$ .

By contrast, as we have seen above, the data are much more consistent with the assumption that only the (1,0) band of NO is principally involved. This supports the atom interchange + earthshine scatter hypothesis for which only  $\text{NO}(v = 1)$  would be appreciably excited.

#### 4.3- $\mu\text{m}$ EMISSION

Figure 2-14 shows the measured zenith radiance near  $4.3 \mu\text{m}$ . It includes the radiometer data and also the CVF spectrometer data integrated in wavelength over the  $4.3\text{-}\mu\text{m}$  features. Again, the wavelength intervals covered in Figure 2-14 by the two instruments are not identical. The half power points on the radiometer response (Reference 11) lie between  $4.21$  and  $4.31 \mu\text{m}$ , whereas the CVF features were integrated from  $4.08$  to  $4.32 \mu\text{m}$ .

Also shown in Figure 2-14 are several theoretical results. The dashed curves give the calculated zenith radiance from  $\text{CO}_2$  vibrational luminescence after 100 and 1000 sec of arc bombardment. The dotted curve is Kumer's estimate (Reference 13) of the ambient nighttime  $\text{CO}_2$  radiance from thermal collisions and earthshine scatter. The dot-dash curve is an estimate of the  $\text{CO}_2$  vibrational luminescence due to drizzle bombardment of the ascent rocket air-space during the half hour prior to rocket launch. It is based on an ARCTIC code calculation of the drizzle environment assumed for the '74 Multi event (Reference 4) and results from an energy input flux of about  $4 \text{ ergs cm}^{-2} \text{ sec}^{-1}$ . This is reasonably consistent with the measured flux shown in

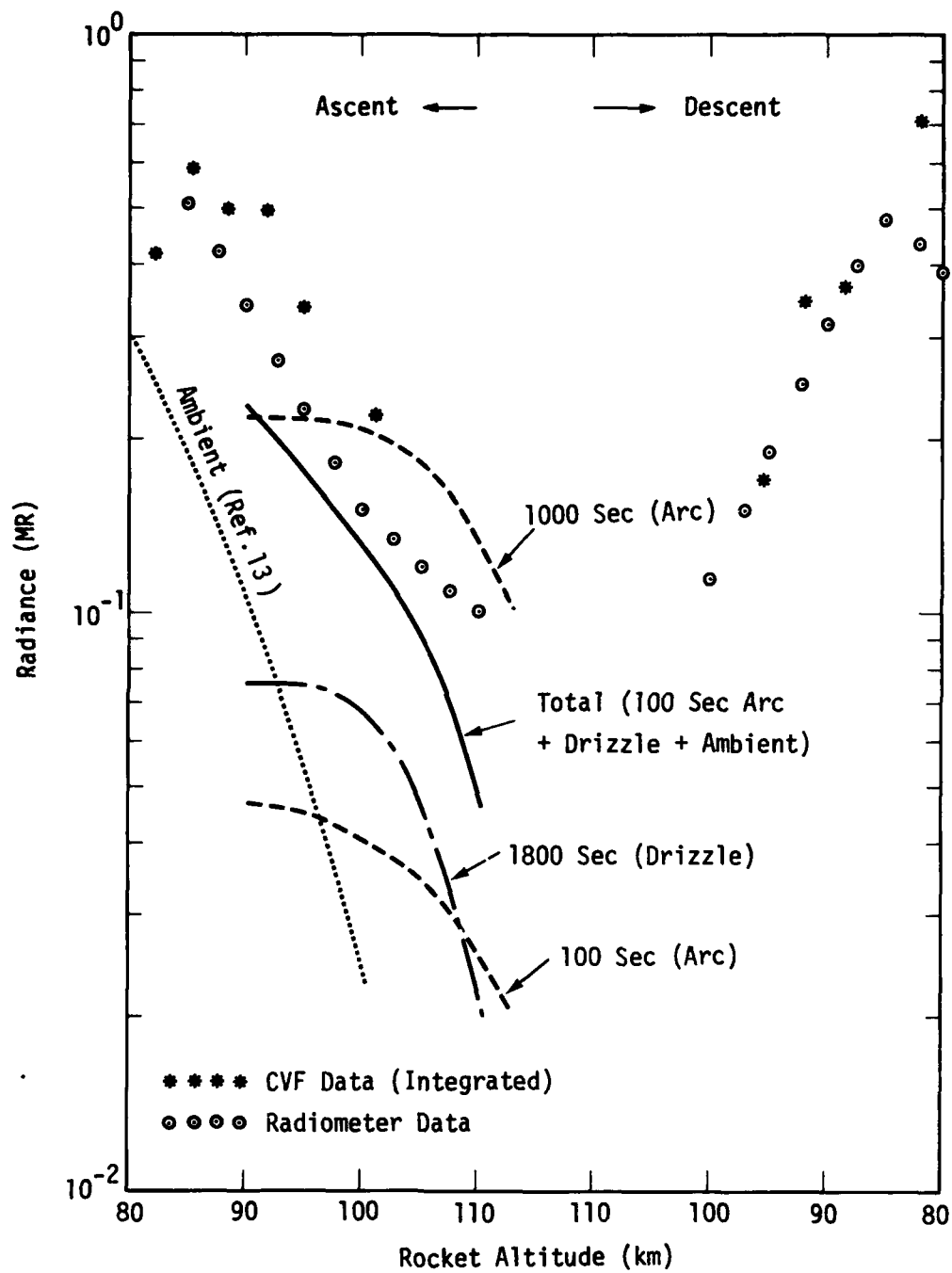


Figure 2-14. Observed zenith radiance near  $4.3 \mu\text{m}$  compared with calculated  $\text{CO}_2$  emission (Sergeant Hydac IC 519.07-1B).

Figure 2-4, although it may be a little on the low side. The solid curve is the sum of the contributions from the arc (100 sec), the drizzle, and the ambient  $\text{CO}_2$  radiance. The ARCTIC code results (dashed and dot-dash curves) have been corrected for the radiometer relative response function so as to make them comparable with the radiometer data.

The solid curve is seen to be in good agreement with the radiometer data between about 90 and 105 km. However, at higher altitudes the calculated vibrational luminescence falls off faster than does the ascent radiometer data so that by 110 km they differ by a factor of 2.

It should be realized that detailed agreement between auroral data at  $4.3 \mu\text{m}$  and a calculation of  $\text{CO}_2$  vibrational luminescence, such as we have done, is not generally to be expected. The reason for this is that energy deposited in vibrational excitation of  $\text{N}_2$  at any given time is (partially) transferred to  $\text{CO}_2$  and radiated at  $4.3 \mu\text{m}$  with an e-folding time ranging from about 8 minutes at 100 km to over one half hour at 120 km. Therefore, the  $\text{CO}_2$  emission at any given time is the integrated contribution, due to vibrational excitation of  $\text{N}_2$ , over past times. An accurate calculation would require a knowledge of the spectral flux of precipitating electrons for minutes to hours (depending on altitude) prior to the measurement time. In addition, as pointed out by Kumer (Reference 13), transport effects due to winds and diffusion can appreciably modify the local concentration of  $\text{N}_2(v=1)$ , and hence the  $\text{CO}_2$  emission, in the time scales involved. These effects should also be included. Detailed information of this nature has yet to be available in any auroral experiment.

In the calculations presented in Figure 2-14, we used the measured arc flux and guessed that it bombarded the rocket airspace for 100 sec. This seems reasonable on the basis of the arc morphology inferred from the Lockheed photometer data, but the magnitude of the emission is sensitive to the actual bombardment time which could have been at least a factor of 2,

more or less, than what we assumed. The predosing from the drizzle is also a guess, albeit aided by the ground photometer data. Furthermore, no correction for transport effects has been made. Considering all these uncertainties and assumptions, the agreement with the data should be considered good. We feel that the  $\text{CO}_2$  vibrational luminescence can, in the main, account for the ascent data at  $4.3 \mu\text{m}$ . It is likely, however, that on ascent through the arc complex, the instruments received additional contributions at  $4.3 \mu\text{m}$  from  $\text{NO}^+$  chemiluminescence. This possibility is discussed below.

In Figure 2-14 the descent data near  $4.3 \mu\text{m}$  are also shown. It should be noted that although the rocket descended in a region of low particle precipitation, the radiance measured near  $4.3 \mu\text{m}$  is almost as large as that on rocket ascent through the arc. This is further evidence in support of  $\text{CO}_2$  vibrational luminescence as the main mechanism operating near  $4.3 \mu\text{m}$ . For if the radiance were mainly from  $\text{NO}^+$  chemiluminescence, then the data on descent through the drizzle should have been considerably less than that on ascent through the arc because the time constant for decay of  $\text{NO}^+$  chemiluminescence is short (a few seconds). On the other hand, the rocket descent airspace had been bombarded by the arc flux about 12 minutes earlier as the arc system moved south through it. The decay of the  $\text{CO}_2$  vibrational luminescence is sufficiently slow so that the emission seen on descent could result from this earlier bombardment.

Figure 2-15 shows the calculated zenith intensity at  $4.3 \mu\text{m}$  from  $\text{NO}^+$  chemiluminescence in the arc. The upper dashed curve is an integral over altitude of the volume emission rate shown in Figure 2-8. It is for the entire band, uncorrected for instrument response, and it does not include collisional quenching. Clearly, this uncorrected intensity is much larger than that observed by the radiometer. The middle dashed curve in Figure 2-15 incorporates a correction factor of 0.16 to allow for the radiometer relative response function (see Reference 2, p. 72). This correction factor is based

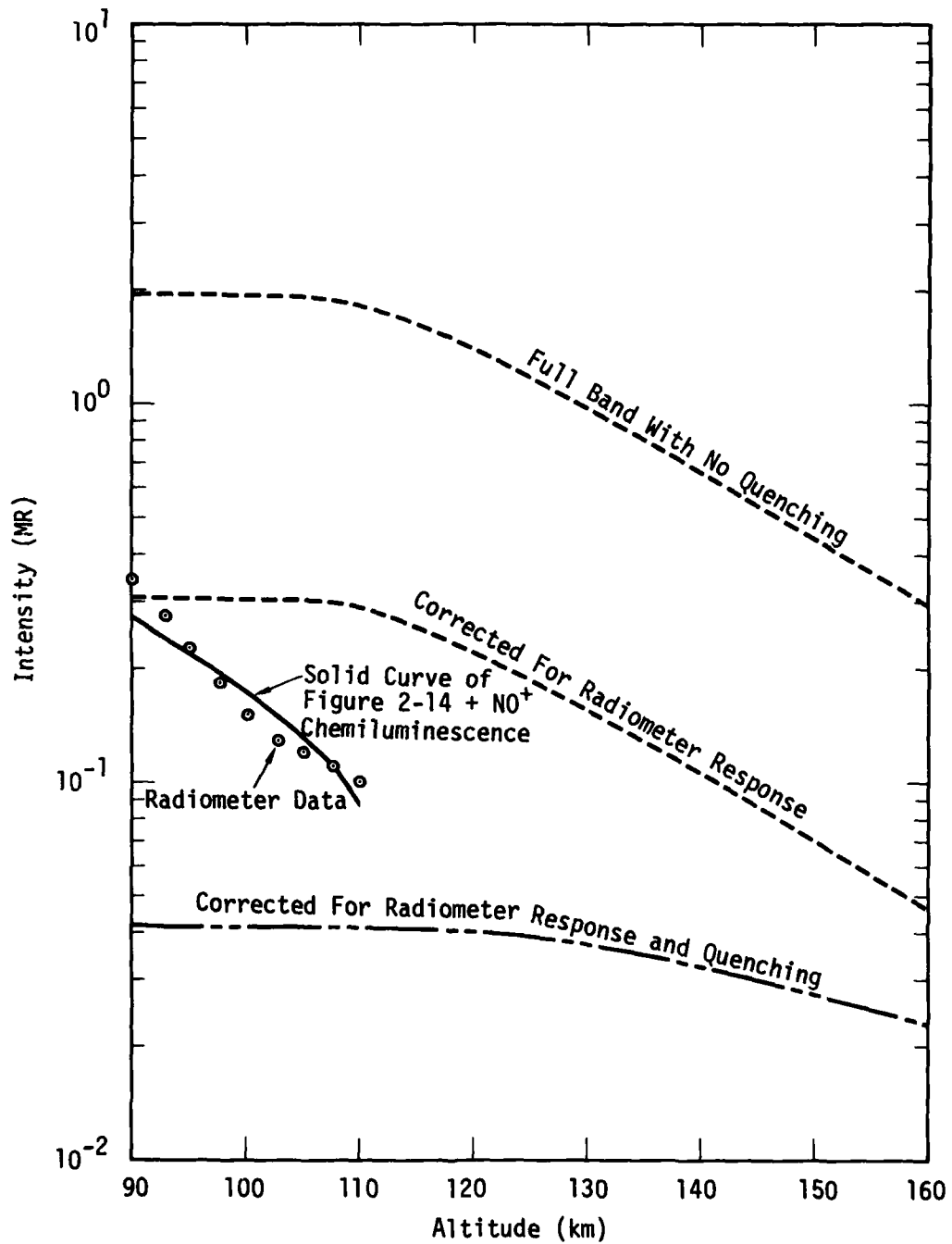


Figure 2-15. Possible contribution of  $\text{NO}^+$  chemiluminescence to observed emission in radiometer band near  $4.3 \mu\text{m}$ .

on the assumption that the chemiluminescent spectrum shown in Figure 2-16 (Reference 4) is applicable. No laboratory data exist to support it.

The lowest curve in Figure 2-15 (dot-dash) incorporates an additional correction for collisional quenching. To our knowledge, quenching rates for the vibrational states of  $\text{NO}^+$  have not been measured. However, if we assume that vibrational quenching of  $\text{NO}^+$  proceeds mainly by v-v transfer to  $\text{N}_2$  with rate constant  $k$ , then we can allow, approximately, for it by reducing the volume emission rate by the factor  $A_{10}/(A_{10}+k[\text{N}_2])$  where  $A_{10}$  is the Einstein transition rate for the fundamental band of  $\text{NO}^+$ . The dot-dash curve is based on values for  $A_{10}$  and  $k$  of  $13.4 \text{ sec}^{-1}$  and  $1 \times 10^{-9} \text{ cm}^3 \text{ sec}^{-1}$ , respectively. When the dot-dash curve is added to the  $\text{CO}_2$  emission (solid curve in Figure 2-14), the solid curve in Figure 2-15 results. The radiometer data are shown for comparison.

Unfortunately, as explained above, there are too many uncertainties inherent in the  $\text{CO}_2$  calculation, as well as in the photon efficiency spectrum of  $\text{NO}^+$  chemiluminescence, to say if the apparent agreement with the  $4.3\text{-}\mu\text{m}$  data shown in Figure 2-15 has any significance. The only thing we can say for sure is that if the assumptions inherent in our  $\text{CO}_2$  and  $\text{NO}^+$  calculations are reasonably good, then a (lumped) quenching rate constant for the vibrational states of  $\text{NO}^+$  as large as  $1 \times 10^{-9} \text{ cm}^3 \text{ sec}^{-1}$  is needed. A value of this magnitude is not unusual for an ion-molecule reaction.

#### 2.7- $\mu\text{m}$ EMISSION

No data at  $2.7 \mu\text{m}$  are available from rocket IC 519.07-1B with which to compare our calculated NO chemiluminescence. The CVF spectrometer data in this spectral region appear to be primarily noise. This is consistent with our calculated intensity at  $2.7 \mu\text{m}$  that is below the instrument noise level of  $2.3 \text{ MR}(\mu\text{m})^{-1}$ . To this extent, therefore, our calculated NO chemiluminescence is not in disagreement with the CVF spectrometer observations.

## SUMMARY AND CONCLUSIONS

Results and conclusions from our study of the 12 March 1975 auroral event can be summarized as follows:

(1) The calculated 3914-Å intensity profile for the arc system, based on the measured particle flux, is a factor of 3 to 4 times larger than that measured by the rocket-borne photometer. This result is consistent with corresponding comparisons made for other auroral events, although the reason for it is not known.

(2) The emission intensity observed near 5.3  $\mu\text{m}$  on rocket descent through a low level drizzle precipitation region can be accounted for on the basis of atom interchange + earthshine scatter excitation of NO for a suitably chosen enhanced NO profile. A combination of this descent emission and the calculated NO chemiluminescence in the arc is in good agreement with the data measured on rocket ascent through the arc complex. The peaks in the CVF spectra near 5.3  $\mu\text{m}$  correspond closely to the R and P branches of the (1,0) fundamental band of NO. Thus, the data are generally consistent with NO emission, excited by a combination of atom interchange and earthshine scatter, as the principal source of radiation near 5.3  $\mu\text{m}$ .

(3) The ascent and descent rocket data near 4.3  $\mu\text{m}$  are consistent with CO<sub>2</sub> vibrational luminescence as the dominant emission mechanism. However, detailed agreement with theory cannot be expected unless accurate account is taken of predosing and the transport of vibrationally excited N<sub>2</sub> by winds and diffusion.

(4) In order to suppress NO<sup>+</sup> chemiluminescence, that would otherwise dominate the emission near 4.3  $\mu\text{m}$ , a quenching rate coefficient (by N<sub>2</sub>) as large as  $1 \times 10^{-9} \text{ cm}^3 \text{ sec}^{-1}$  is needed.

(5) The CVF spectrometer data near 2.7  $\mu\text{m}$ , consisting of noise, is not inconsistent with our calculated emission from NO chemiluminescence that also provides for signal levels below the instrument noise.

SECTION 3  
AURORAL EVENT OF 10 MARCH 1975  
(Nike Hydac IC 507.11-2A)

PRELIMINARY

On 10 March 1975, at 0912:20 UT (2312:20 local time), rocket IC 507.11-2A was launched from Poker Flat into a very active auroral breakup, reaching an apogee of 152.3 km at 200 sec after launch. The region traversed by the rocket was the central intense part of a westward traveling surge (Reference 5). The scanning photometer data of Sears (Reference 9) showed that the region was very broad, extending 30 degrees on either side of the zenith at Chatanika.

The rocket-borne instrumentation included three vertical-viewing, helium-cooled radiometers operating in the 5.6-, 9.6-, and 7-12-  $\mu\text{m}$  regions. No particle detectors or other optical instrumentation were on board.

In addition to the Lockheed scanning photometer data (Reference 9), other ground support data for this event are available from the SRI incoherent backscatter radar (Reference 6). Camera malfunction precluded any scanning photometer data from Ft. Yukon or Ester Dome.

Since no measured particle flux data are available for this event, and only very limited optical/IR data, no attempt was made to make a detailed ARCTIC code calculation. Rather, we have attempted to scale from previous calculations to infer what the zenith intensity due to NO chemiluminescence should have been, and to compare the results with the radiometer data.

## ENERGY DEPOSITION

The total energy deposition rate from precipitating electrons has been inferred from the Lockheed photometer data (Reference 9) and the SRI radar data (Reference 6). Both sets of data show the deposition rate peaking at about 0915 UT, just after rocket launch. However, the photometer data shows a peak of over  $200 \text{ ergs cm}^{-2} \text{ sec}^{-1}$ , while the radar data indicate about  $62 \text{ ergs cm}^{-2} \text{ sec}^{-1}$ , over a factor of 3 less.

Since the radar data provide an altitude profile of the electron density,  $n_e$ , we have used it to infer an energy deposition rate profile,  $\dot{\epsilon}$ . In particular, in steady state,

$$\dot{\epsilon} = \eta \alpha n_e^2 \quad (3-1)$$

where  $\eta$  is eV/ion pair, and  $\alpha$  is the effective electron recombination coefficient. Figure 3-1 shows the electron density profile (Reference 6) measured for the time period 0914:22-0920:58. Since it is fairly similar to the one calculated for the '73 Multi arc, we have used our results from that calculation to provide profiles for  $\eta$  and  $\alpha$ , the latter of which is shown in Figure 3-1. The value of  $\eta$  varies slowly from about 35.1 at 90 km to 33.4 at 175 km. The resulting profile of  $\dot{\epsilon}$  is also shown in Figure 3-1.

## COMPARISONS WITH DATA IN 5.3- $\mu\text{m}$ BAND

To compute the NO chemiluminescence from the deposition rate profile shown in Figure 3-1, we have adopted the 5.3- $\mu\text{m}$  photon efficiency (photons per eV deposited) calculated for the '73 Multi event (rocket A18.205-1) for a bombardment time of 80 sec. This is shown in Figure 3-2, along with the resulting volume emission rate profile.

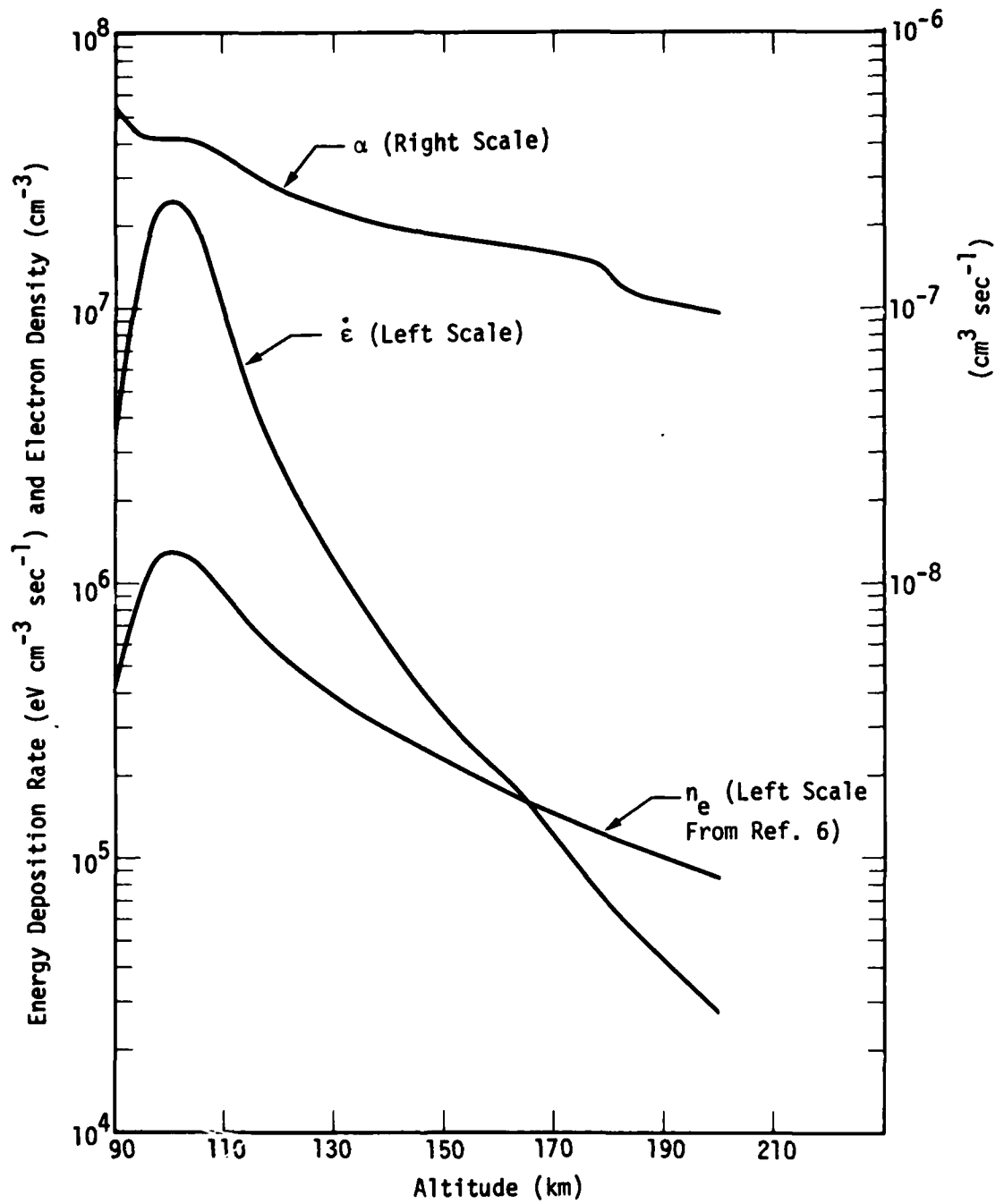


Figure 3-1. Measured electron density and inferred energy deposition rate profiles for auroral event of 10 March 1975.

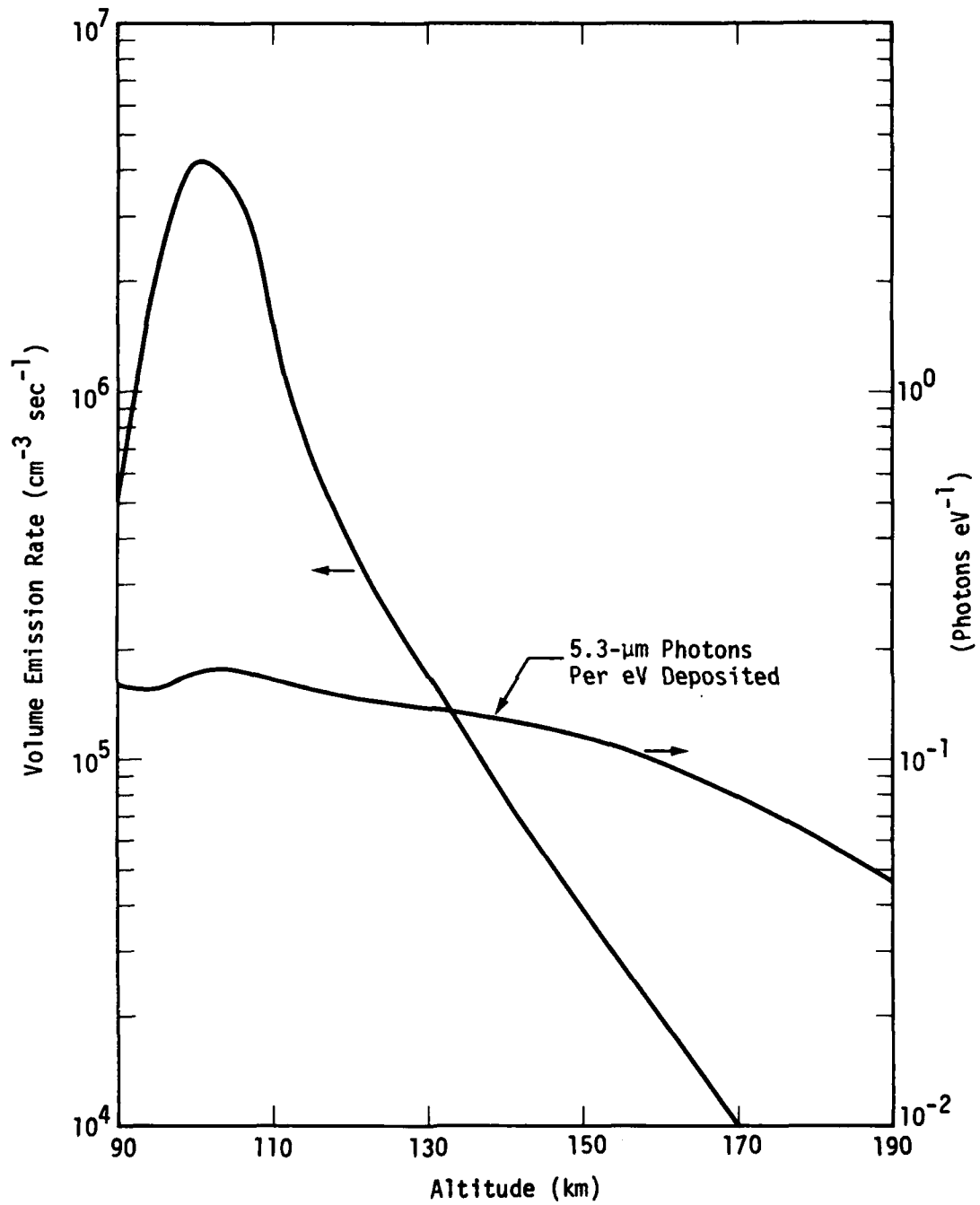


Figure 3-2. Calculated volume emission rate near 5.3  $\mu\text{m}$  from NO chemiluminescence for auroral event of 10 March 1975.

Figure 3-3 shows a comparison between the intensity measured by the radiometer on rocket ascent and our computed intensity from NO chemiluminescence. (The descent data are similar, at least above 110 km). The effective radiometer passband covers the wavelength interval from 5.27 to 5.88  $\mu\text{m}$  (Reference 14). The theoretical curve in Figure 3-3 is the altitude-integrated volume emission rate (Figure 3-2) with a correction factor of 0.65 applied to allow for the fraction of the chemiluminescent spectrum (Reference 2, Figure A-1) that falls in the radiometer passband.

The agreement between the two curves in Figure 3-3 is obviously poor, especially above 100 km where the theoretical curve falls off with increasing altitude much faster than does the data. One might argue that this may be due to an underestimate of the energy deposition at higher altitudes, based on the radar data, as appeared to be the case for the 12 March 1975 event (see Section 2, especially Figure 2-9). However, our revised ARCTIC code calculation for the '73 Multi event gives, for 80 sec of arc bombardment, an NO emission profile similar in shape to that shown in Figure 3-3 and only a factor of 2 larger. It is unlikely, therefore, that had a measured particle spectrum been available to us, and a full code calculation been performed, results much different from those shown in Figure 3-3 would have been obtained. In fact, all previous runs with the ARCTIC code have shown that, although the magnitude of the chemiluminescent intensity changes as the input spectral flux is changed, the shape of the altitude profile remains approximately the same as shown in Figure 3-3. It does not seem possible to match the shape of the radiometer curves in Figure 3-3 with NO chemiluminescence alone.

It is tempting, as in previous comparisons with data near 5.3  $\mu\text{m}$ , to attribute the difference to excitation of NO by a combination of the atom interchange reaction,  $\text{NO}(v=0) + \text{O}^{\bullet} \rightarrow \text{NO}^{\bullet}(v=1) + \text{O}$ , and earthshine scatter, operating on an aurorally enhanced NO profile. However, if this is indeed the explanation, then NO concentrations 4 to 5 times larger than the

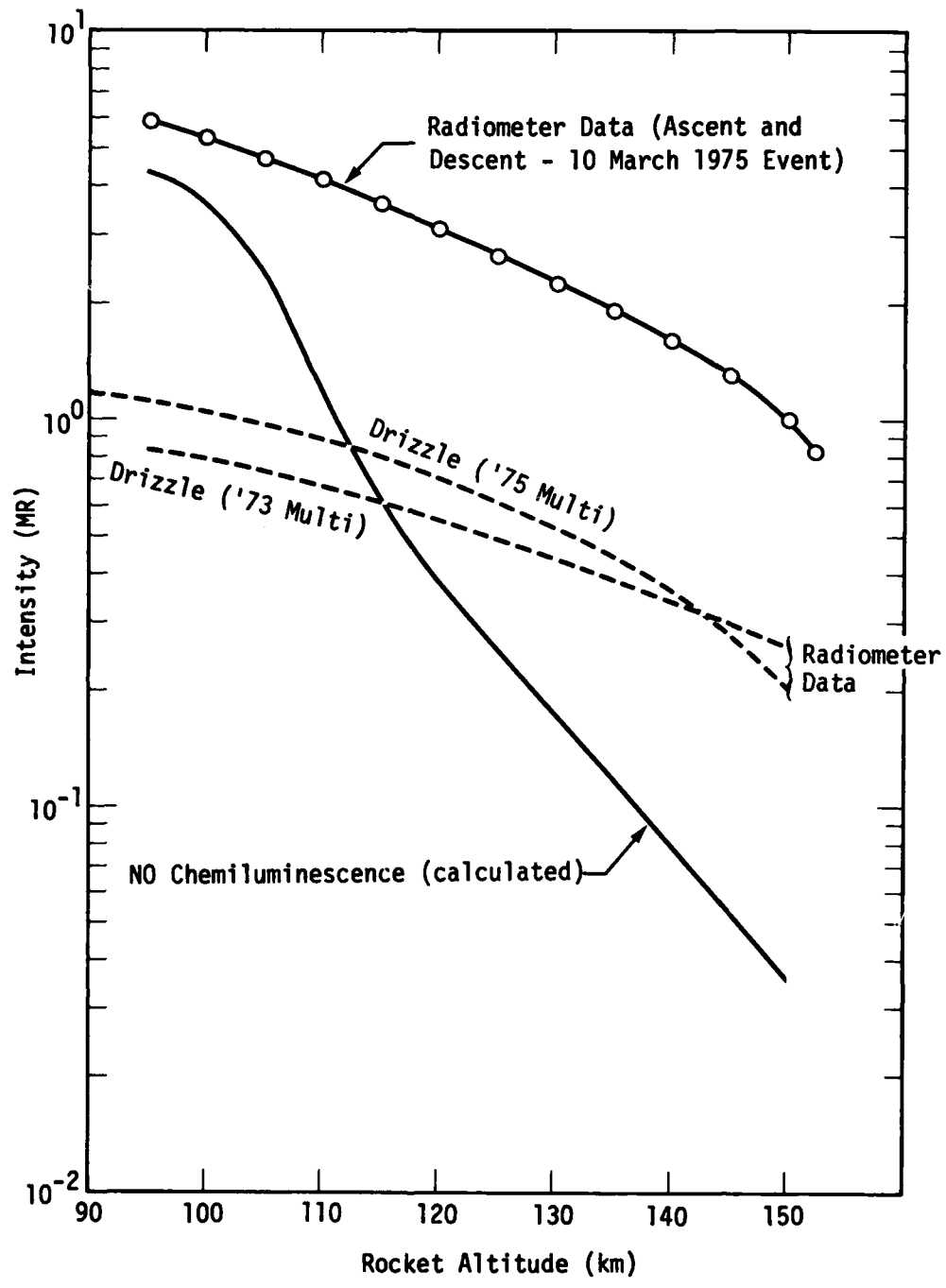


Figure 3-3. Measured 5.3- $\mu$ m band emission compared with calculated NO chemiluminescence for 10 March 1975 auroral event (IC 507.11-2A).

already enhanced values that seem to have been present under certain other auroral conditions would be required. This follows from a comparison with the radiometer data obtained on descent of the '73 and '75 Multi rockets through drizzle regions (shown by the dashed curves in Figure 3-3). These data have previously been ascribed to NO emission excited by earthshine scatter and atom interchange, and are seen to be 4 to 5 times smaller than the present radiometer data.\* In fact, if we ascribe all of the present radiometer data to these mechanisms, the inferred NO profile is shown in Figure 5-1 of Section 5. It is, indeed, seen to be considerably enhanced over the other enhanced profiles.

Although intense precipitation occurred during the rocket flight, its duration in the rocket airspace prior to launch was too short for any appreciable buildup of the NO. Probably of more significance, however, is the predosing received over longer time periods prior to rocket launch. We have estimated the relative predosing for the present event (of 10 March 1975) and for the '75 Multi event (2 days later) using the time histories of energy deposit by particle precipitation given by Sears (Reference 9) and Vondrak (Reference 6). From the optical data (Reference 9), the ratio of the integrated energy deposition over a time span of 67 min prior to rocket launch on 10 March 1975, to that on 12 March 1975, is about 3.2. From the radar data (Reference 6), the corresponding ratio, over a time span of 138 min, is 4.3.

These numbers suggest that the integrated dosage prior to the 10 March event may have been sufficiently greater than that prior to the 12 March event to produce the additional NO concentration required. Longer integration times are needed, however, to say with more assurance whether or not this is likely to be the case.

---

\* Although the radiometer used for the 10 March 1975 event was not identical to those used in the other two experiments, we feel that the difference is not enough to be very significant.

## SUMMARY AND COMMENTS

Based on the electron density profile measured by the SRI backscatter radar, we have inferred an energy deposition rate profile for the auroral event of 10 March 1975 and, together with results from previous ARCTIC code calculations, have estimated the intensity profile of NO chemiluminescence near 5.3  $\mu\text{m}$ . The results show that chemiluminescence cannot account for the radiometer data, especially at altitudes above 100 km.

It is possible to account for the results on the basis of NO emission excited by earthshine scatter and the atom interchange reaction, but only by invoking an NO profile that is considerably enhanced over already enhanced profiles inferred from other auroral events. A limited survey of data on predosing suggests that the integrated energy deposited in the region prior to rocket launch may, at least qualitatively, account for the presence of larger NO values. However, for this very intense event, one would have expected NO chemiluminescence near 5.3  $\mu\text{m}$  to dominate other mechanisms. It is rather disconcerting that this does not appear to have been the case.

## SECTION 4 CODE CALCULATION OF THE ELECTRON TEMPERATURE

### PRELIMINARY

In comparing ARCTIC code calculations of electron temperature, performed prior to the present effort, with observational data for the auroral environment, it became clear that the code results were too large. In fact, at low altitudes (~100 km) in strong arcs (such as the '74 Multi event) our temperature values were high by as much as a factor of 5. Such errors can impact severely upon the accuracy of calculated species concentrations, especially those of the ions and electrons. Considerable effort was devoted to tracking down the source of the error and in providing a computational method that we now believe is accurate. It incorporates several features that have not hitherto been reported in the literature. This section, along with Appendices A and B, is devoted to a description of this work.

### HEATING AND COOLING RATES

The basic equation used in the ARCTIC code for determining the electron temperature is given by (Reference 1)

$$\frac{dT_e}{dt} = H - C \quad , \quad (4-1)$$

where H and C are, respectively, the heating and cooling rates per electron. The ARCTIC code includes the following basic cooling terms: 1) excitation of  $O^+(^2D)$ ,  $O^+(^2P)$ , 2) excitation of  $O(^1D)$ ,  $O(^1S)$ ,  $N(^2D)$ ,  $N(^2P)$ , 3) excitation of vibrational states of  $N_2$ , 4) excitation of

vibrational states of  $O_2$ , 5) excitation of fine structure levels of  $O(^3P)$ , 6) rotational excitation of  $N_2, O_2$ . The details of these cooling terms can be found in Reference 1.

In addition to electron cooling by these processes, we have recently added cooling from elastic scattering by  $N_2, O_2, O$  and positive ions. Explicit expressions for the rates ( $eV\text{ cm}^{-3}\text{ sec}^{-1}$ ) are given, from Reference 16, by:

$$C_{N_2} = 1.77 \times 10^{-19} (2/3k) [N_2] (1 - 1.21 \times 10^{-4} T_e) T_e (T_e - T_n) \quad (4-2)$$

$$C_{O_2} = 1.21 \times 10^{-18} (2/3k) [O_2] (1 + 3.6 \times 10^{-2} T_e^{1/2}) T_e^{1/2} (T_e - T_n) \quad (4-3)$$

$$C_O = 7.9 \times 10^{-19} (2/3k) [O] T_e^{1/2} (T_e - T_n) (1 + 5.7 \times 10^{-4} T_e) \quad (4-4)$$

$$C_{\text{ions}} = 5 \times 10^{-7} (2/3k) \frac{T_e - T_n}{T_e^{3/2}} ([O^+] + .5[O_2^+] + .53[NO^+]) \quad (4-5)$$

where  $2/3k = 7.7 \times 10^3 \text{ }^\circ\text{K/eV}$ .

We have also included a cooling term due to heating of the ions. It is given by (Reference 17)

$$C_h = \frac{7.7 \times 10^{-6} (2/3k)}{T_e^{3/2}} \{ (0.5[N_2^+] + [N^+])/14 + (0.5[O_2^+] + [O^+])/16 + [NO^+]/30 \} (T_e - T_n) \quad (4-6)$$

The heating term is determined primarily from the bombarding flux and is given by

$$H = 7.7 \times 10^3 \frac{d\mathcal{E}_e}{dt} \frac{1}{n_e} \quad (4-7)$$

where  $d\mathcal{E}_e/dt$  is the rate energy is deposited in the electron gas. It is determined from the expression

$$\frac{d\mathcal{E}_e}{dt} = \int_0^{\infty} \phi(E) L_e(E, T_e) dE \quad (4-8)$$

where  $\phi(E)$  represents the net steady state flux (both primaries and secondaries) and  $L_e$  is the electron loss function (see Appendix A). In addition, heating of the electron gas also occurs due to deexcitation of  $O^+(^2D)$ ,  $O^+(^2P)$ ,  $O(^1D)$ ,  $O(^1S)$ ,  $N(^2D)$ , and  $N(^2P)$ . However, except for deexcitation of  $N(^2D)$  at high altitudes ( $\sim 200$  km), these heating terms involve only small energy transfer. Furthermore, not all of the energy of the ejected electron ends up in the ambient electron gas. Appendix B gives a description of how we partition the ejected electron energy.

#### OLD SOLUTION TO EQUATION 4-1

In order to solve Equation 4-1 for  $T_e$ , we have to solve Equations 4-7 and 4-8 for the heating terms. If this is done every numerical time step in the chemistry code, it becomes prohibitively expensive. Therefore, approximate solutions are usually adopted for Equations 4-7 and 4-8. In Appendix A we show that the usual approximation made (see also Reference 17) is

$$\frac{d\mathcal{E}_e}{dt} = f_e \delta \frac{d\mathcal{E}_t}{dt} \quad (4-9)$$

where  $f_e$  is the fractional ionization,  $\delta$  is a constant, and  $d\mathcal{E}_t/dt$  is the total energy deposition rate. Since the fractional ionization is given by  $n_e/A$ , where  $A$  is the total particle concentration, Equation 4-7 becomes

$$H = 7.7 \times 10^3 \frac{\delta}{A} \frac{d\mathcal{E}_t}{dt} \quad (4-10)$$

Thus, with approximation 4-9, the heating rate per electron is independent of the electron density.

This is the assumption previously made in the ARCTIC code and, as far as we are aware, by all other workers in the field. At a given altitude, the code would perform a detailed calculation of  $\delta$  for a given electron density and would assume the validity of Equation 4-10 during the temperature and chemistry calculation while the electron density varied. Since the cooling rate is also independent of the electron density, the electron temperature was then also independent of the electron density. Under this approximation, the solution to Equation 4-1 can be represented schematically as shown in Figure 4-1. We see that it exhibits a monotonic rise following onset of particle bombardment until it reaches a constant steady state value  $T_{ss}$ .  $T_{ss}$  can be found by setting Equation 4-1 to

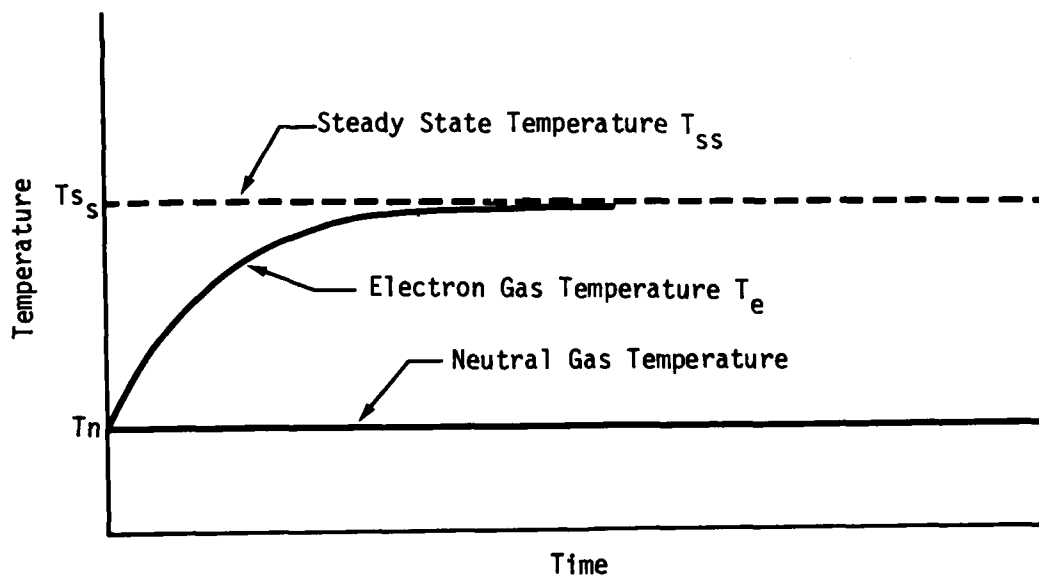


Figure 4-1. Behavior of  $T_e$  and  $T_{ss}$  under approximations 4-9 and 4-10.

zero. Often the monotonic rise can be represented by an exponential rise with a time constant given by

$$\tau = \left[ \frac{\partial C}{\partial T_e} \Big|_{T_e = T_{ss}} \right]^{-1} \quad (4-11)$$

In the ARCTIC code, detailed account was taken of the rise portion of Figure 4-1. However, once the electron temperature reached  $T_{ss}$ , we set it equal to  $T_{ss}$  for all subsequent times. As mentioned above, this procedure has resulted in gross errors.

#### NEW SOLUTION TO EQUATION 4-1

A detailed study of the validity of Equations 4-9 and 4-10 has been made. This work is reported in Appendix A. Basically, the results of this study show that Equations 4-9 and 4-10 hold for  $f_e < 10^{-9}$ . For  $10^{-9} \leq f_e \leq 10^{-6}$ , the partition of energy into the electron gas becomes very complex. For  $f_e > 10^{-6}$ , however, the deposition can again be represented simply by (see Appendix A):

$$\frac{d\mathcal{E}_e}{dt} \approx \alpha f_e^{.25} d\mathcal{E}_t/dt ; \quad f_e > 10^{-6} \quad (4-12)$$

This alteration of form is of more than passing interest since fractional ionizations of  $10^{-6}$  and above occur quite commonly at altitudes  $\geq 200$  km.

Using Equation 4-12, we can now write the heating rate per electron as

$$H = \frac{7.7 \times 10^3 \alpha}{A n_e^{.75}} d\mathcal{E}_t/dt \quad (4-13)$$

Equation 4-13 tells us that while the total energy deposition rate in the electron gas increases as the electron density increases, the heating rate per electron actually decreases as the electron density increases. This is in contrast to the previous result (Equation 4-10) where it remained constant. Similarly, the steady state temperature,  $T_{ss}$ , will be a function of  $n_e$ , increasing with decreasing  $n_e$ .

The dynamic solution to Equation 4-1 for the electron temperature, under conditions where Equation 4-12 is valid, is represented schematically in Figure 4-2. We see that, as in Figure 4-1, there is an initial temperature rise but, unlike that in Figure 4-1, the temperature ultimately reaches a maximum and then subsequently decays. This behavior can be understood qualitatively by writing the solution to Equation 4-1 as

$$T_e \approx (T_{e_0} - T_{ss})e^{-t/\tau} + T_{ss} \quad , \quad (4-14)$$

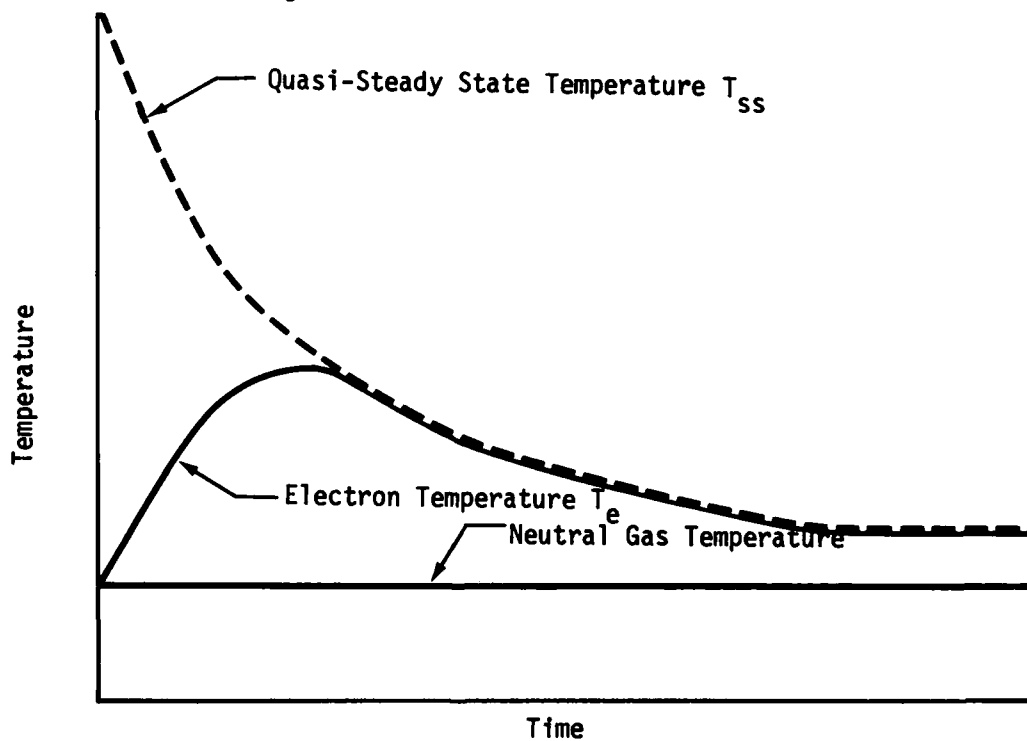


Figure 4-2. Behavior of  $T_e$  and  $T_{ss}$  using Equation 4-12 and 4-13.

where  $\tau$  is determined from Equation 4-11 and  $T_{ss}$  is the solution to

$$H = C(T_{ss}) \quad . \quad (4-15)$$

A schematic plot of  $T_{ss}$  is also shown in Figure 4-2.

Initially, in Figure 4-2, the electron temperature rises because the bombarding flux heats the gas. This is represented by the exponential term in Equation 4-14. The rise time,  $\tau$ , can vary from  $10^{-4}$  sec at 100 km to seconds at 200 km. During this rise time, however, the electron density is increasing. This increase results in a decrease of the steady state electron temperature and, subsequently, once  $T_e$  reaches  $T_{ss}$ , to a decay of  $T_e$ . The decay of  $T_e$  is almost entirely governed by the time constant for electron density buildup which is usually longer than the time constant of Equation 4-11.

Figures 4-3 and 4-4 present the results of calculations at several different altitudes (using Equation A-28 of Appendix A for the partition function) for two different input spectra. Figure 4-3 shows the electron temperature at 100, 132 and 194 km, as functions of time, under electron flux conditions corresponding to the '75 Multi arc (Section 2). We see that the qualitative behavior expected (Figure 4-2) is indeed borne out. Further, we see that at quite low altitudes (132 km) the transient electron temperature can easily reach large values ( $2000^\circ\text{K}$ ) before decaying away. Figure 4-4 presents the same information for the background drizzle appropriate to the '74 Multi event (Reference 4). The energy input from this spectrum is much less than for the '75 Multi arc, but even here we see some transient behavior as in Figure 4-2.

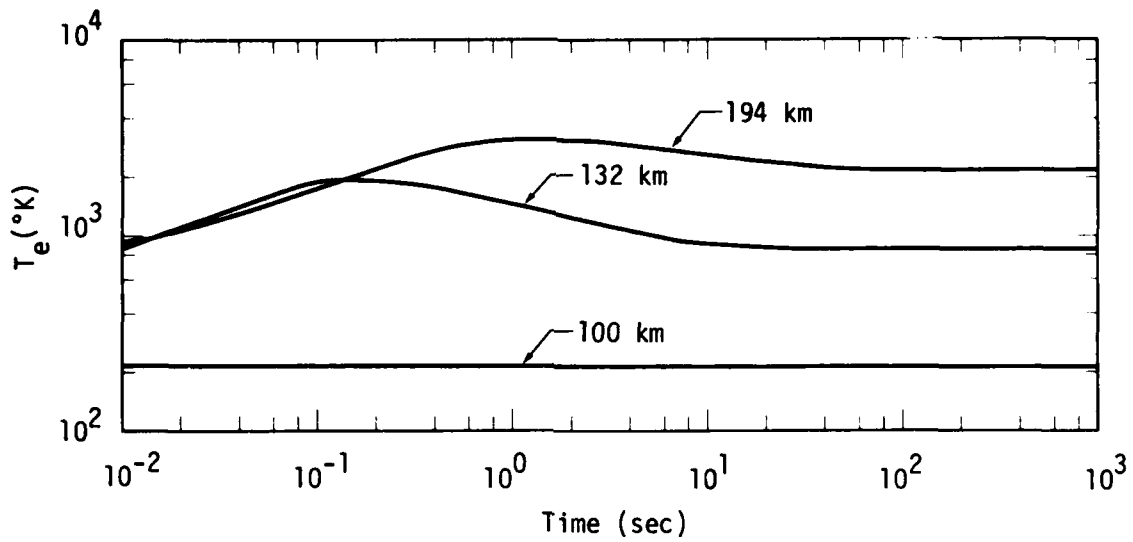


Figure 4-3. Calculated electron temperature in '75 Multi arc as function of time for three different altitudes.

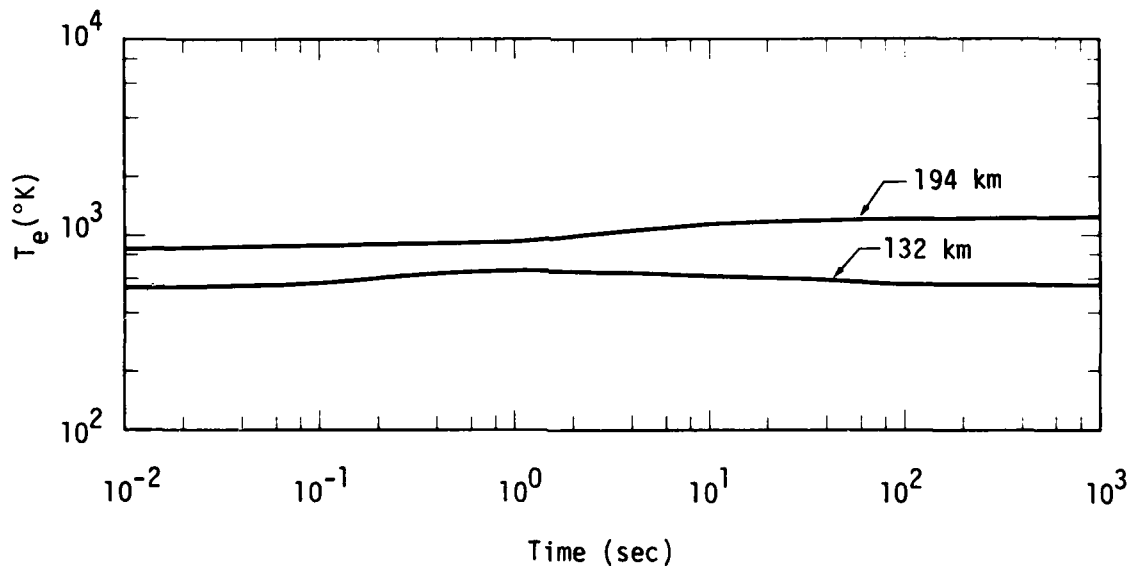


Figure 4-4. Calculated electron temperature in '74 Multi drizzle as function of time for two different altitudes.

## HEATING BY $N(^2D)$ QUENCHING

As mentioned earlier, deexcitation of excited atomic states by the electron gas will also contribute to the heating rate. The reactions are typically of the type



where the recoil electron can be approximated as having an energy equal to the energy of the excited state  $x^*$ . The additional energy carried by the "hot" electron  $e^*$  will now be deposited in the gas. Some of this energy will go into thermal excitation of the electron gas. The partition of the energy deposited by these low energy electrons, incorporated in the ARCTIC code, is given in detail in Appendix B.

For most states, the additional heating due to reactions like 4-16 is very small and can be neglected. However, for  $N(^2D)$  the de-excitation reaction



can play a significant role at high altitudes. In fact, in Appendix B we show that virtually all of the energy of the hot electron goes into thermal energy. Therefore, the rate at which energy is being added to the thermal electron gas is

$$(d\mathcal{E}/dt)_{N(^2D)} \approx 2.38K[N(^2D)]n_e \quad (\text{eV cm}^{-3} \text{ sec}^{-1}) \quad (4-18)$$

and the heating rate due to deexcitation of  $N(^2D)$  can be written, using Equation 4-7, as

$$H = 1.83 \times 10^4 K [N(^2D)] \quad (\text{eV cm}^{-3} \text{ sec}^{-1}) \quad (4-19)$$

In Figure 4-5 we have plotted the fraction,  $f$ , of the total heating rate that arises from deexcitation of  $N(^2D)$ . It is defined as

$$f = \frac{H(N(^2D))}{H(N(^2D)) + H(\text{bombarding flux})} \quad (4-20)$$

The results in Figure 4-5 are for the '75 Multi arc at an altitude of 194 km. They show that  $f$  varies from insignificant amounts at times less than 10 sec to a value in excess of 20 percent of the total heating rate in steady state. We would expect from Equation 4-20 that it would follow the  $N(^2D)$  concentration closely, and indeed it does, as can also be seen in Figure 4-5. Of course the bombarding flux is still the ultimate energy source for electron heating. What we have shown, however, is that indirect processes can, at times, become significant in determining the electron temperature.

#### COMPARISONS WITH SRI RADAR DATA

The foregoing procedures were incorporated into the ARCTIC code. New runs were then made for a variety of auroral input conditions. The resulting electron temperatures, as functions of altitude, are shown by the solid curves in Figure 4-6. Also shown (dashed curve) are the neutral gas temperature and several data points inferred from the SRI incoherent backscatter radar. The only common auroral events that can be used for comparison are those on 27 March 1973 ('73 Multi) and 25 February 1974 ('74 Multi).

For the '73 Multi event, the calculations give, for an altitude of 175 km, arc and drizzle temperatures of 1360 °K and 900 °K, respectively, compared with a radar value of 1250 °K. For the '74 Multi event, the calculations give, for an altitude of 170 km, arc and drizzle temperatures of 1600 °K and 1030 °K, respectively, compared with a radar value of 1300 °K.

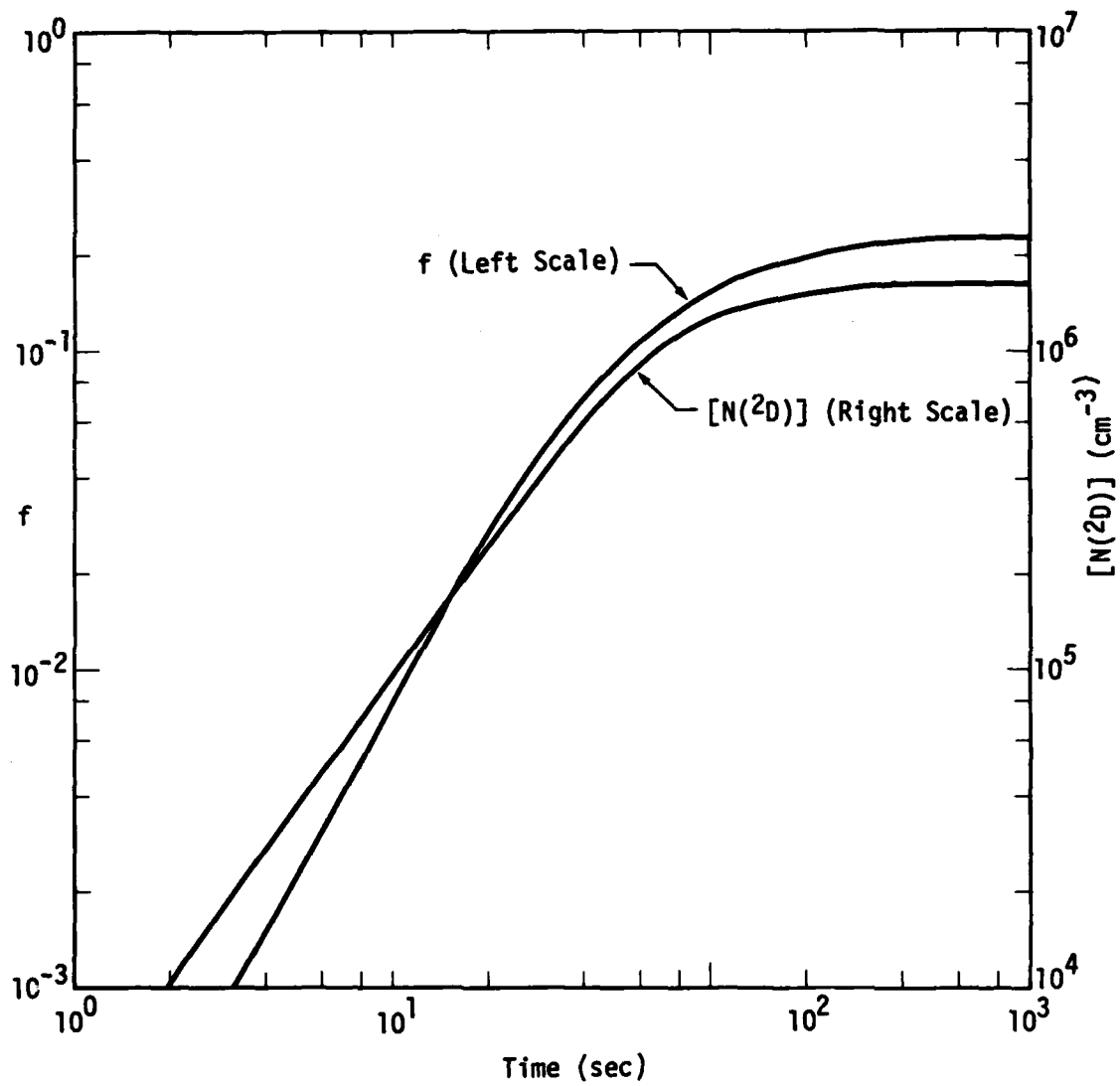


Figure 4-5. Fraction,  $f$ , of total electron heating rate at 194 km due to deexcitation of  $N(2D)$  after onset of '75 Multi arc flux.

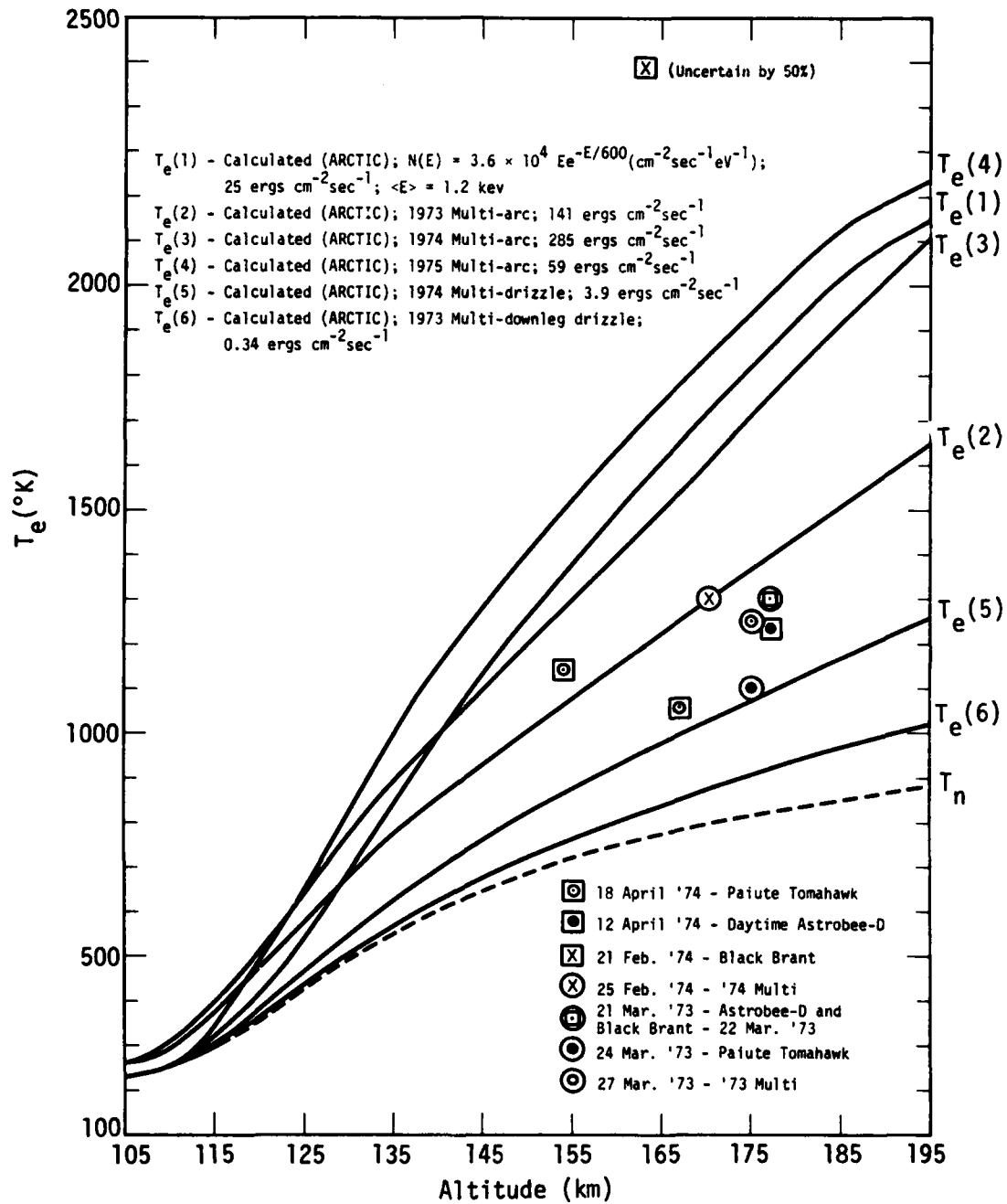


Figure 4-6. Electron temperature calculations compared with SRI radar data.

Since the radar measurements may correspond to conditions either inside or outside the arc, or to a combination of both, it is perhaps reasonable that the data should fall between the calculated arc and drizzle values, as indeed it does for both of these events.

SECTION 5  
NO IN THE AURORAL ENVIRONMENT

PRELIMINARY

Enhancement of the NO concentration in an auroral environment has been reported by a number of workers (see, for example, References 18, 19, and 20). In an earlier report (Reference 2), we also inferred enhanced values for [NO] based on ion mass spectrometer measurements for the ICECAP event of 27 March 1973. Furthermore, it is difficult to account for the ICECAP data near 5.3  $\mu\text{m}$  unless we attribute it to the presence of an enhanced NO profile.

With the exception of the neutral mass spectrometer measurements of Zipf, et al. (Reference 18), most measurements on NO concentrations in auroras are indirect. We have taken the relevant ICECAP data and have attempted to infer NO profiles on the basis of two different methods, neither of which is very reliable. However, although the uncertainties are large, the results unambiguously support the presence of NO concentrations considerably larger than those reported at lower latitudes. The results of this work are reported here.

[NO] INFERRED FROM SLOPE OF 5.3- $\mu\text{m}$  ZENITH INTENSITY PROFILES

The basis for this method of inferring [NO] profiles is the observation that most of the ICECAP data on zenith intensities at 5.3  $\mu\text{m}$  are, for a given event, essentially independent of whether the sight path intersects an auroral arc or not. An exception to this rule may occur only for very

intense events. The only way we have been able to account for these observations is to assume that the NO concentration is uniformly enhanced both outside and inside the arc. Excitation of the NO(v=1) state then occurs by a combination of the atom interchange reaction



and earthshine scatter by NO. For sufficiently enhanced concentrations of NO, this emission dominates the NO chemiluminescence contribution, except possibly in very intense arcs.

To the extent that this view is correct, one can then infer an NO concentration by noting that it is proportional to the volume emission rate in the NO fundamental band near 5.3  $\mu\text{m}$ , especially outside arcs. Mathematically, since  $\dot{\phi}(z)$ , the volume emission rate at altitude  $z$ , is related to  $I(z)$ , the zenith intensity, by

$$I(z) = \int_z^{\infty} \dot{\phi} dz \quad , \quad (5-2)$$

we have

$$\dot{\phi}(z) = - \frac{dI(z)}{dz} \quad . \quad (5-3)$$

But under conditions where the excitation of NO(v=1) occurs entirely by atom interchange + earthshine scatter, we have

$$\dot{\phi} = (k[\text{O}] + \eta) [\text{NO}] \quad (5-4)$$

where  $k$  is the rate coefficient for Reaction 5-1 and  $\eta$  is the earthshine excitation rate per NO molecule. Equations 5-3 and 5-4 then lead to the result

$$[\text{NO}] = \frac{-(dI/dz)}{(k[\text{O}] + \eta)} \quad . \quad (5-5)$$

Normally, the measuring instrument has limited bandwidth so that only a fraction,  $f$ , of the emitted photons are detectable. Thus, if  $(dI/dz)'$  is the slope of the measured intensity profile, Equation 5-5 can be written as

$$[NO] = \frac{-(dI/dz)'}{f(k[O] + \eta)} \quad (5-6)$$

Equation 5-6 has been used to estimate NO profiles for three different auroral events. The results are shown in Figure 5-1. They are based on radiometer data obtained on descent through drizzle regions by Rockets A18.205-1 ('73 Multi) and IC519.07-1B ('75 Multi) and by Rocket IC507.11-2A during the intense auroral breakup event of 10 March 1975. Values used for the parameters appearing in Equation 5-6 are (see Reference 4):  $f = 0.75$ ,  $\eta = 3.38 \times 10^{-4}$ ,  $k = 5 \times 10^{-13} T^{0.5} e^{-3196/T}$ . Also shown in Figure 5-1 (dashed curve) is a mid latitude profile obtained from References 21 and 22.

The uncertainty associated with the profiles shown in Figure 5-1 is large because of the difficulty in accurately determining the slope,  $(dI/dz)'$ , of the measured intensity profiles, and because of uncertainties in the values of  $k$  and  $\eta$ . Factors of 2 or more in uncertainty of the inferred NO values would not be unreasonable.

Application of this method to the drizzle environments appropriate to the descent airspace of the '73 and '75 Multi rockets seems reasonable since NO chemiluminescence should be small. However, one might question its use for the intense auroral breakup event of 10 March 1975 in which chemiluminescence would be expected to contribute significantly. The only justification is based on the following facts (see Section 3): (1) the measured zenith intensity in the radiometer band, centered near  $5.6 \mu\text{m}$ ,

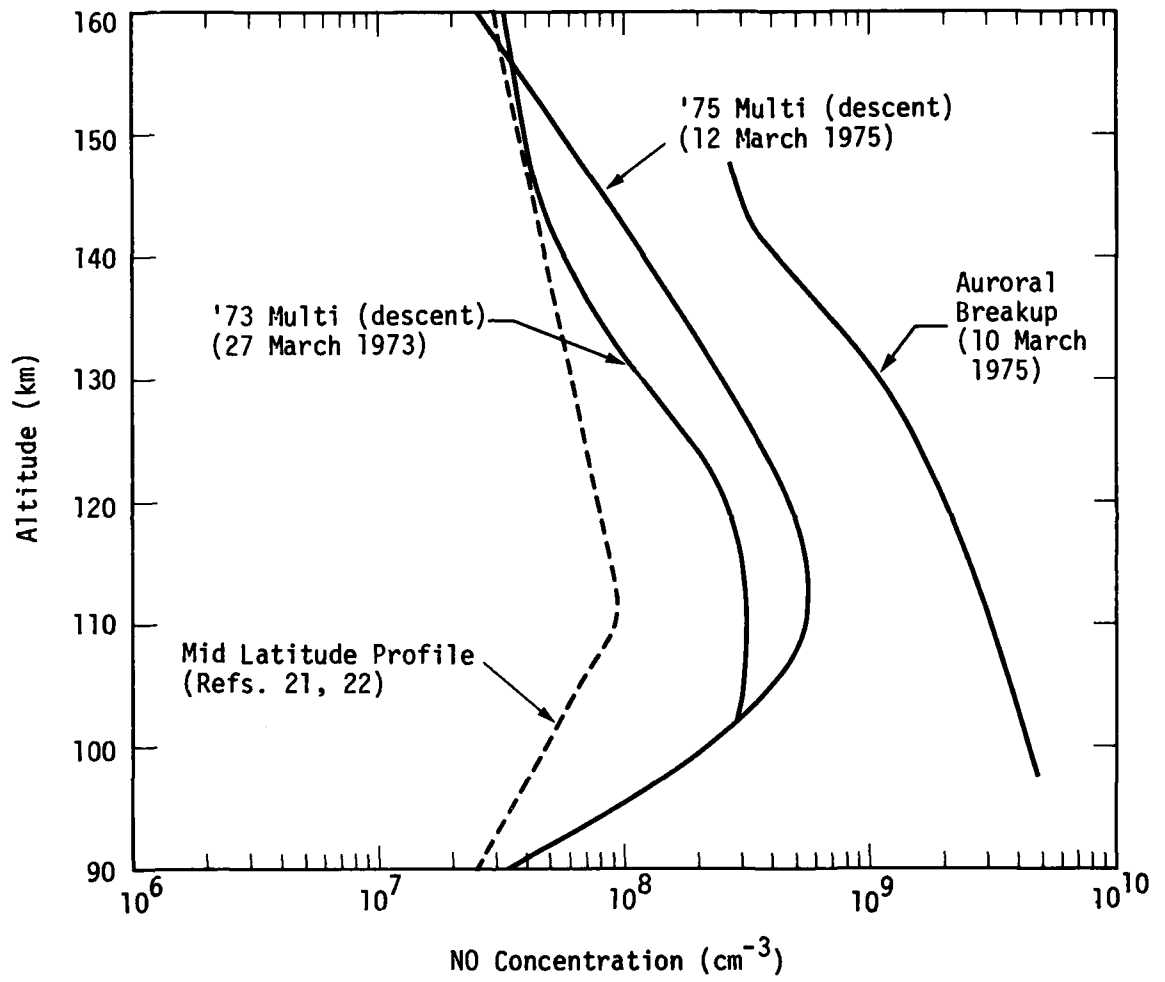


Figure 5-1. Auroral NO concentrations inferred from slope of 5.3- $\mu$ m radiometer data.

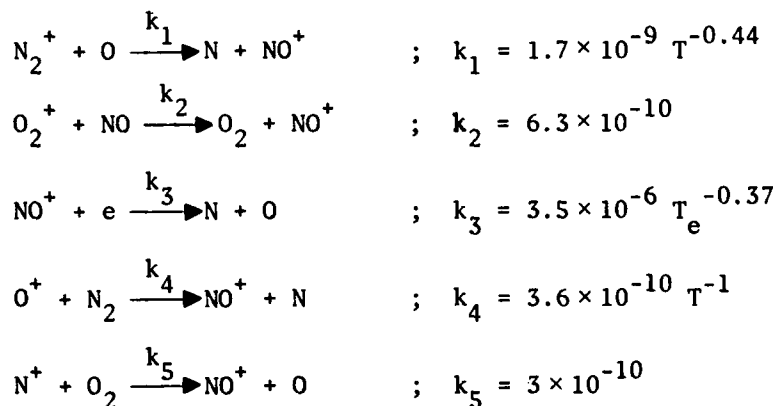
is nearly the same on rocket ascent and descent,\* (2) the computed chemi-luminescence is too small to account for the data, and (3) the CVF spectra support the view that the dominant emission is the (1,0) band of NO.

#### [NO] INFERRED FROM ION MASS SPECTROMETER MEASUREMENTS

It can be shown (see, for example, Reference 19) that in steady state the NO concentration can be determined from measured ratios of the ion concentrations by the expression

$$[\text{NO}] = \frac{k_3}{k_2} n_e \left( \frac{[\text{NO}^+]}{[\text{O}_2^+]} \right) - \frac{k_1}{k_2} [\text{O}] \left( \frac{[\text{N}_2^+]}{[\text{O}_2^+]} \right) - \frac{k_4}{k_2} [\text{N}_2] \left( \frac{[\text{O}^+]}{[\text{O}_2^+]} \right) - \frac{k_5}{k_2} [\text{O}_2] \left( \frac{[\text{N}^+]}{[\text{O}_2^+]} \right) \quad (5-7)$$

Here, the k's are rate constants for the reactions:



and  $n_e$  is the electron density.

\* Actually, we don't know if the particle precipitation on rocket descent was significantly less than on ascent because the SRI radar was not operated in a meridian scan mode during the rocket flight but, rather, was pointed at the anticipated 100-km altitude rocket entry point.

We have used Equation 5-7, together with measured (Reference 23) ion mass spectrometer values for the ion concentration ratios, and retarding potential analyzer values for  $n_e$ , to determine [NO] profiles on ascent and descent of the '73 Multi Rocket A18.205-1 on 27 March 1973. Values for the neutral species concentrations were taken from the 1965 Cira mean model (Model 5, hour 0 above 120 km), and values for the electron temperature, obtained from the ARCTIC code, are shown by the appropriate curves in Figure 4-6. The results are shown in Figure 5-2.

The jagged appearance of the curves in Figure 5-2 arises from the fact that in Equation 5-7 we used the actual values of the ion ratios that exhibit jagged profiles due to spin modulation of the rocket.

A similar calculation has been performed by Narcisi and Swider (Reference 20) for the ascent portion of the rocket flight, using smoothed versions of their ion concentration ratios. Their results, for the Cira 1965 atmosphere, match ours at 110 km, but fall off faster with increasing altitude. We attribute the difference to their use of different rate constants, to their equating the electron and neutral temperatures and, perhaps, to their use of somewhat different neutral species concentrations.

Uncertainty in the calculated NO profile, using Equation 5-7, can arise for at least two reasons. First, when the terms in Equation 5-7 are of comparable magnitude, especially the first two, small variations in the magnitude of their factors produce large changes in the resulting NO concentration. Second, the equation is valid only in the steady state, a condition that does not generally prevail in a dynamic auroral environment.

Also shown in Figure 5-2 (smooth solid curve) for comparison, is the descent NO profile from Figure 5-1 obtained by taking the slope of the 5.3- $\mu$ m radiometer data. Over the altitude range from 105 to 140 km,

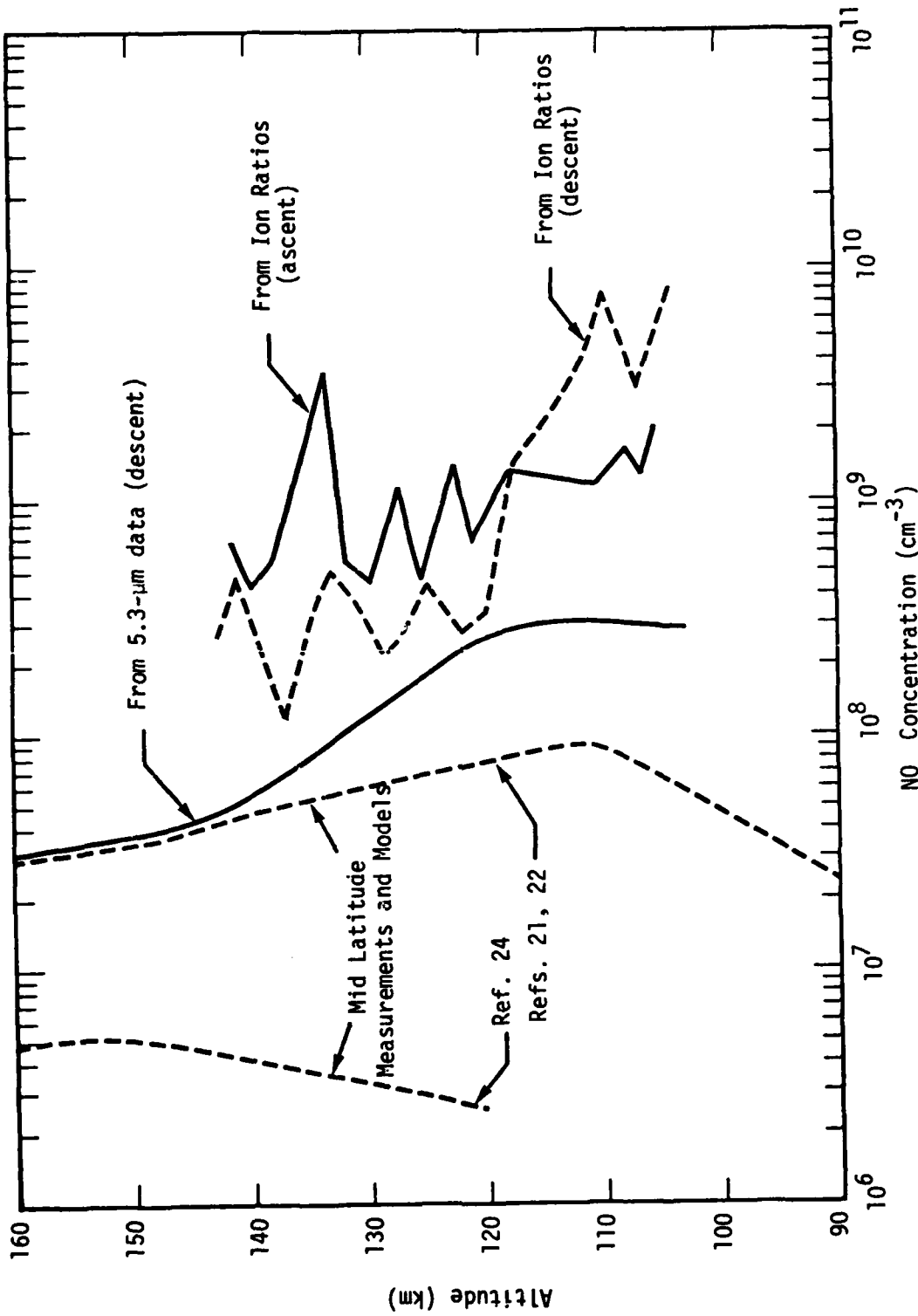


Figure 5-2. NO Concentration inferred from auroral data of 27 March 1973 (Rocket A18.205-1).

the latter profile is seen to be smaller than the one obtained by the ion ratio method by factors ranging from about 10 at 110 km to about 3 or so at 140 km.

Two mid latitude profiles (widely different) are also shown in Figure 5-2. In all cases, the aurorally-inferred profiles are considerably enhanced over those at mid latitudes.

#### SUMMARY

Although fraught with considerable uncertainty, two different methods have been used to infer [NO] profiles from ICECAP data. The results are all supportive of considerable auroral enhancement of [NO], especially at altitudes in the 100- to 120-km region.

SECTION 6  
ICECAP SUMMARY AND CONCLUSIONS

PRELIMINARY

This section summarizes the principal results and conclusions of our work, as embodied in this and earlier reports (References 1 through 4), related to the interpretation and understanding of ICECAP data. Emphasis has been on those auroral events for which coordinated measurements were taken with a variety of instruments, especially the short wavelength infrared (SWIR) detectors. Not all aspects of the ICECAP data have been studied, and no attempt is made here to summarize results from the entire ICECAP program, or conclusions reached by other workers.

One of the main purposes of ICECAP was to measure SWIR radiation from an aurorally excited atmosphere and thereby test the validity of models used in computer codes to predict corresponding emissions in a nuclear environment. In this sense the program was at least partially successful. Complete success was hampered by a number of factors, not the least of which is the fact that the experiments had to be carried out in the uncontrolled, dynamic, auroral environment. It is not possible, in such experiments, to measure the input particle flux spectrum over a large enough spatial region and for sufficiently long periods of time to specify adequately the input conditions necessary for accurate calculation of the resulting optical/IR radiances. Ambiguities related to excitation mechanisms and radiating species also exist because of instrumental limitations, especially with respect to spectral coverage and wavelength resolution. In some cases, radiance data at a given wavelength, measured by two different instruments,

may be sufficiently different to render the field values very uncertain. So, for these and other reasons, uncertainty still remains with respect to interpretation of some of the data, and complete verification of the SWIR models is not yet possible.

Our analysis and interpretation of the data was greatly facilitated by the development of the ARCTIC code that inputs the measured spectral flux of auroral electrons and computes in detail the energy deposition and partition as well as the subsequent atmospheric chemistry and optical/IR radiation. Many, although not all, of our conclusions are based on comparisons between these calculations and the field data.

#### PRINCIPAL RESULTS

The following summarizes our results according to the different topics covered. To simplify reference to the different auroral events, we have classified them numerically according to the scheme shown in Table 6-1.

Table 6-1. Classification of auroral events studied.

Event	Event Date and Description	Rocket
1	27 March 1973 (discrete arc)	A18.205-1: Black Brant ('73 Multi)
2	24 March 1973 (auroral breakup)	A10.205-2; Paiute Tomahawk
3	25 February 1974 (discrete arcs)	A18.219-1; Black Brant ('74 Multi)
4	12 March 1974 (discrete arcs)	IC519.07-1B; Sergeant Hydac ('75 Multi)
5	10 March 1975 (auroral breakup)	IC507.11-2A: Nike Hydac

### 5.3- $\mu\text{m}$ Radiation

Radiometer and/or CVF spectrometer data from each of the five events shown in Table 6-1 were analyzed and compared with calculations. The results can be enumerated as follows:

(1) NO chemiluminescence cannot account for any of the data. Its magnitude (too small), its sensitivity to rapid changes in bombardment conditions, and its spectral distribution, are not in accord with the observations.

(2) Although generally differing in magnitude from event to event, the zenith intensity profile near 5.3  $\mu\text{m}$ , for any given event, is nearly the same on rocket ascent and descent, even though the instantaneous bombardment conditions may be quite different in the upleg and downleg regions. A good example of this behavior is shown in Figure 6-1 for auroral Event 2 (Table 6-1). Although the zenith 3914Å intensity on ascent saturated at 200 kR, the intensity on descent did not exceed about 40 kR (see Reference 4, Figure 3-2). However, at least above 95 km where we have descent data, the 5.3- $\mu\text{m}$  intensity is virtually the same on ascent and descent.

(3) The limited-resolution spectral data are reasonably consistent with (1,0) band radiation from NO.

(4) Excitation of NO( $v=1$ ) by a combination of the atom interchange reaction  $\text{NO}(v=0) + \text{O}^{\prime} \rightarrow \text{NO}(v=1) + \text{O}$  and earthshine scatter appears to be capable of accounting for most of the data. However, these mechanisms do require the presence of considerably enhanced [NO] profiles that differ from event to event. Complete verification of this model would entail an independent measurement of the [NO] profiles as well as a measurement of the rate constant for the atom interchange reaction.

The data at 5.3  $\mu\text{m}$  have produced one of the more surprising outcomes from the ICECAP program. The results have implications for modeling in the nuclear environment that will be mentioned later.

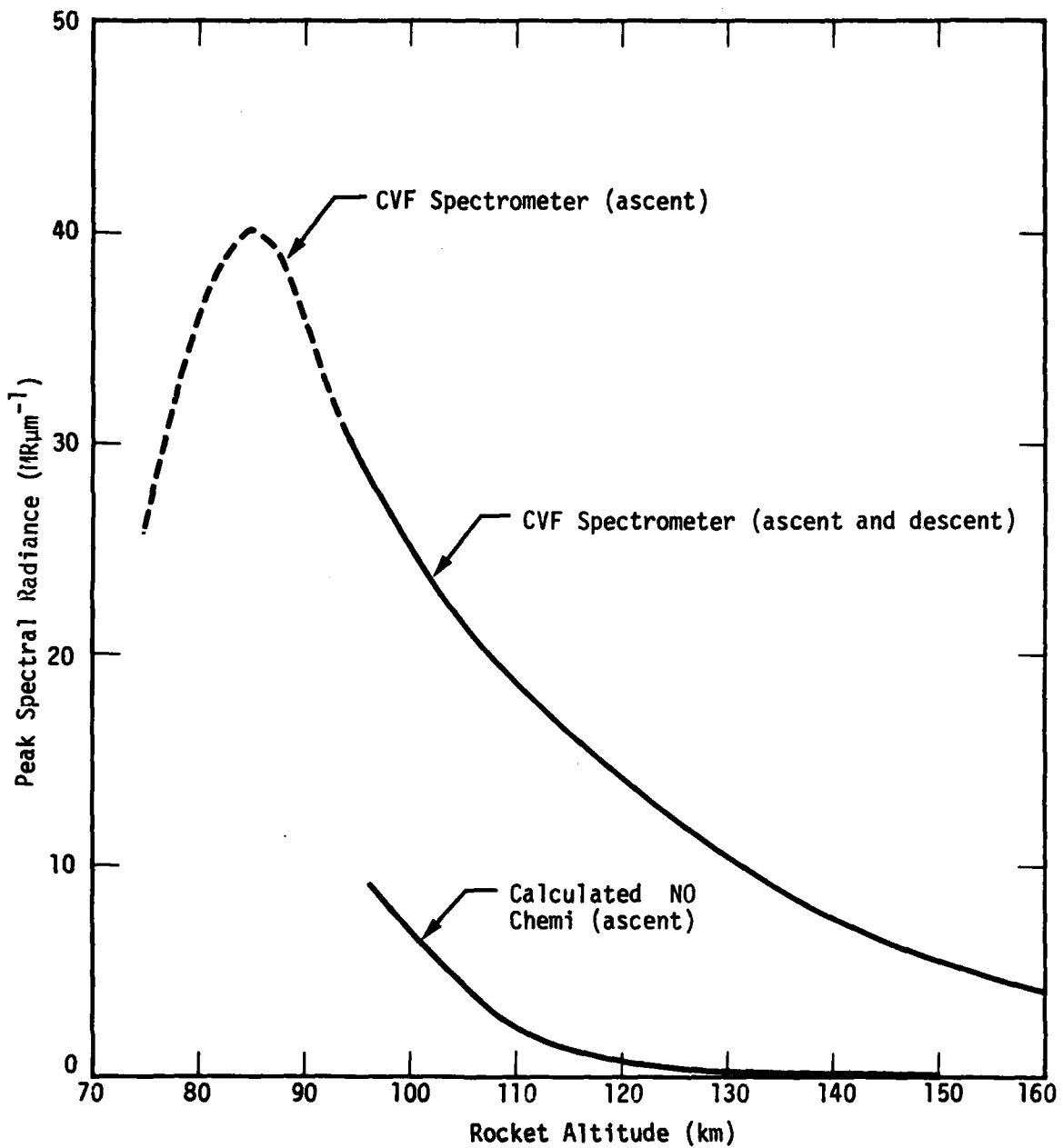


Figure 6-1. Zenith peak spectral radiance near 5.3 µm (Paute Tomahawk A10-205-2).

## 2.7- $\mu\text{m}$ Radiation

The only usable rocket data at 2.7  $\mu\text{m}$  from ICECAP that we are aware of were taken by CVF instruments during Events 2 and 3 (Table 6-1). The CVF data for Event 4 are below the instrument noise level. From study of this very limited amount of data, and comparison with calculations, we find the following:

(1) For Event 2, comparison between the measured zenith intensity at 3914 $\text{\AA}$  and that near 2.7  $\mu\text{m}$ , leads to a fluorescence efficiency for the 2.7- $\mu\text{m}$  band of about 0.5 percent. This is consistent with analyses of aircraft data reported by Kofsky (Reference 25). It is also consistent with our code calculations of NO chemiluminescence that provides for efficiencies at 2.7  $\mu\text{m}$  between about 0.5 and 1 percent.

(2) For Event 2, the magnitude of the measured intensity above 95-km altitude, and the shape of the spectral feature near 2.7  $\mu\text{m}$ , are reasonably consistent (to within a factor of 2 on intensity) with our model of NO chemiluminescence that provides for about one 2.7- $\mu\text{m}$  photon per  $\text{N}(\text{}^2\text{D}) + \text{O}_2$  reaction.

(3) For Event 3, NO chemiluminescence is insufficient to account for the magnitude of the 2.7- $\mu\text{m}$  data available to us. In fact, calculation of the fluorescence efficiency at 2.7  $\mu\text{m}$ , obtained by comparing the CVF data with the 3914 $\text{\AA}$  data, leads to values as high as 50 percent. Therefore, it would appear that either there is a calibration problem with the CVF instrument on this flight, or else we don't understand the radiation mechanism.

For Event 3, the data referred to above were taken on rocket descent about one minute after passage of a strong arc. It has been suggested (Reference 26) that a long-life radiator (perhaps  $\text{CO}_2$ ) is operating near 2.7  $\mu\text{m}$  in the auroral environment. If so, this could account for the observed magnitude of the emission which would have been excited by the earlier passage of the arc. However, the relatively slow decay of the

intensity with increasing altitude above about 90 km, compared with that at 4.3  $\mu\text{m}$ , does not favor  $\text{CO}_2$  as the likely radiator.

In summary then, except for Event 3, the weight of the very limited data (aircraft + one rocket flight) suggest that NO chemiluminescence can account reasonably well for the ICECAP observations near 2.7  $\mu\text{m}$ .

#### 4.3- $\mu\text{m}$ Radiation

Radiometer and/or CVF spectrometer data for the first four events shown in Table 6-1 were studied and compared with calculations involving  $\text{CO}_2$  vibrationaluminescence and  $\text{NO}^+$  chemiluminescence. The results are as follows:

(1) The data are all reasonably consistent with  $\text{CO}_2$  vibrationaluminescence as the main source of 4.3- $\mu\text{m}$  radiation in the auroral environment. Both the magnitude of the intensity and the shape of the spectral features near 4.3  $\mu\text{m}$  support this conclusion. The emission is consistent with the presence of a long-life radiator. Removal of an intense bombardment source (arc) does not immediately reduce the emission intensity as would be the case if the source were primarily  $\text{NO}^+$  chemiluminescence. For this reason, however, detailed agreement between calculations and the field data is difficult to achieve because transport effects, due to winds and diffusion, have time to modify the spatial distribution of the vibrationally excited nitrogen and, hence, the  $\text{CO}_2$  volume emission rate. Knowledge of the bombardment history (for minutes to hours, depending on the altitude) is also essential for correct determination of the vibrationaluminescent intensity.

(2) Unquenched  $\text{NO}^+$  chemiluminescent emission near 4.3  $\mu\text{m}$  is generally in poor agreement with the data, both with respect to the magnitude of the intensity and to the shape of the spectral features. Also, as mentioned above, the observed radiation persists after removal of the bombardment source, and this is not consistent with  $\text{NO}^+$  chemiluminescence.

Data from Event 4 has been used to show that a rate constant as large as  $1 \times 10^{-9} \text{ cm}^3 \text{ sec}^{-1}$  for quenching  $\text{NO}^+$  emission by  $\text{N}_2$  is required. The likely mechanism is v-v transfer from  $\text{NO}^+$  to  $\text{N}_2$  for which there is very close energy resonance.

### NO Concentration

Values for the NO concentration, enhanced by up to 2 orders of magnitude over mid latitude values near 105 km, have been inferred from Events 1, 4, and 5 (Table 6-1). Even larger values for Event 2 are implied by the data in Figure 6-1.

Some of these inferred values (for Event 1) are based on ion mass spectrometer data. The others are based on the assumption that most of the 5.3- $\mu\text{m}$  radiation is excited by the atom interchange reaction + earthshine scatter from NO. To the extent that this is true, the data suggest that the altitude profile of NO is fairly uniform over a large spatial region (perhaps a few hundred km) surrounding a given auroral form. The degree of enhancement appears to be related to the cumulated energy deposited over some period of time, although there does seem to be a correlation with the intensity of the specific event as well. To our knowledge, no one has attempted to take detailed account of the bombardment history, for a given event, over a period of perhaps hours or days, and perform a chemistry calculation to see if the required NO values can indeed be attained. Part of the difficulty in making such a calculation, however, is the unknown influence of transport effects that have ample time to operate and change the NO distribution.

### IMPLICATIONS TO THE NUCLEAR ENVIRONMENT

Application of the foregoing results to a nuclear environment are fairly clear, at least for the 5.3- and 4.3- $\mu\text{m}$  bands.

For the 5.3- $\mu\text{m}$  band, the models should add the contribution from NO radiation due to excitation by the atom interchange reaction and by earth-shine scatter. We have not studied the effect of this addition in detail, but have made estimates for two situations involving high-altitude nuclear detonations. In one case, for a sight path along which there was no significant temperature increase, the effect was to approximately double the calculated radiance due to NO chemiluminescence alone. In the other case, for sight paths external to the fireball, but along which there was significant heating, the atom interchange contribution was greater by up to 2 orders of magnitude than the combined effects of NO thermal and chemiluminescence radiation.

For the 4.3- $\mu\text{m}$  band, CO<sub>2</sub> vibrationaluminescence seems clearly established as the dominant mechanism, at least in regions not heated sufficiently for thermal emission to dominate. However, modeling for the nuclear environment is complicated in two ways. First, as interpretation of the ICECAP data by Kumer (Reference 13) has shown, trapping of the 4.3- $\mu\text{m}$  photons at altitudes below about 100 km is important. This is especially significant in the nuclear environment because much of the X-ray energy is deposited at altitudes near 80 km. Second, because of the long lifetime of the radiation process, the effects due to transport of the vibrationally excited nitrogen by winds and diffusion cannot be ignored. The models must make some provision for incorporating these effects if reasonably reliable predictions are to be made. This is particularly so for the case of a multiburst environment.

For the 2.7- $\mu\text{m}$  band, the results are still in some doubt. At the present time, we would recommend retention of a chemiluminescent model in which about 0.5 percent of the deposited energy is radiated in the first overtone band of NO. Further work is needed to clarify whether or not some other molecule, or excitation mechanism, is contributing significantly to this band, at least at altitudes above about 90 km.

## SECTION 7 COMMUNICATIONS-RELATED WORK

### INTRODUCTION

With DNA's increased emphasis on field programs related to satellite communications, especially the Wideband Satellite experiment, a small part of our present effort was devoted to work in this area.

Satellite communication problems arise largely from radiowave scintillation caused by striations or other irregularities in the F-region ionization. Successful prediction of the irregularity structure and scintillation effects in a nuclear environment depends on a good theoretical understanding of how the irregularities develop. Hopefully, a major step toward this understanding, at least in the non nuclear case, will result from the proper interpretation of the Wideband Satellite transmissions through both the equatorial and high latitude scintillation zones.

Two aspects of the problem, especially as it bears on the interpretation of the Wideband data, were addressed. One relates to the question of how important, in the auroral environment, the perturbing effects due to structure in particle precipitation may be in masking the instability-produced inhomogeneities in the F layer. The other relates to the question of how to measure the F-region neutral wind component normal to the earth's magnetic field at equatorial latitudes. This wind component is the driving force in the so-called "ion-neutral slip" (or "gradient drift") instability mechanism that is believed to generate the striation phenomenon. Although our efforts in these two areas were not very fruitful, they are briefly reported here.

## AURORAL IONIZATION EFFECTS DUE TO STRUCTURED PARTICLE FLUXES

Interpretation of Wideband Satellite scintillation data from the auroral region, in terms of instability-generated F-layer inhomogeneities, could be rendered erroneous if effects due to structure (temporal or spatial) in the auroral particle flux, were to dominate. In this context, we first note that direct effects on F-layer ionization from a structured particle flux should be insignificant because of the long response time of the ionosphere above 250 km. In the E layer, however, ionization irregularities would not be expected to wash out because of the much shorter response time.

We are not referring here to structure associated with discrete arcs. For, although auroral arcs may produce severe radiowave scintillation as the propagation path scans across them, their presence in the Wideband experiment would surely be recognized, either from coordinated optical measurements, or from their characteristic scintillation signature. Rather, the concern was over the possibility of frequent occurrence of random, large amplitude, fluctuations of the incoming particle flux. Such occurrences would then be reflected in corresponding fluctuations in the E-layer ionization that might be misinterpreted in terms of F-layer structure.

We conducted a fairly exhaustive literature survey to uncover what is known about such random flux variations. The outcome of that survey shows that, for the most part, the particle precipitation in regions away from discrete auroral forms is quite uniform. The presence of large amplitude random fluctuations is rare. Consequently, we conclude that the probability that structured particle fluxes will interfere with auroral Wideband data interpretation is small.

## ELECTRON BEAM EXCITATION OF F-REGION ATOMIC OXYGEN

As was mentioned in the Introduction, the force driving the instability mechanism believed responsible for F-region striations is the neutral wind component normal to the earth's magnetic field. A suggested method for measuring this wind component is to excite one or more lines in the visible spectrum of atomic oxygen by an in situ electron beam and to measure the doppler shift in the lines by utilizing a ground-based Fabry Perot interferometer. The following paragraphs describe the results of a study made, using the ARCTIC code, to assess the utility of such an experiment at equatorial latitudes. They show why we feel that the technique is not feasible.

### Deposition and Partition by 325 eV Electrons at 300-km Altitude

The ARCTIC code was run to determine the deposition volume and the partition of the energy for an electron beam of various initial energies at an altitude of 300 km at the magnetic equator. Because of the low air density at 300 km, the range of keV electrons is very large ( $\approx 2.7 \times 10^3$  km), and it is necessary to go to lower electron energies in order to have a higher volume deposition rate. The results presented below are for a 325 eV electron beam.

The code results show that the deposition volume can be described approximately as a cylinder 320 km long by 30 m in diameter, for a total volume of  $2.25 \times 10^{14}$  cm<sup>3</sup>.

### PERMITTED TRANSITIONS

The energy deposited in the various states of atomic oxygen depends on the ambient electron density. The higher the ambient ionization, the more energy is imparted to it by the electron beam, and the less energy is available

for atomic excitation. Table 7-1 shows the computed emission in several permitted lines of atomic oxygen for three different values of the ambient electron density. The results in the last six columns are for a beam current of 1 ampere, and the intensity is in Rayleighs.

The intensities shown in Table 7-1 were computed for a path length of 30 m, corresponding to the diameter of the cylindrical deposition volume. This is appropriate for a viewing geometry that includes a ground-based interferometer located near the magnetic equator where the long axis of the cylinder is parallel to the earth's surface.

The intensities in Table 7-1 need to be compared with the airglow background, at the corresponding wavelengths, that arises from radiative recombination of  $O^+$  in the F layer. For estimating the backgrounds, we have used radiative recombination values quoted by Tinsley et al. (Reference 27) for an electron temperature of 2000 °K. These values are shown in Table 7-2.

The volume emission rate is given by the equation

$$\dot{\phi} = \alpha n_e^2 \text{ (photons cm}^{-3} \text{ sec}^{-1}\text{)} \quad , \quad (7-1)$$

and the brightness, for a path length  $L$ , is then

$$B = L \alpha n_e^2 \quad (7-2)$$

provided the medium is optically thin.

For a vertical path length of 200 km, the computed airglow intensities, for the wavelengths corresponding to those in Table 7-1, are shown in Table 7-3. Intensities as high as 200 R at 7774Å in the equatorial anomaly region have been reported (Reference 28). The values shown in the last column of Table 7-3, are not atypical of what the background intensity is likely to be in an electron beam experiment near the equator.

Table 7-1 Photon emission rate in various permitted lines of atomic oxygen at 300-km altitude by a 325 eV electron beam of unit ampere current.

Wavelength (Å)	Photons Per eV Deposited		Photons cm <sup>-3</sup> sec <sup>-1</sup> amp <sup>-1</sup>		Intensity Per Ampere for 30 m Path (R)	
	n <sub>e</sub> = 10 <sup>5</sup>	10 <sup>6</sup> 5 × 10 <sup>6</sup>	n <sub>e</sub> = 10 <sup>5</sup>	10 <sup>6</sup> 5 × 10 <sup>6</sup>	n <sub>e</sub> = 10 <sup>5</sup>	10 <sup>6</sup> 5 × 10 <sup>6</sup>
1304	3.8 <sup>-3</sup>	1.6 <sup>-3</sup> 1.1 <sup>-3</sup>	3.2 <sup>4</sup>	1.4 <sup>4</sup> 9.3 <sup>3</sup>	*9.6 <sup>1</sup>	4.1 <sup>1</sup> 2.8 <sup>1</sup>
1356	2.4 <sup>-4</sup>	8.7 <sup>-5</sup> 5.6 <sup>-5</sup>	2.0 <sup>3</sup>	7.3 <sup>2</sup> 4.7 <sup>2</sup>	*6.1	2.2 1.4
4368	2.8 <sup>-6</sup>	1.2 <sup>-6</sup> 8.9 <sup>-7</sup>	2.4 <sup>1</sup>	1.0 <sup>1</sup> 7.5	7.1 <sup>-2</sup>	3.0 <sup>-2</sup> 2.3 <sup>-2</sup>
7774	5.3 <sup>-5</sup>	2.1 <sup>-5</sup> 1.4 <sup>-5</sup>	4.5 <sup>2</sup>	1.8 <sup>2</sup> 1.2 <sup>2</sup>	*1.3	5.3 <sup>-1</sup> 3.5 <sup>-1</sup>
8446	8.4 <sup>-4</sup>	3.7 <sup>-4</sup> 2.8 <sup>-4</sup>	7.1 <sup>3</sup>	3.1 <sup>3</sup> 2.4 <sup>3</sup>	*2.1 <sup>1</sup>	9.4 7.1

\* Includes contributions from cascade.

Table 7-2. Radiative recombination rate constants for the process O<sup>+</sup> + e → O + hv at T<sub>e</sub> = 2000 °K (from Reference 27).

λ(Å)	1304	1356	4368	7774	8446
α(cm <sup>3</sup> sec <sup>-1</sup> )	2.4 <sup>-13</sup>	4.8 <sup>-13</sup>	5.0 <sup>-15</sup>	3.4 <sup>-13</sup>	1.5 <sup>-13</sup>

Table 7-3. Computed airglow intensity for 200-km vertical path and selected values of ambient electron density.

Wavelength (Å)	$n_e =$	Intensity (R)		
		$10^5$	$10^6$	$5 \times 10^6$
1304		$4.8^{-2}$	4.8	$1.2^2$
1356		$9.6^{-2}$	9.6	$2.4^2$
4368		$1.0^{-3}$	$1.0^{-1}$	2.5
7774		$6.8^{-2}$	6.8	$1.7^2$
8446		$3.0^{-2}$	3.0	$7.5^1$

A comparison between the last column in Tables 7-1 and 7-3 shows that for an electron beam current of 1 ampere, the airglow background at each wavelength is likely to be considerably higher than the intensity generated by the beam. Only if we could increase the beam current to values between 10 and 100 amps could the signal to background ratio become acceptable.\* However, such currents for an electron energy of 325 eV appear to be unreasonably large because of space-charge limitations. For example, in Project EXCEDE, the typical beam current attained at a 3-keV energy is 10 amps. Assuming the current is space-charge limited, so that the current varies as (voltage)<sup>3/2</sup>, then for a potential of 325 volts the current is only about 0.4 amps.

The conclusion is that electron beam excitation of permitted lines of atomic oxygen at 300-km altitude provides too weak a source, relative to the night glow background, for measurement of doppler shifts.

\* Even this assumes that the electron-excited emission volume completely fills the sensor field of view, which is unlikely because a 30 m region viewed from a range of 300 km would require an angular field of only  $6 \times 10^{-3}$  degrees.

## FORBIDDEN TRANSITIONS

We have looked at one other line of atomic oxygen, namely the forbidden transition  $^1D-^3P$  at  $6300\text{\AA}$ . The  $^1D$  state has a lifetime of 110 sec and so the emitting region may consist of an afterglow trail considerably longer than the 30-m diameter of the deposition cylinder. Consider, for example, the geometrical arrangement depicted in Figure 7-1. Here, the rocket trajectory lies in a plane normal to the earth's magnetic field. The instantaneous deposition volume is still a cylinder along the field lines (normal to the page), but the emitting region will be the volume swept out by the cylinder as it moves down along the rocket trajectory. The effective path length through the region, as seen by a sensor looking up the rocket trajectory, is the distance the rocket moves during some fraction ( $\geq 0.5$ ) of the radiative lifetime of  $O(^1D)$ .

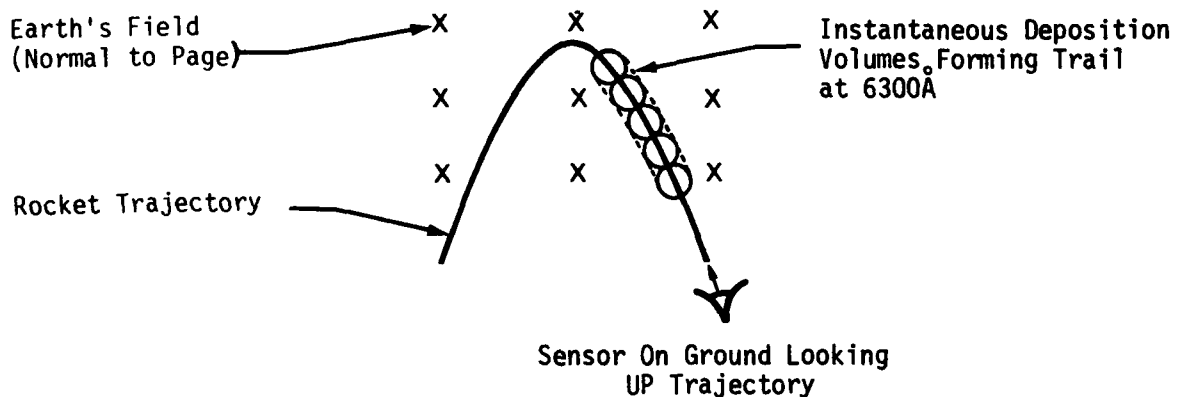


Figure 7-1. Depicting geometrical arrangement for viewing  $6300\text{\AA}$  emission from ground.

We estimate the brightness seen from the ground as follows. If  $P$  is the production rate of  $O(^1D)$  by the electron beam, then in the absence of quenching, which is negligible at 300-km altitude,

$$\frac{d[O(^1D)]}{dt} = P - A[O(^1D)] \quad (7-3)$$

where  $A$  is the radiative transition probability ( $\approx 1/110 \text{ sec}^{-1}$ ). Thus, while the beam is on,

$$[O(^1D)] = \frac{P}{A} (1 - e^{-At}) \quad (7-4)$$

But, because of rocket motion, any volume element will be irradiated for only a short time,  $\Delta t$ , during which the concentration of  $O(^1D)$  will build up to the maximum value  $P\Delta t$  and then decay by radiation according to the equation

$$[O(^1D)] = P\Delta t e^{-At} \quad (7-5)$$

As an approximation, assume that a volume element at a maximum distance,  $L$ , behind the rocket still contributes to the emission when the radiation from it is down by a factor of 2 from its peak; that is, when  $e^{-At_1} = 1/2$ . For  $1/A = 110 \text{ sec}$ , the time,  $t_1$ , required to satisfy this condition is 76 sec. The effective path length through the emitting region is

$$L = v t_1 \quad (7-6)$$

where  $v$  is the rocket velocity, and so the brightness is

$$B \approx \frac{1}{2} A v t_1 P\Delta t \quad (7-7)$$

But  $\Delta t$ , the irradiation time, is the time taken for the rocket to traverse the diameter,  $D$ , of the deposition cylinder. That is

$$\Delta t = \frac{D}{v} \quad (7-8)$$

Thus,

$$B \approx \frac{1}{2} A D P t_1 \quad (\text{photons cm}^{-2} \text{ sec}^{-1}) \quad (7-9)$$

For  $A = 1/110$ ,  $D = 3 \times 10^3$ ,  $t_1 = 76$ , we get

$$B \approx 1 \times 10^{-3} P \quad (\text{Rayleighs}) \quad (7-10)$$

Equation 7-10 was used, along with the production rates of  $O(^1D)$  computed for three different values of the ambient electron density, to calculate the brightness of  $6300\text{\AA}$  emission. The results are shown in Table 7-4.

The intensities shown in Table 7-4 are to be compared with the tropical night glow at  $6300\text{\AA}$ , typical values for which are 400 to 800 Rayleighs (Reference 27). It is clear, therefore, that the beam-induced emission is small compared with the night airglow.

Table 7-4. Estimated intensity of  $6300\text{\AA}$  emission excited by a 325 eV electron beam of unit ampere current at 300-km altitude.

Wavelength ( $\text{\AA}$ )	Production Rate of $O(^1D)$ ( $\text{cm}^{-3} \text{ sec}^{-1} \text{ amp}^{-1}$ )			Intensity Per Ampere (Rayleighs)		
	$n_e = 10^5$	$10^6$	$5 \times 10^6$	$n_e = 10^5$	$10^6$	$5 \times 10^6$
6300	$7.3^4$	$1.2^4$	$4.2^3$	$7.3^1$	$1.2^1$	4.2

### Conclusions

We conclude that the signal (from both permitted and forbidden transitions in  $O$ ) attainable in an electron beam experiment at 300-km altitude is too small, relative to the airglow background, to provide a usable means for measuring the neutral wind component normal to the magnetic field.

## REFERENCES

1. Tarr, P. W., D. H. Archer, and N. G. Utterback, Studies of Auroral Simulation, DNA 3297F, MRC-R-122, Mission Research Corporation, 11 April 1974.
2. Archer, D. H. and P. W. Tarr, Auroral Simulation Studies, DNA 3567T, HAES Report No. 6, MRC-R-152, Mission Research Corporation, 22 April 1975.
3. Tarr, P. W., ARCTIC Code Electron Deposition Theory with Application to Project EXCEDE, DNA 3636T, HAES Report No. 10, MRC-R-173, Mission Research Corporation, 18 June 1975.
4. Tarr, P. W., and D. H. Archer, Auroral Simulation Studies in Support of ICECAP and EXCEDE, DNA 3785F, HAES Report No. 24, MRC-R-211, Mission Research Corporation, 30 September 1975.
5. Romick, Gerald J., Report on the Geophysical Description and Available Data Associated with Rocket PF-SH-92, Scientific Report No. 7, Geophysical Institute, University of Alaska, January 1976.
6. Perreault, P. D., R. R. Vondrak, and T. M. Watt, ICECAP '75-Chatanika Radar Results, Topical Report, Contract DNA001-74-C-0167, SRI Project 3118, Stanford Research Institute, Menlo Park, Calif. (In Press).
7. Sears, Robert D., Lockheed Palo Alto Research Laboratory, Private Communication, May 1976.
8. Hegblom, E. R., Boston College, and James C. Ulwick, Air Force Geophysics Laboratory, Private Communication.
9. Sears, Robert D., Ionospheric Irregularities: HAES Program Support, DNA 3782F, Haes Report No. 29, Lockheed Palo Alto Research Laboratory, 30 September 1975.
10. Doyle, P. G., Air Force Geophysics Laboratory, Private Communication.

11. Burt, D. A., and C. S. Davis, Rocket Instrumentation for ICECAP 73A Auroral Measurements Program-Black Brant 18.205-1, HAES Report No. 3, AFCRL-TR-74-0195, Utah State University, February 1974.
12. Wheeler, Ned, Air Force Geophysics Laboratory, Private Communication.
13. Kumer, John B., Analysis of 4.3  $\mu\text{m}$  ICECAP Data, Haes Report No. 19, AFCRL-TR-74-0334, Lockheed Palo Alto Research Laboratory, July 1974.
14. Nadile, R., Air Force Geophysics Laboratory, Private Communication.
15. Peterson, L. R., et al., Electron Deposition in a Gaseous Mixture, Computer Physics Comm. 5, 239 (1973).
16. Takayanaqi, K., and Y. Itikawa, Elementary Processes Involving Electrons In the Ionosphere, Space Sci. Rev. 11, 380 (1970).
17. Walker, J. C. G., and M. H. Rees, Ionospheric Electron Densities and Temperatures in Aurora, Planet. Space Sci. 16, 459 (1968).
18. Zipf, E. C., W. L. Borst, and T. M. Donahue, J. Geophys. Res. 75, 6371 (1970).
19. Swider, W., and R. S. Narcisi, J. Geophys. Res. 79, 2849 (1974).
20. Narcisi, R. S., and W. Swider, J. Geophys. Res. 81, 4770 (1976).
21. Meira, L. G., J. Geophys. Res. 76, 202 (1971).
22. Strobel, D. F., J. Geophys. Res. 76, 2441 (1971).
23. Narcisi, R. S., Private Communication.
24. Strobel, D. F., et al., J. Geophys. Res. 81, 3745 (1976).
25. Kofsky, I. L., et al., Data Reduction and Auroral Characterizations for ICECAP II, HAES Report No. 27, DNA 3789F, Photometrics, Inc., 25 October 1975.
26. Mitchell, H., R & D Associates, Private Communication.
27. Tinsley, B. A., et al., J. Geophys. Res., 78, 1174 (1973).
28. Christensen, A. B., Private Communication with I. L. Kofsky.
29. Omholt, A., the Optical Aurora, Springer-Verlag (1971), p. 82.
30. Gattinger, R. L., and A. Vallance Jones, Can. J. Phys. 52, 2343 (1974).

31. Meyer, J. A., et al., *Astrophys. J.* 157, 1023 (1969).
32. Meyer, J. A., et al., *J. Chem. Phys.* 55, 2084 (1971).
33. Allen, C. W., *Astrophysical Quantities*, The Athlone Press (1973)
34. Becker, K. H., et al., *Chem Phys. Lett.* 15, 215 (1972).
35. Donahue, T. M., *J. Geophys. Res.* 79, 4337 (1974).

APPENDIX A  
 PARTITION OF ELECTRON ENERGY ( $\geq 1$  keV) IN ATMOSPHERIC GASES

PRELIMINARY

In the discussion of electron temperatures, given in Section 4 of this report, or in the calculation of the effects of X-ray or electron deposition, one needs a simple semi-quantitative method of partitioning the deposited energy. In this appendix we use the continuous slowing down approximation (Reference 3) to develop approximate relationships for the partition.

PARTITION FOR SMALL FRACTIONAL IONIZATION

The equation that determines the slowing down of an electron in a gaseous mixture of  $N_2$ ,  $O_2$ ,  $O$ ,  $N_2^+$ , ... is given by

$$\begin{aligned} \frac{dE}{ds} = & -[N_2]L_{N_2}(E) - [O_2]L_{O_2}(E) - [N]L_N(E) \\ & - [O]L_O(E) - [N_2^+]L_{N_2^+}(E) \dots \end{aligned} \quad (A-1)$$

where  $[N_2]$ ,  $[O_2]$ , ..., refers to the concentrations of  $N_2$ ,  $O_2$ , ..., and  $L$  refers to their respective loss functions (References 1, 3). The loss function is defined by the equation

$$L = \sum_j \sigma_j w_j + \text{ionization terms} \quad (A-2)$$

where  $\sigma_j(E)$  is the cross section for an electron of energy  $E$  to excite state  $j$  of the atom (or molecule) and lose an amount of energy  $w_j$  in the process,  $E$  is the mean energy of the electron, and  $s$  is the mean path length traveled.

It is an interesting fact that the above loss functions for keV electrons are related approximately by

$$L_{N_2} \approx L_{O_2} \approx 2L_N \approx 2L_O \approx L_{N_2^+} \approx \dots \equiv 2L \quad (A-3)$$

That is, the loss function depends, approximately, only on the number of atoms present in the gas. Thus, we can write Equation A-1 as

$$\frac{dE}{ds} \approx -AL(E) \quad (A-4)$$

where  $A$  is defined by the relation

$$A = 2[N_2] + 2[O_2] + [O] + [N] + \dots \quad (A-5)$$

For keV electrons,  $L$  is given by

$$L(E) \approx \frac{2.5 \times 10^{-18}}{E^{.75}} \text{ (keV cm}^2\text{)} \quad (A-6)$$

Now the probability that a single electron (unit flux) of energy  $E$ , traversing a distance  $ds$ , will excite the  $j^{\text{th}}$  state of  $N_2$  is given by

$$[N_2] \sigma_{[N_2]_j} ds \quad (A-7)$$

Therefore, the number of excited states formed by an electron, per unit distance, while it is slowing down is

$$\frac{dJ_{[N_2]_j}}{ds} = [N_2] \sigma_{[N_2]_j} \quad (A-8)$$

Integrating Equation A-8 over  $s$ , and making use of Equation A-4, we find

$$J_{[N_2]_j} = [N_2] \int_0^x \sigma_{[N_2]_j} ds = \frac{[N_2]}{A} \int_0^{E_0} \frac{\sigma_{[N_2]_j} dE}{L(E)} \quad (A-9)$$

Since  $L_{N_2} \approx 2L$ , Equation A-9 can be rewritten as

$$J_{[N_2]_j} = \frac{2[N_2]}{A} \left\{ \int_0^{E_0} \frac{\sigma_{[N_2]_j} dE}{L_{[N_2]}(E)} \right\} \quad (A-10)$$

where  $E_0$  is the initial electron energy and the term in brackets depends only on the results calculated (or measured) in a pure gas.

For keV electrons,

$$\int_0^{E_0} \frac{\sigma_{[N_2]_j} dE}{L_{[N_2]}(E)} \approx \epsilon_{[N_2]_j} E_0, \quad (A-11)$$

where  $\epsilon_{[N_2]_j}$  is a constant.

Equation A-10 can now be written as

$$J_{[N_2]_j} = f_{[N_2]} \epsilon_{[N_2]_j} E_0 \quad (A-12)$$

where

$$f_{[N_2]} \equiv 2[N_2]/A \quad (A-13)$$

The total amount of energy going into state  $[N_2]_j$  is  $J_{[N_2]_j}$ , and the fraction of the total energy,  $E_0$ , going into  $[N_2]_j$  is

$$P_{[N_2]_j} = \frac{J_{[N_2]_j}}{E_0} = f_{[N_2]} \epsilon_{[N_2]_j} w_{[N_2]_j} \quad (A-14)$$

Clearly,  $\epsilon_{[N_2]_j}^{w_{[N_2]_j}}$  is the partition one would calculate for a pure  $N_2$  gas. These results can be applied to any gas in the mixture. Equation A-14 tells us that we need only combine the partition calculated in pure gases linearly, weighting each by the fractional number of atoms present.

The above derivation was for the primary electrons only, but when secondaries and higher order effects are included, detailed calculations show that Equations A-10 through A-14 are still approximately correct although the constants  $\epsilon$  are then redefined. The fractional amount of energy going into each excited state is approximately independent of the initial electron energy. In particular, this holds for states of ionization. For example, it is well known that the number of ion-pairs formed per eV deposited in "normal air" is a constant over a wide range of incident electron energies. In the present notation this can be written as

$$\text{ion-pairs/eV} \approx \sum_{ij} f_i \epsilon_{ij} \quad (\text{A-15})$$

where  $i$  denotes the gas and  $j$  denotes a state of ionization.

In Tables A-1 to A-4 are listed the constants  $\epsilon$  for  $N_2$ ,  $O_2$ ,  $N$ , and  $O$  gases. These results include all orders of secondary electrons. The actual solution is an integral equation which can be solved exactly (Reference 15). Since the above derivation is approximate rather than exact, we have weighted the results so that  $N_2$  and  $O_2$  reproduce the results of an 80 percent  $N_2$  and 20 percent  $O_2$  gas mixture while  $O$  is weighted to a 50 percent  $N_2$  and 50 percent  $O$  gaseous mixture.

These results can now be used to calculate ionization, excitation and partition of energy in a mixture of gases following X-ray or electron deposition. The effect of the variation of atmospheric constituents during deposition can also be taken into account in a straightforward manner. For

Table A-1. Partition in a pure N<sub>2</sub> gas.

i	State	$\epsilon_{[N_2]}$	Mean Excitation Energy (eV)*	Energy Partition (P <sub>i</sub> )
1	N <sub>2</sub> <sup>+</sup>	.0252	16.98	.427
2	N <sup>+</sup> ( <sup>3</sup> P)	.002	19.42	.039
3	N <sup>+</sup> ( <sup>1</sup> D)	.0008	21.32	.017
4	N <sup>+</sup> ( <sup>1</sup> S)	.0002	23.52	.005
5	N( <sup>4</sup> S)	.0078	4.88	.038
6	N( <sup>2</sup> D)	.007	7.26	.051
7	N( <sup>2</sup> P)	.0018	8.46	.015
8	N <sub>2</sub> (v)direct	.223	.3	.067
9	N <sub>2</sub> (v)cascade	.007	.3	.002
	Ion Kinetic Energy			.008
	Neutral Kinetic Energy			.023
	Energy into Electron Gas and N <sub>2</sub> Rotational Excitation			.031
	Energy into Radiation and Metastable States of N <sub>2</sub>			.277

\* The mean energy is not necessarily the energy of the lowest lying state since several states may have been combined to form the above table. For atomic products, one half the dissociation energy has been assigned to the mean excitation energy.

Table A-2. Partition in a pure O<sub>2</sub> gas.

i	State	$\epsilon_{[O_2]}$	Mean Excitation Energy (eV)	Energy Partition (P <sub>i</sub> )
10	O <sub>2</sub> <sup>+</sup>	.0203	16.75	.335
11	O <sup>+</sup> ( <sup>4</sup> S)	.007	16.15	.113
12	O <sup>+</sup> ( <sup>2</sup> D)	.004	19.45	.078
13	O( <sup>3</sup> P)	.0387	2.54	.098
14	O( <sup>1</sup> D)	.0127	4.5	.057
15	O <sub>2</sub> (v)	.67	.25	.168
16	O <sub>2</sub> ( <sup>1</sup> Δ)			.040
	Ion Kinetic Energy			.002
	Neutral Kinetic Energy			.031
	Energy into Electron Gas and O <sub>2</sub> Rotational Excitation			.005
	Energy into Radiation and Metastable States of O <sub>2</sub>			.073

Table A-3. Partition in a pure O gas.

i	State	$\epsilon_{[O]}$	Mean Excitation Energy (eV)	Energy Partition ( $P_i$ )
17	O( <sup>1</sup> D)	.110	1.96	.217
18	O( <sup>1</sup> S)	.005	4.98	.021
19	O <sup>+</sup> ( <sup>4</sup> S)	.016	13.61	.218
20	O <sup>+</sup> ( <sup>2</sup> D)	.014	16.9	.237
21	O <sup>+</sup> ( <sup>2</sup> P)	.007	18.5	.130
	Energy Lost to Electron Gas and Fine Structure of O( <sup>3</sup> P)			.058
	Energy into Radiation			.119

Table A-4. Partition in a pure N gas.

i	State	$\epsilon_{[N]}$	Mean Excitation Energy (eV)	Energy Partition ( $P_i$ )
22	N( <sup>2</sup> D)	.082	2.38	.195
23	N( <sup>2</sup> P)	.022	3.58	.079
24	N <sup>+</sup> ( <sup>3</sup> P)	.018	14.5	.261
25	N <sup>+</sup> ( <sup>1</sup> D)	.016	16.4	.262
26	N <sup>+</sup> ( <sup>1</sup> S)	.007	18.6	.130
	Energy Lost to Electron Gas			.008
	Energy into Radiation			.065

example, if  $\mathcal{E}$  represents the total amount of energy deposited, the rate at which  $[N_2]$  is destroyed is

$$\frac{d[N_2]}{dt} = - \frac{2[N_2]}{A} \left\{ \epsilon_1 + \frac{1}{2} \sum_{i=2}^7 \epsilon_i \right\} \frac{d\mathcal{E}}{dt} \quad , \quad (\text{A-16})$$

where the values of  $\epsilon_i$  are given in Table A-1.

In terms of the variable  $U = \mathcal{E}/A$ , Equation A-16 can now be written as

$$\frac{d[N_2]}{dU} = - [N_2] R_1 \quad . \quad (\text{A-17})$$

with solution

$$[N_2] = [N_2]_0 e^{-R_1 U} \quad , \quad (\text{A-18})$$

where

$$R_1 = 2\epsilon_1 + \epsilon_2 + \epsilon_3 + \epsilon_4 + \epsilon_5 + \epsilon_6 + \epsilon_7$$

and  $[N_2]_0$  is the initial concentration of  $N_2$  at the start of the deposition. Concentrations of other states can be calculated using a similar procedure.

#### PARTITION FOR LARGER FRACTIONAL IONIZATION

Results such as A-18 are valid provided the fractional ionization remains small. If it does not, then we must add an additional term to the right side of Equation A-4, rewriting it as

$$\frac{dE}{ds} = - AL - n_e L_e \quad . \quad (\text{A-19})$$

Here,  $n_e$  is the electron density and  $L_e$  is the electron loss function given, for keV electrons, by (Reference 15)

$$L_e \approx 3.4 \times 10^{-15} / E \text{ keV cm}^2 \quad (\text{A-20})$$

In general, the partition of energy now becomes a very complex function. Factoring A out of the right hand side of Equation A-19, we get

$$\frac{dE}{ds} = -A(L + f_e L_e) \quad (\text{A-21})$$

where

$$f_e = n_e / A \quad (\text{A-22})$$

The fraction of the energy,  $E_o$ , going into the electron gas is given by

$$P_e = \frac{1}{E_o} \int_0^{E_o} \frac{n_e L_e}{AL + n_e L_e} dE + \frac{1}{E_o} \int_0^{\frac{1}{2}(E_o - I)} \frac{n(E, T) n_e L_e(T)}{AL(T) + n_e L_e(T)} dT \quad (\text{A-23})$$

where  $n(E, T)$  is the number of secondary electrons of energy  $T$  produced by a primary of energy  $E$ , and  $I$  is the ionization potential (see Reference 15).

We see that as long as  $f_e L_e$  is small compared to  $L$ , the previous results hold. When  $f_e L_e$  is large compared to  $L$ , then all of the energy will go into the electron gas. The region in between is quite complex particularly since the partition depends on an integral over energy, and  $L$  and  $L_e$  have different energy dependencies. Thus, primary and secondary electrons behave differently as a function of fractional ionization,  $f_e$ . To first order, we can consider four separate regions depending on whether it is primary or secondary electrons that are mainly involved in heating the electron gas.

We first note that typical energies of secondary electrons are  $\sim 10$  eV while primary electrons are 100 eV to 10 keV or more. Thus,  $L_e$  for a secondary electron is several orders of magnitude larger than  $L_e$  for a primary. For "small" fractional ionization ( $f_e < 10^{-9}$ ) the principle method of heating the ambient electron gas is by secondary electrons and essentially no heating is done by the primaries. The heating rate is so small that it can be considered as essentially a perturbation on the previous results. Thus, in Region 1 the first term on the right hand side of Equation A-23 is zero, and the partition of energy into the electron gas becomes

$$P_e \approx \frac{1}{E_0} \int_0^{\frac{1}{2}(E_0-I)} \frac{n(E,T)n_e L_e(T)}{AL(T)} dT = f_e \delta_1 \quad (\text{A-24})$$

where  $\delta_1$  is a constant applicable to Region 1.

As the fractional ionization increases, however, there comes a point where  $f_e L_e > L$  for secondaries but  $f_e L_e \ll L$  for primaries. That is, we reach a point of saturation where all of the secondary electron energy, but none of the primary energy, goes into heating the ambient electron gas. In this region the partition of energy into the electron gas becomes simply a constant, independent of the fractional ionization. Thus, in Region 2,

$$P_e \approx \delta_2 \quad (\text{A-25})$$

Region 3 is where  $f_e L_e < L$  for primaries, but the primaries still contribute to heating the ambient electron gas. The first term of Equation A-23 can then be approximated as

$$\frac{1}{E_0} \int_0^{E_0} \frac{n_e L_e}{AL} dE \approx f_e \delta_3 \quad (\text{A-26})$$

The partition then becomes, approximately,

$$P_e \approx \delta_2 + f_e \delta_3 (1 - \delta_2) \quad (\text{A-27})$$

where the term  $f_e \delta_3 (1 - \delta_2)$  comes from the reduced amount of energy going into secondary electrons.

Finally, Region 4 is where  $f_e L_e \gg L$  for all energies and  $P_e \approx 1$ .

The foregoing behavior is illustrated schematically in Figure A-1. We see that in Regions 1 and 3,  $P_e$  varies linearly with  $f_e$  while in Regions 2 and 4 it is constant.

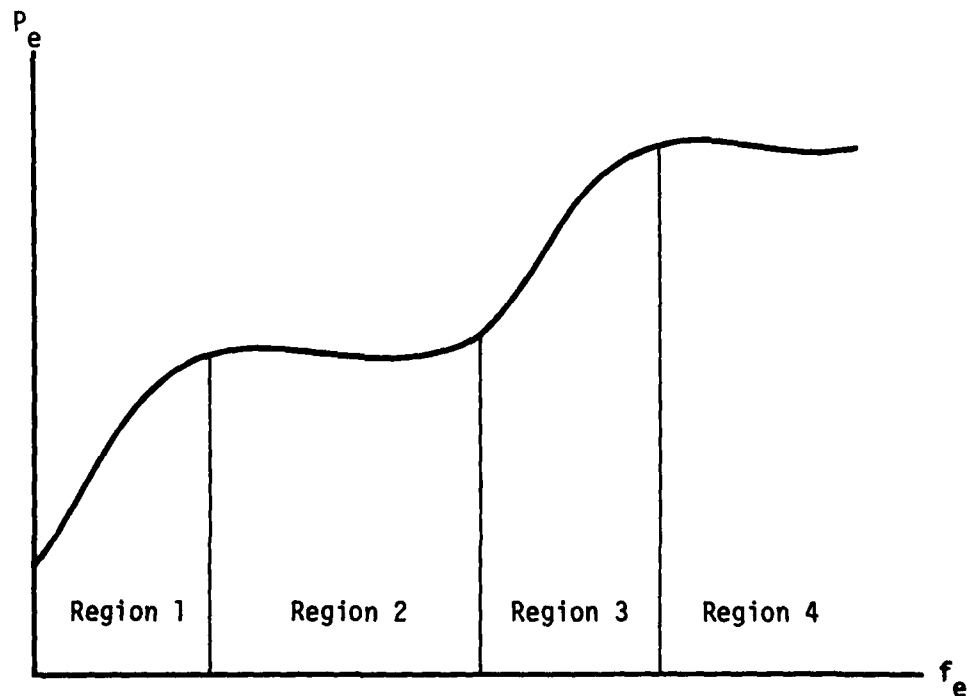


Figure A-1. Schematic illustration of the dependence of  $P_e$  on  $f_e$ .

Detailed runs of the ARCTIC code (References 1, 3) tend to confirm this analysis.\* We have done a parametric study over a wide range of energies ( $1 < E_0 < 15$  keV) and over compositions corresponding to a variety of atmospheric mixes between 60 and 200-km altitude.

Figure A-2 presents our results for one energy ( $E_0 = 4$  keV) at two compositions corresponding to altitudes of 100 and 184 km. We see that the results are quite independent of the incident electron energy. Regions 2 and 3, however, tend to overlap, giving rise to an intermediate behavior. The partition for fractional ionizations  $f_e > 10^{-6}$  varies approximately as  $f_e^{.25}$ . As expected, it is nearly independent of atmospheric composition. In Region 1 ( $f_e < 10^{-9}$ ), the variation of  $P_e$  with  $f_e$  is indeed seen to be linear, but the partition is composition dependent. This is not surprising in view of the low energies of the secondaries ( $\sim 10$  eV).

We have curve fit these results to better than 15 percent over the range  $0 \leq f_e \leq .1$  and for energies from  $1 \leq E_0 \leq 15$  keV. The result is

$$P_e = \frac{a f_e}{1 + \gamma_1 f_e} + \frac{b f_e}{1 + \gamma_2 f_e^{.77}} \quad (\text{A-28})$$

where

$$a = 5.21 \times 10^5 + 2.939 \times 10^6 M$$

$$\gamma_1 = 2.26 \times 10^6 + 4.37 \times 10^8 M + 4.62 \times 10^8 M^2$$

---

\* The loss function of Reference 1 has been modified below 2.1 eV by  $L = \text{MAX}[L_{01d}, f_{N_2} * \text{MAX}[1.8 \times 10^{-4}, 10^{-4} \text{EXP}(2.6 * E)]] + f_{O_2} \times 1.8 \times 10^{-4} + f_O \times 3.5 \times 10^{-3}$  to account for rotational excitation of  $N_2$ ,  $O_2$  and fine structure excitation of O (Reference 16).

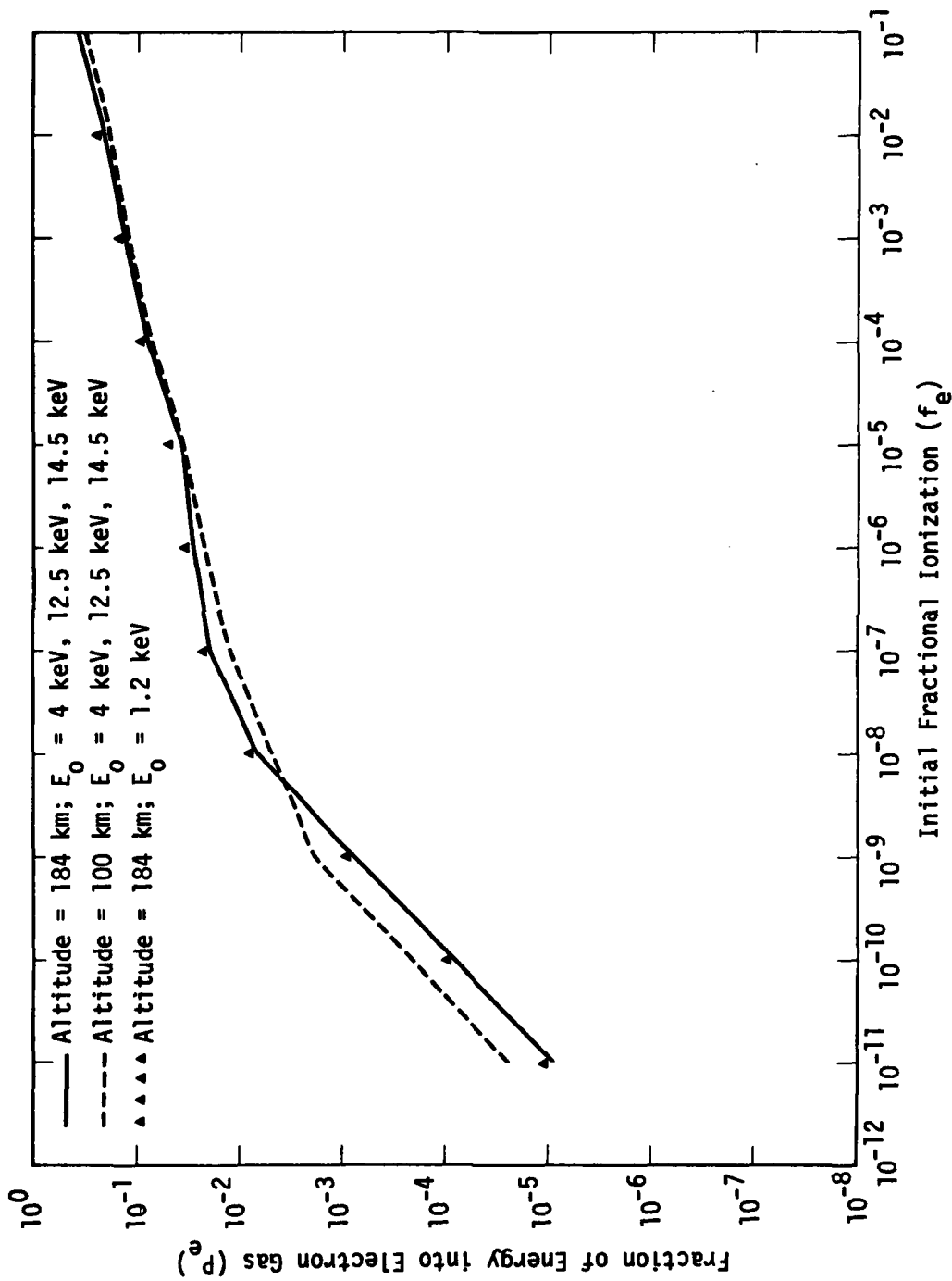


Figure A-2. Calculated fractional energy deposited in electron gas as function of initial fractional ionization.

$$b = 9 \times 10^4$$

$$\gamma_2 = 1.75 \times 10^5$$

$$M = [\text{Molecules}] / ([\text{Molecules}] + 12 \times [\text{ATOMS}])$$

To first order, the complete partition of energy into all modes is given by Equation A-28 (for the ambient electron gas) and by the results of Tables A-1 through A-4 reduced by a factor  $(1 - P_e)$ .

The modifications presented above will probably not affect calculations below altitudes of 100 km. However, above 200 km, where the fractional ionization regularly exceeds  $10^{-6}$ , the changes can be dramatic. In particular, use of Equation A-24, rather than Equation A-28 at these altitudes (the assumption usually made), will produce erroneous results.

APPENDIX B  
PARTITION OF ELECTRON ENERGY ( $\lesssim 25$  eV) IN ATMOSPHERIC GASES

The partition of low energy electrons ( $< 25$  eV) among various states is often needed for chemistry or IR calculations. These low energy electrons can arise from UV deposition or from deexcitation of excited atomic and molecular states. We have performed a parametric study, using the ARCTIC code, of this partition as functions of electron energy and fractional ionization. The results are presented here.

Figures B-1 through B-4 show, for deposition in  $N_2$ ,  $O_2$ , N, and O, respectively, the fraction of the electron's energy deposited in the thermal electron gas + rotational states + fine structure states of  $O(^3P)$  as functions of the initial fractional ionization,  $f_e$ , (see Equation A-22). We make the assumption that initially all of this energy is deposited in the final (after deposition) thermal electron gas. This is because the energy going into rotation or into fine structure excitation comes about only after most other excitations have occurred, at which time the electron has lost most of its energy. The cross sections for these processes are very flat at low energies so that subsequent cooling of the electron gas by rotational or fine structure excitation will be approximately correct.

Over the energy range considered (0-24 eV) the form of all the curves shown in Figures B-1 through B-4 can be represented approximately by

$$P_e = (A/E)^\alpha \quad (B-1)$$

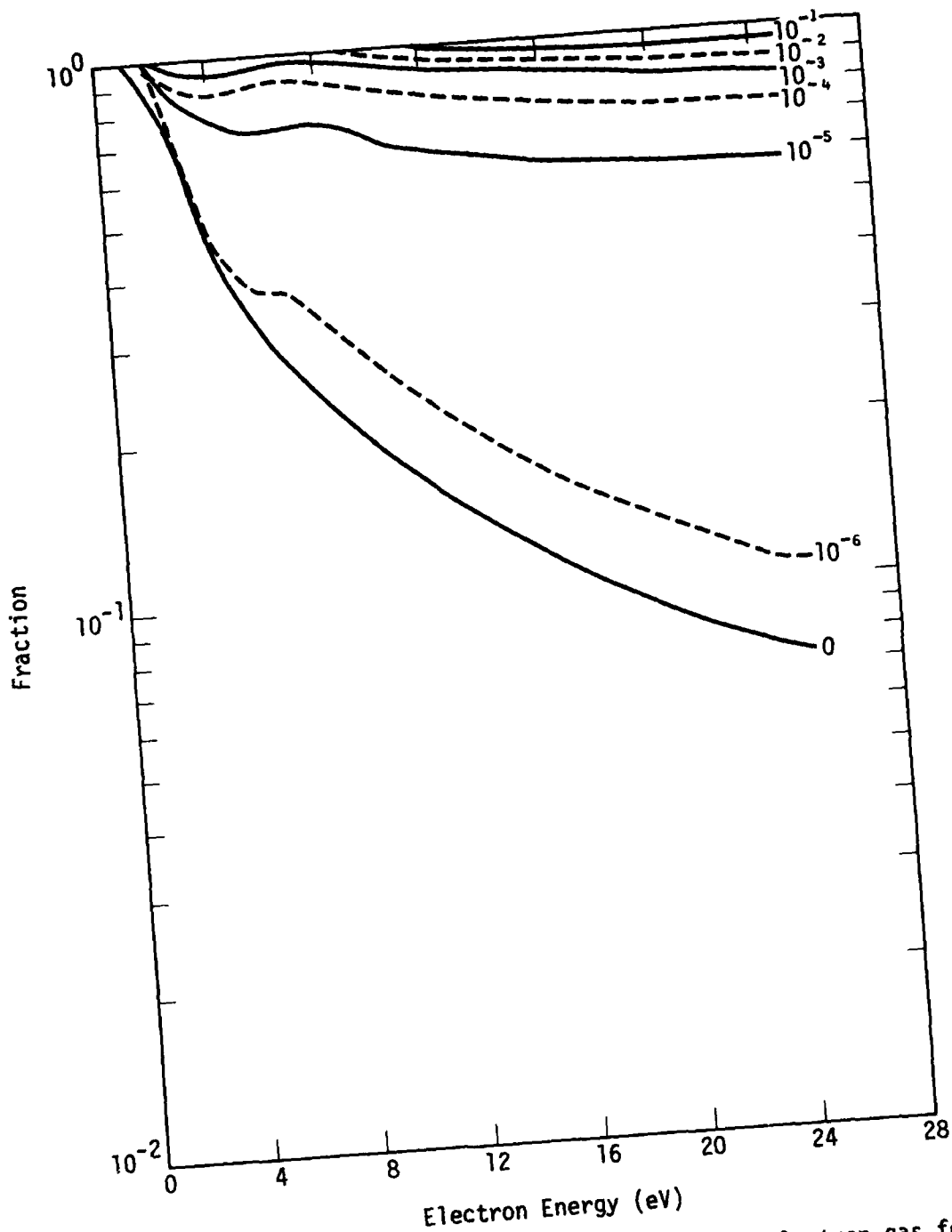


Figure B-1. Fraction of electron energy deposited in electron gas for parametric values of the fractional ionization in pure N<sub>2</sub>.

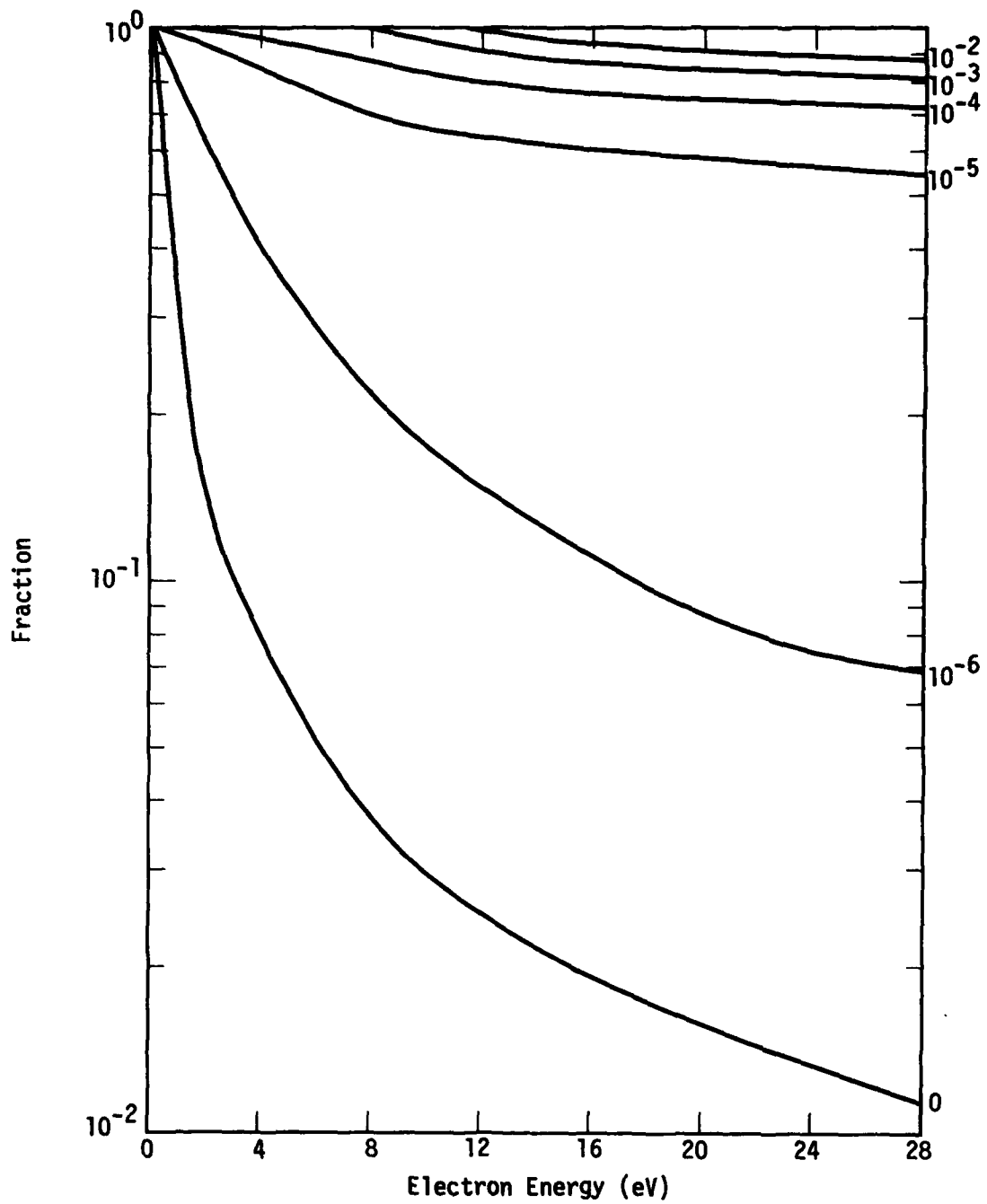


Figure B-2. Fraction of electron energy deposited in electron gas for parametric values of the fractional ionization in pure O<sub>2</sub>.

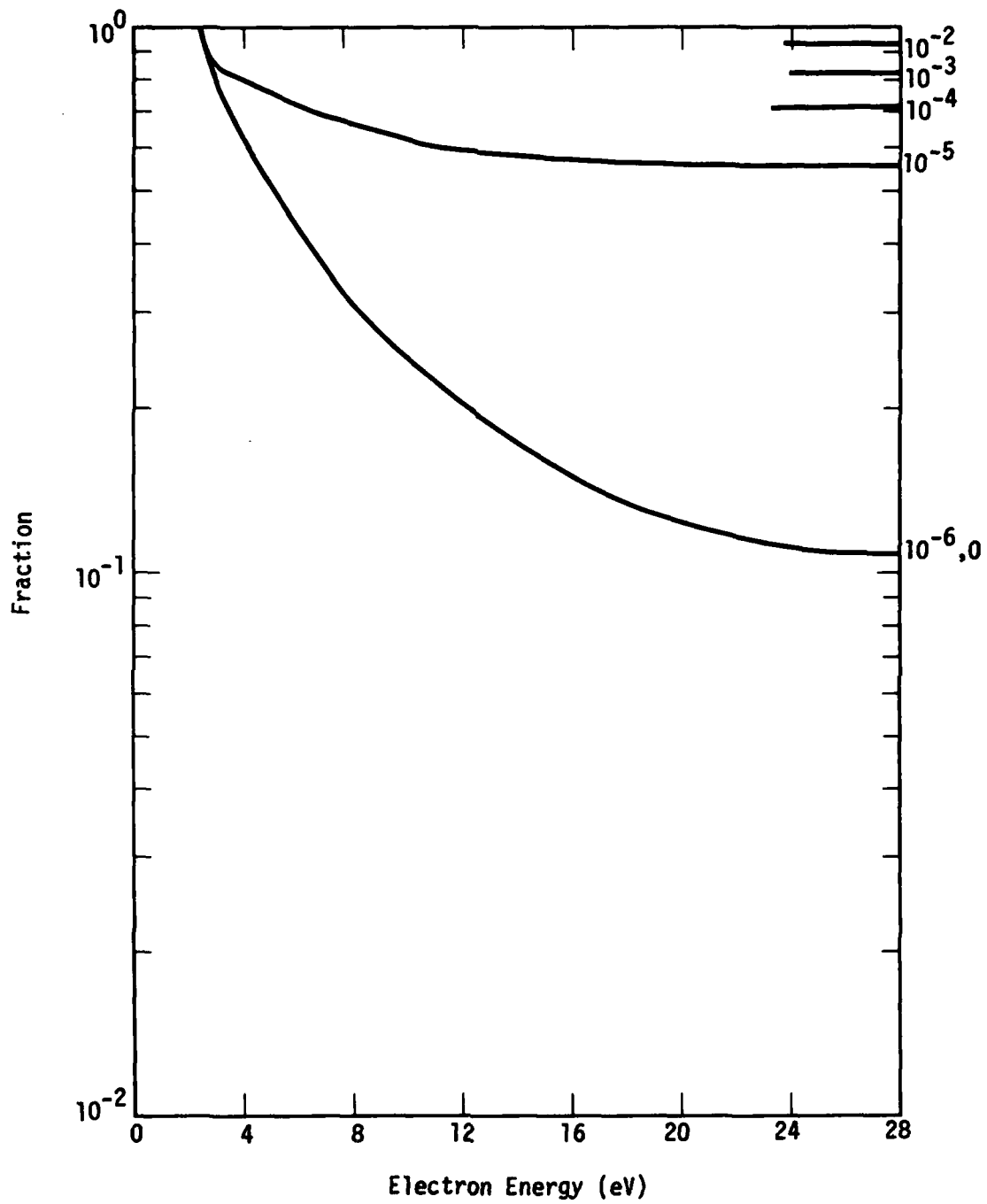


Figure B-3. Fraction of electron energy deposited in electron gas for parametric values of the fractional ionization in pure N.

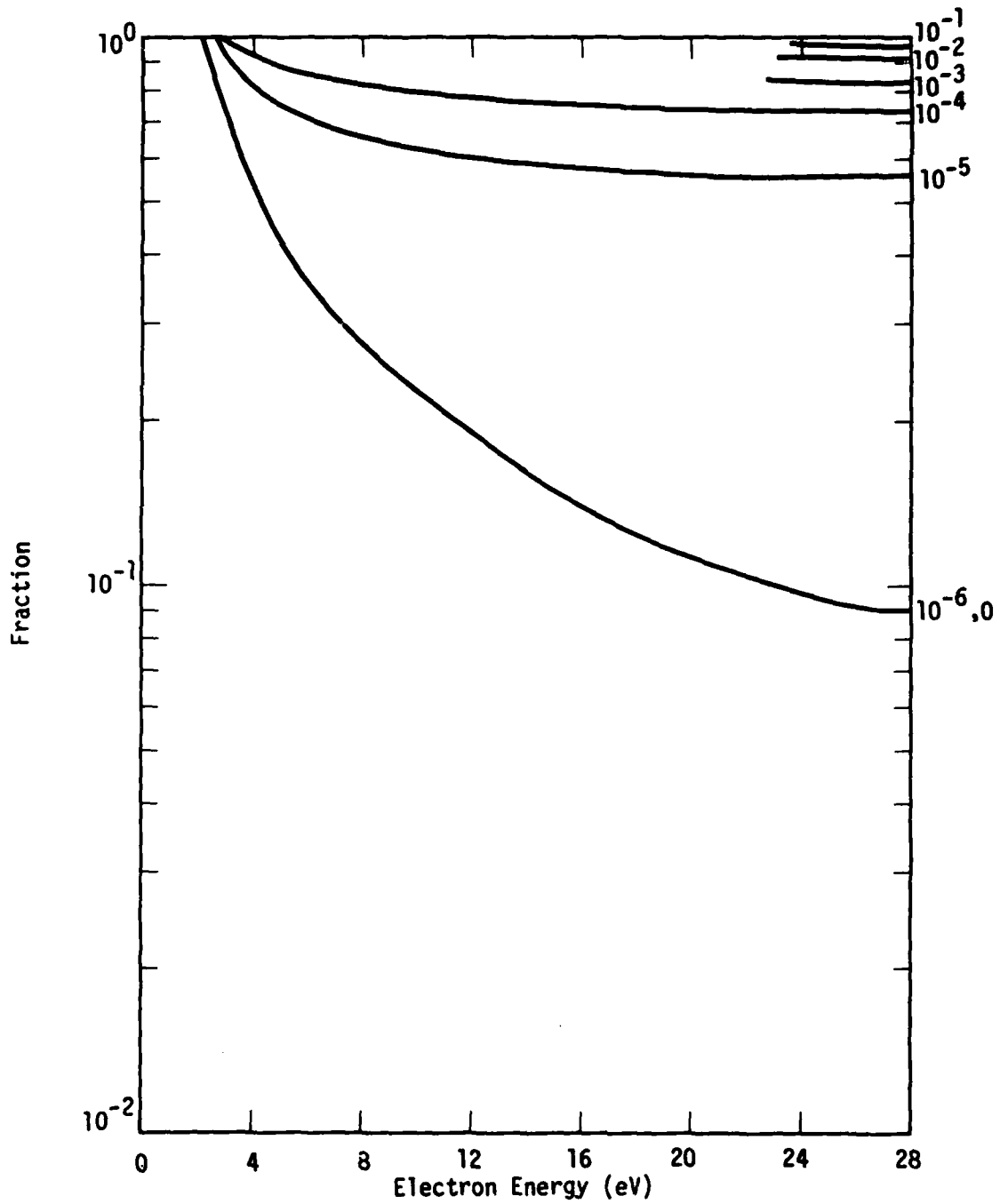


Figure B-4. Fraction of electron energy deposited in electron gas for parametric values of the fractional ionization in pure O.

where  $P_e$  is the fraction of the hot electron's energy going into the electron gas,  $E$  is the initial energy of the hot electron, and  $A$  and  $\alpha$  are parameters that depend on the fractional ionization. These parameters are given approximately by

$$\alpha \approx \text{MAX}[0.14, \text{MIN}(1, 0.96 - 8 \times 10^5 f_e)] \quad (\text{B-2})$$

and

$$A \approx 24^\alpha (U + \text{EXP}[\log(1-U) (14.5/(14.5 + \log f_e))^{1.37}]) \quad (\text{B-3})$$

where

$$U = \text{MAX}[\cdot 075, 8.616 \times 10^{-5} T_e/E] \quad .$$

In addition, we have calculated the energy going into other states. Figures B-5 and B-6 show, respectively, the fractions of energy going into vibrational states of  $N_2$  and  $O_2$  for fractional ionizations less than  $10^{-6}$ . We have approximated these curves by the functions

$$P_{N_2}(v) = \begin{cases} \frac{5.5}{E} (1 - 2/E) & E > 2 \\ 0 & E \leq 2 \end{cases} \quad (\text{B-4})$$

and

$$P_{O_2}(v) = \begin{cases} \frac{1.67}{E} (1 - 1/E) & E > 1 \\ 0 & E \leq 1 \end{cases} \quad (\text{B-5})$$

These approximations are plotted in Figures B-5 and B-6.

In addition, we have calculated the number of atomic nuclei formed per eV deposited, as was done in Appendix A. These results, shown in Figures B-7 through B-10, have been approximated analytically. The results are shown in Table B-1.

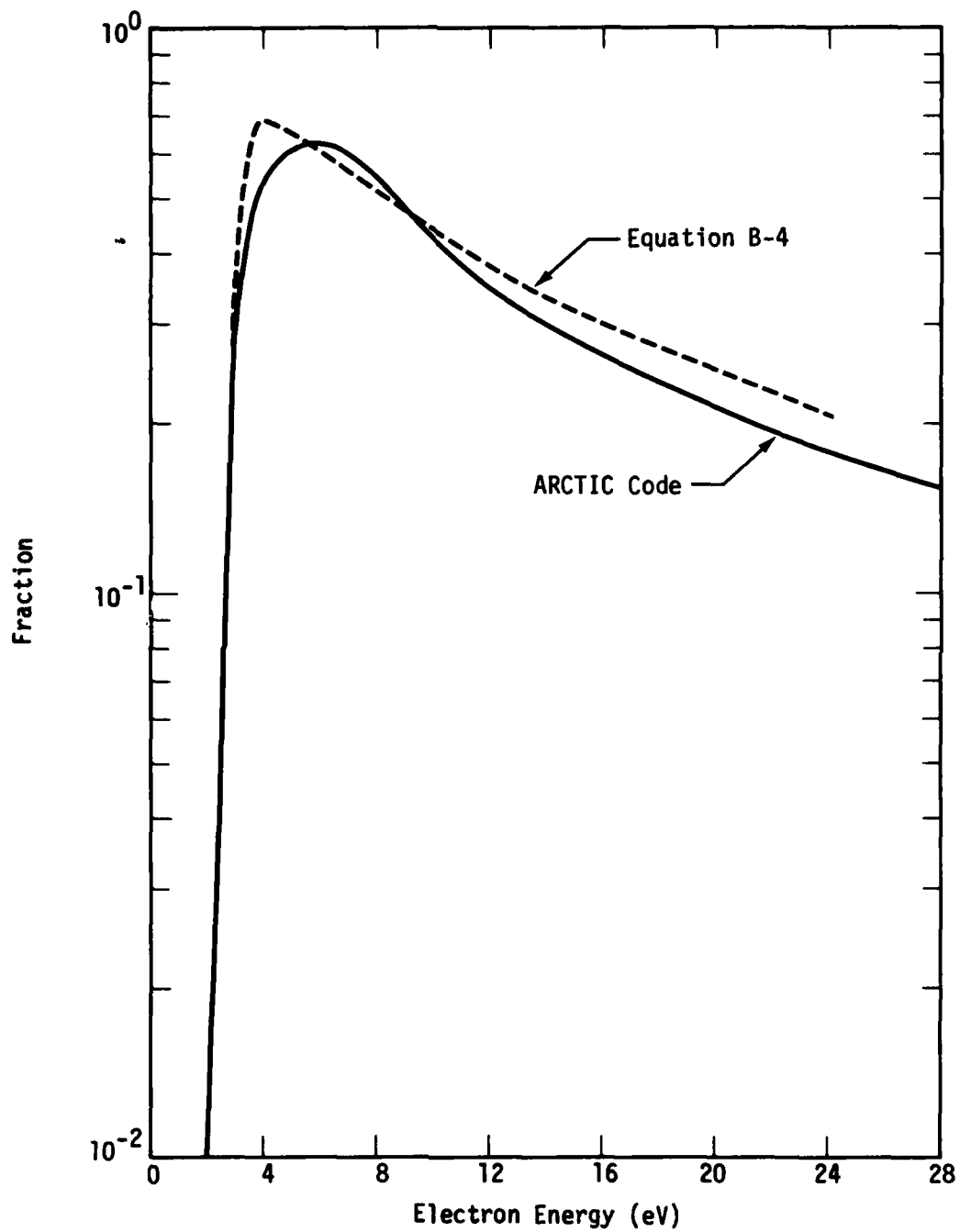


Figure B-5. Fraction of electron energy deposited in vibrational excitation of  $N_2$  for zero fractional ionization.

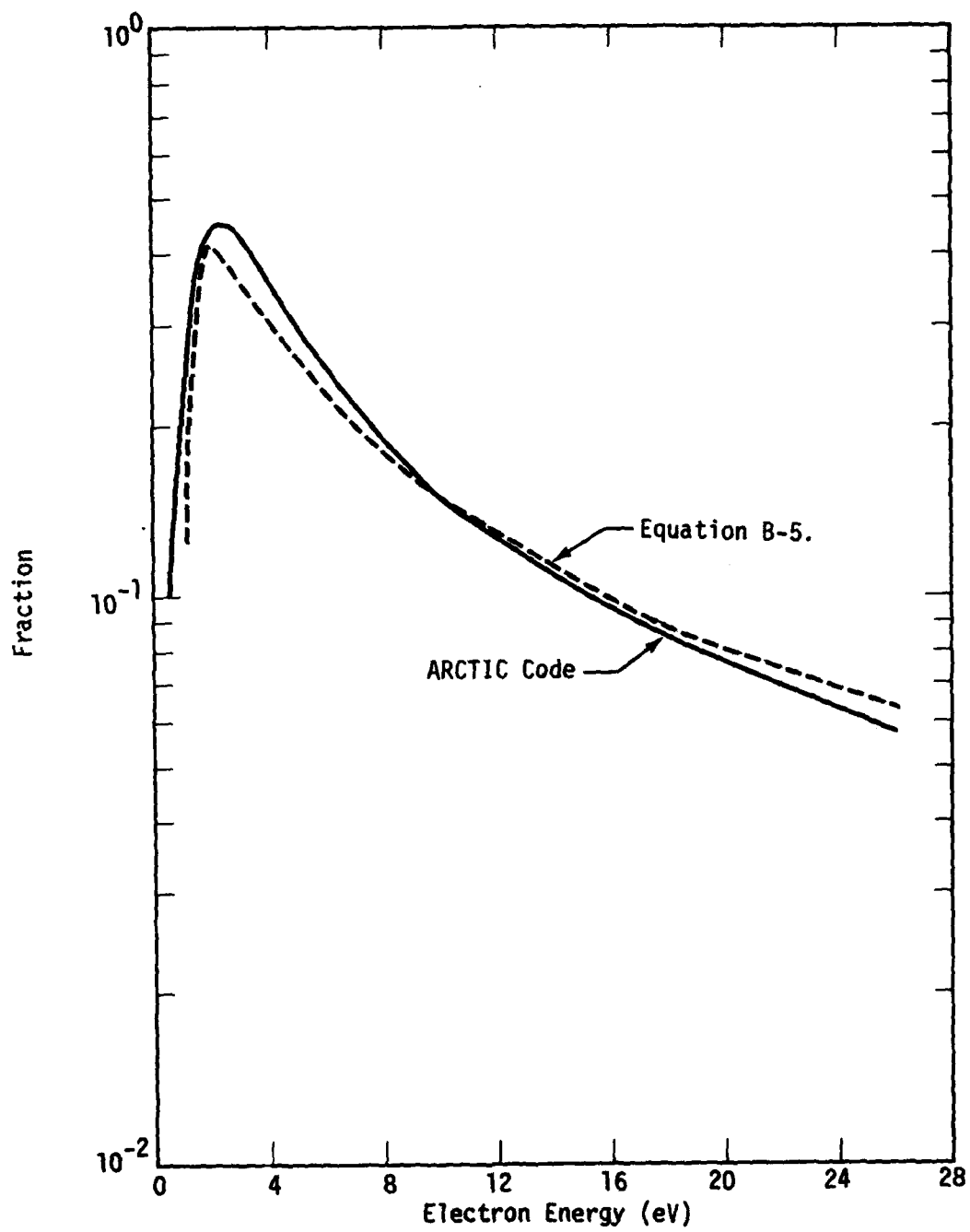


Figure B-6. Fraction of electron energy deposited in vibrational excitation of  $O_2$  for zero fractional ionization.

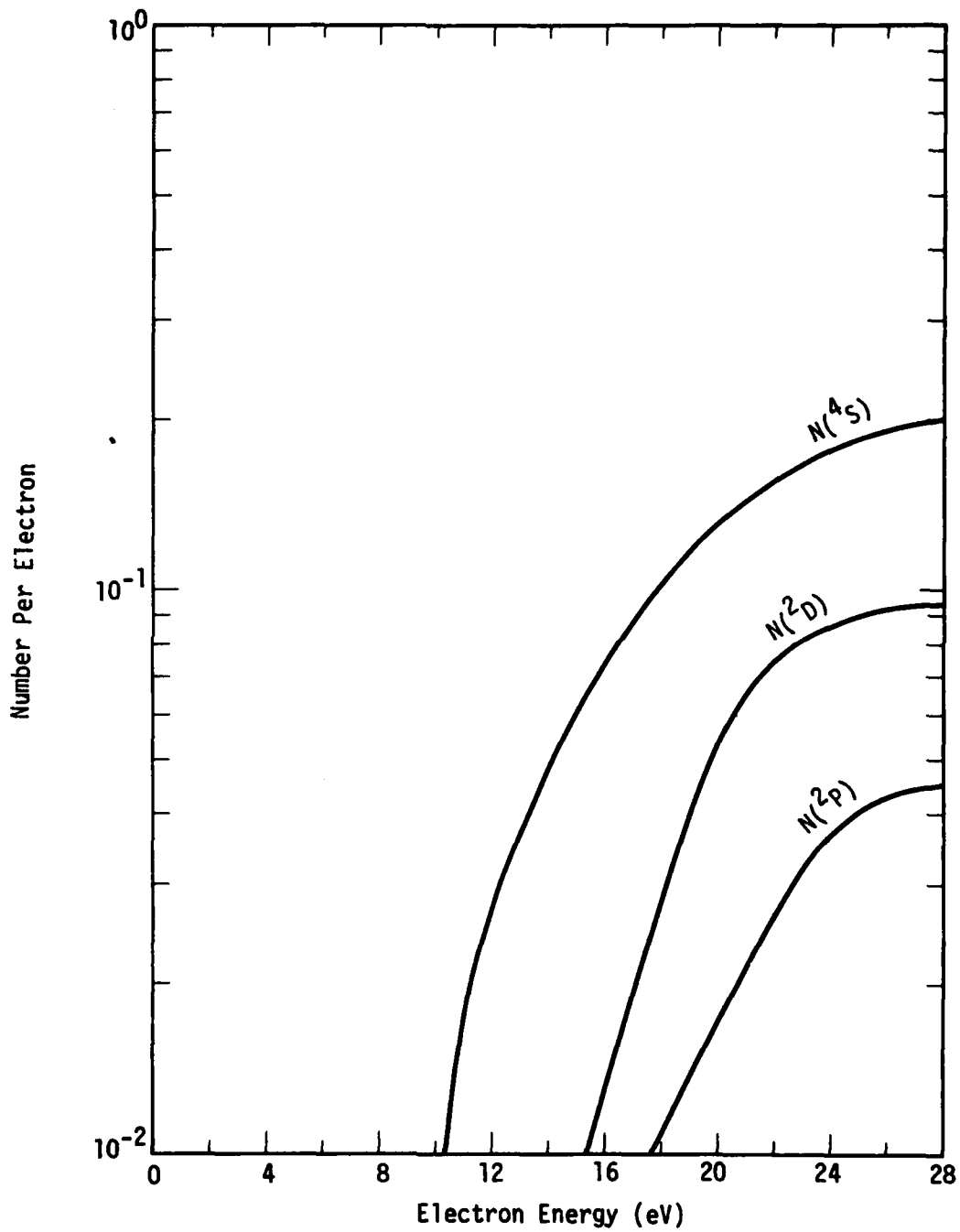


Figure B-7. Number of nitrogen atoms formed per electron deposited in  $N_2$  gas.

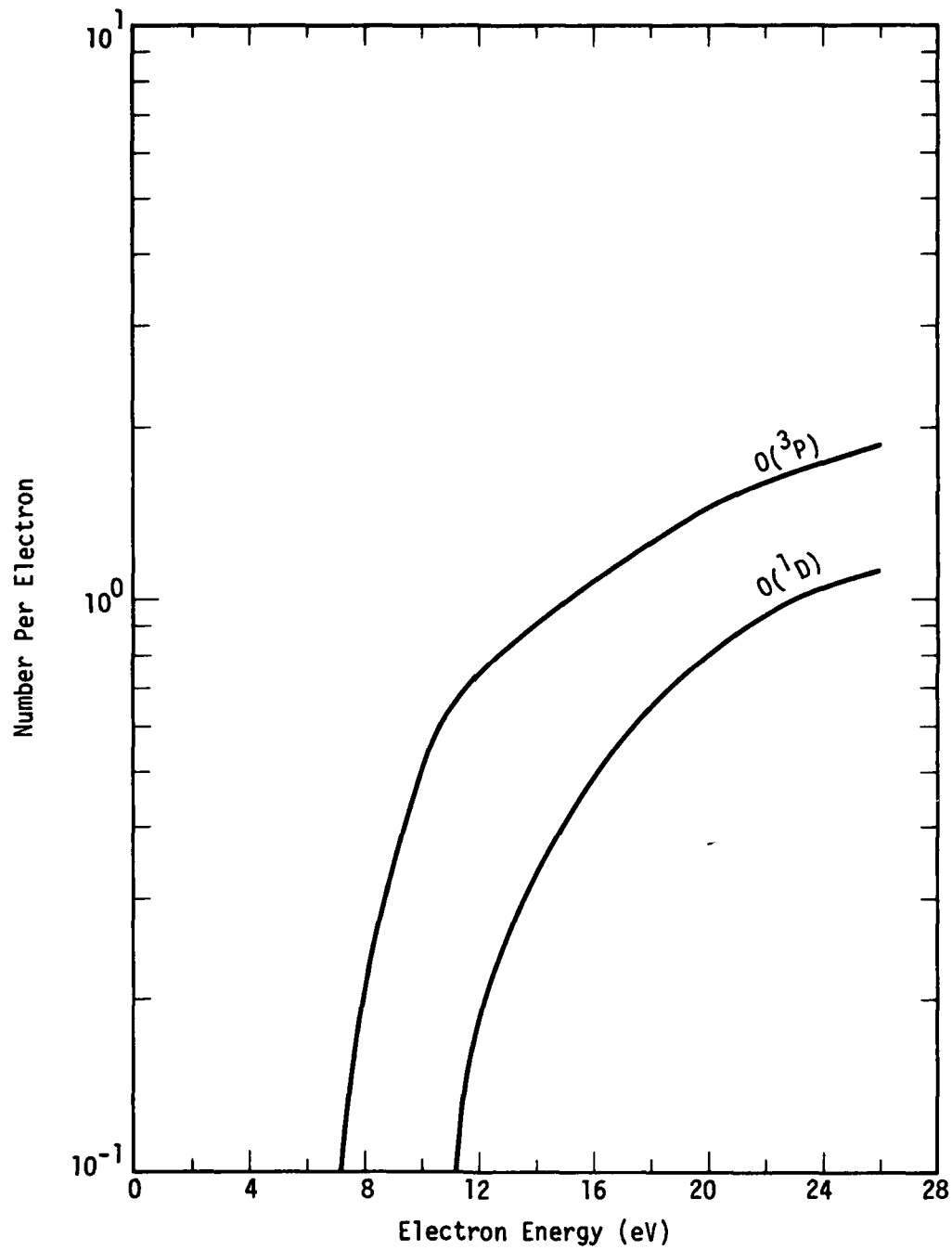


Figure B-8. Number of oxygen atoms formed per electron deposited in  $O_2$  gas.

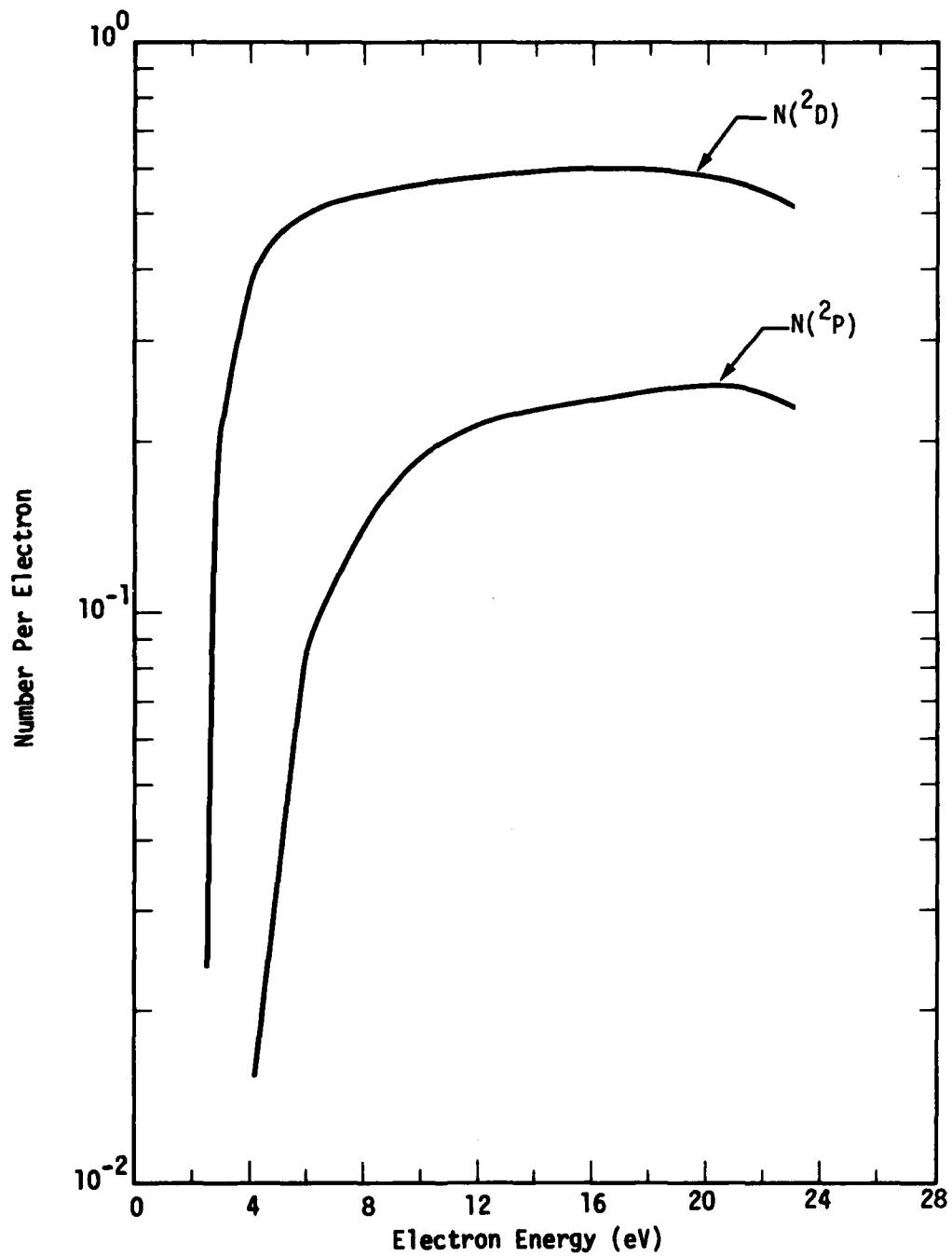


Figure B-9. Number of  $N(2D)$  and  $N(2P)$  atoms formed per electron deposited in N gas.

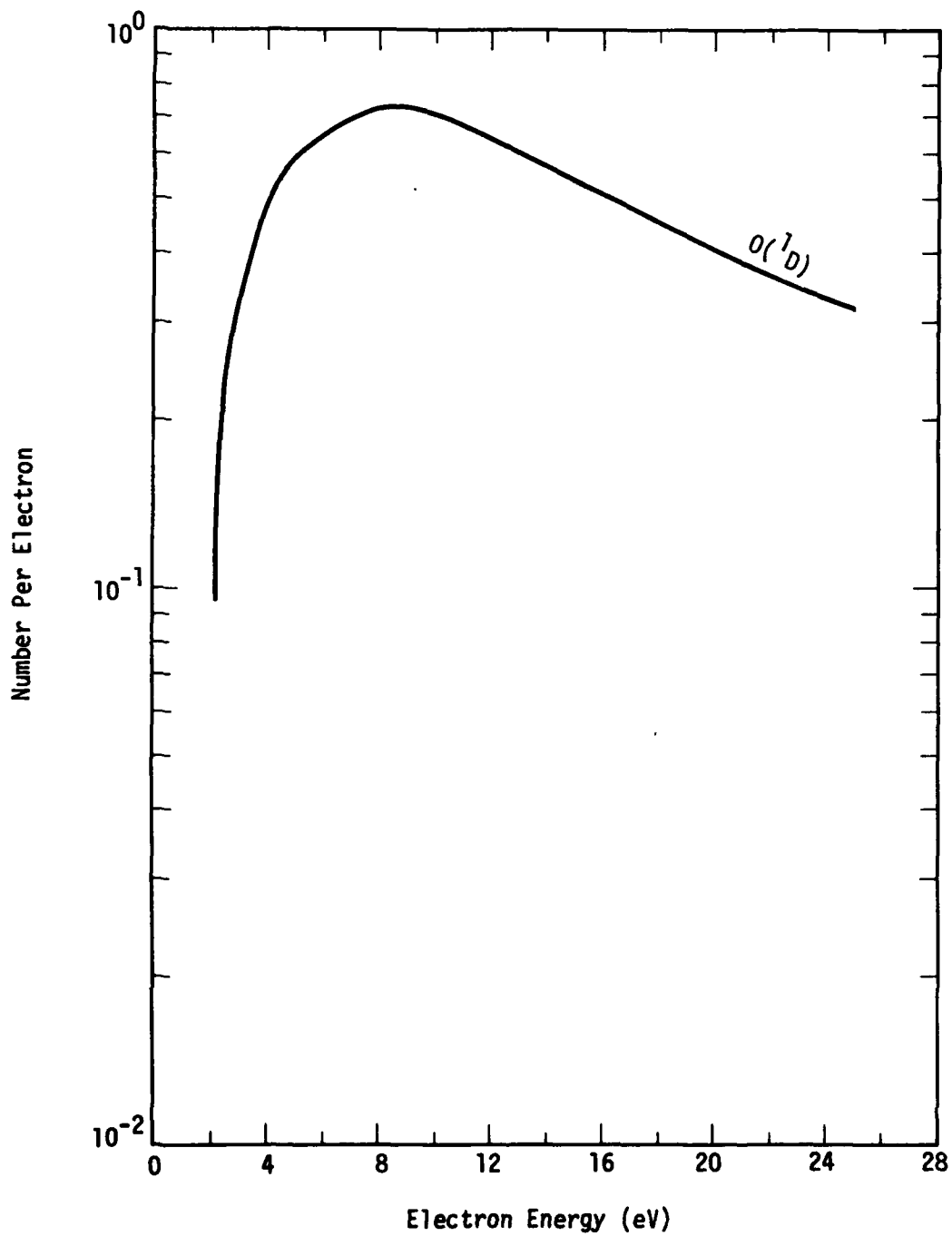


Figure B-10. Number of O(<sup>1</sup>D) atoms formed per electron deposited in O gas.

Table B-1. Species formed in low energy electron deposition.

Gas	Atomic Product Formed	Number Created Per eV Deposited
N <sub>2</sub>	N( <sup>4</sup> S)	0.39(1-10/E) <sup>1.5</sup> ; 10 ≤ E < 24 eV
	N( <sup>2</sup> D)	0.38(1-14/E) <sup>1.7</sup> ; 14 ≤ E < 24 eV
	N( <sup>2</sup> P)	0.17(1-14/E) <sup>1.7</sup> ; 14 ≤ E < 24 eV
O <sub>2</sub>	O( <sup>3</sup> P)	0.09(E-5.4) ; 5.4 ≤ E < 24 eV
	O( <sup>1</sup> D)	0.07(E-9.5) ; 9.5 ≤ E < 24 eV
N( <sup>4</sup> S)	N( <sup>2</sup> D)	0.6 ; 4 ≤ E < 24 eV
	N( <sup>2</sup> P)	0.22 ; 6 ≤ E < 24 eV
O( <sup>3</sup> P)	O( <sup>1</sup> D)	9.8E <sup>-1</sup> (1-1.96E <sup>-1</sup> ) <sup>2</sup> ; 1.96 ≤ E < 24 eV

For mixtures of gases, we have assumed linear superposition using the weighting factors of Appendix A (Equation A-12). In addition, when the fractional ionization exceeds 10<sup>-6</sup>, the fractions shown in Figures B-5 through B-10 must be reduced to allow for the additional energy going into ionization. For this purpose, we have used a reduction factor  $g_e$ , where

$$g_e = (1-f_e)/(1-U) \quad . \quad (B-6)$$

Thus, the partition of energy into N<sub>2</sub> and O<sub>2</sub> vibration can now be written as

$$P_{N_2}(v) = g_e f_{N_2} \frac{5.5}{E} (1-2/E) ; \quad E > 2 \text{ eV} \quad (B-7)$$

and

$$P_{O_2}(v) = g_e f_{O_2} \frac{1.67}{E} (1-1/E) ; \quad E > 1 \text{ eV} \quad (B-8)$$

From Figures B-1 through B-10 we see that our formulas are approximate rather than exact. Therefore, it may occur that energy is not strictly conserved. We have corrected for this by multiplying the results by a normalization factor, R, defined by

$$R = E/(\text{sum of all energy lost}) \quad . \quad (\text{B-9})$$

APPENDIX C  
ON OPTICAL MEASUREMENT OF AURORAL NO PROFILES

INTRODUCTION

We have performed a study to determine the feasibility of measuring the enhanced NO profile in an auroral environment by rocket-borne photometer observations of the continuum emission from the  $\text{NO} + \text{O} \rightarrow \text{NO}_2 + h\nu$  reaction. The work was originally motivated by a requirement for additional experiments to be carried on board a multi-instrumented rocket flown into the aurora.

The idea is basically to measure, as a function of altitude, the continuum emission, in a specified wavelength band, with a horizontal-viewing photometer. These measurements, combined with in situ data on the O concentration (from a mass spectrometer) and the known 2-body rate constant for the continuum reaction, should be sufficient, under certain conditions, to infer an NO profile.

The results of the study are presented in this appendix. They provide two specific wavelength bands in which, for an enhanced NO concentration, the continuum emission should sufficiently dominate the background noise to render the experiment feasible.

The basic problem is to find suitable wavelength regions for which the continuum emission will not be masked by background noise from starlight + zodiacal light + diffuse galactic light + auroral-induced air fluorescence. This problem is first addressed.

## CONTAMINATION RADIATION

### Air Fluorescence

Unfortunately, most wavelength regions of interest for this experiment are profusely populated by air lines and bands that can be excited by the drizzle precipitation. Two regions that are relatively clean, however, are (5025Å-5075Å) and (4750Å-4850Å). This can be seen, for example, from References 29 and 30, and from a survey of atomic and molecular band tables. It is for these two spectral regions that we have done our calculations. The following table shows the principal bands that fall within the two regions.

Table C-1. Fluorescence bands in two wavelength regions.

Wavelength Region	Interfering Bands
5025Å-5075Å	$N_2(1P; 10, 4; 5068\text{Å})$ $N_2(1P; 11, 5; 5045\text{Å})$ $N_2(1P; 12, 6; 5022\text{Å})$ $N_2(2P; 0, 6; 5032\text{Å})$ $N_2(2P; 3, 10; 5067\text{Å})$ $N_2(VK; 7, 19; 5030\text{Å})$ $N_2(VK; 0, 14; 5061\text{Å})$ $N_2^+(1N; 2, 5; 5077\text{Å})$ (degraded to violet)
4750Å-4850Å	$N_2(VK; 2, 15; 4837\text{Å})$ $N_2(VK; 5, 17; 4770\text{Å})$ $N_2(2P; 2, 8; 4813\text{Å})$

We have calculated the volume emission rate from these bands using the following formulae:

$$\dot{\Phi}(1P; v, v'') = \frac{q_{v, v''}^{(1)}}{(\lambda_{v, v''}^{(1)})^3 \sum_v [q_{v, v''}^{(1)} / (\lambda_{v, v''}^{(1)})^3]} \left\{ 2.9 q_{v, v''}^{(1)} + \sum_v \frac{q_{v, v''}^{(2)} q_{v, v''}^{(1)}}{(\lambda_{v, v''}^{(2)})^3 \sum_v [q_{v, v''}^{(2)} / (\lambda_{v, v''}^{(2)})^3]} \right\} \dot{P}[N_2(C)] \quad (C-1)$$

$$\dot{\Phi}(2P; v, v'') = \frac{q_{v, v''}^{(2)} q_{v, v''}^{(1)}}{(\lambda_{v, v''}^{(2)})^3 \sum_v [q_{v, v''}^{(2)} / (\lambda_{v, v''}^{(2)})^3]} \dot{P}[N_2(C)] \quad (C-2)$$

$$\dot{\Phi}(VK; v, v'') = \frac{2.9 q_{v, v''}^{(3)}}{(\lambda_{v, v''}^{(3)})^3 \sum_v [q_{v, v''}^{(3)} / (\lambda_{v, v''}^{(3)})^3]} \left\{ 1.15 q_{v, v''}^{(3)} + \sum_v \frac{q_{v, v''}^{(1)} q_{v, v''}^{(3)}}{(\lambda_{v, v''}^{(1)})^3 \sum_v [q_{v, v''}^{(1)} / (\lambda_{v, v''}^{(1)})^3]} \right\} \dot{P}[N_2(C)] \quad (C-3)$$

$$\dot{\Phi}(1N; v, v'') = \frac{q_{v, v''}^{(4)} q_{v, v''}^{(1)}}{(\lambda_{v, v''}^{(4)})^3 \sum_v [q_{v, v''}^{(4)} / (\lambda_{v, v''}^{(4)})^3]} \dot{P}[N_2^+(B)] \quad (C-4)$$

Here the  $q^s$  are Franck Condon factors referring to the following electronic transitions in  $N_2$  and  $N_2^+$ .

$$\begin{array}{ll} q^{(1)}(C^3\Pi_u \rightarrow X^1\Sigma_g^+) & ; \quad q^{(2)}(C^3\Pi_u \rightarrow B^3\Pi_g) \\ q^{(2)}(B^3\Pi_g \rightarrow X^1\Sigma_g^+) & ; \quad q^{(3)}(A^3\Sigma_u^+ \rightarrow X^1\Sigma_g^+) \\ q^{(3)}(B^3\Pi_g \rightarrow A^3\Sigma_u^+) & ; \quad q^{(4)}(N_2^+(B) \rightarrow N_2(X)) \\ & ; \quad q^{(4)}(N_2^+(B) \rightarrow N_2^+(X)) \end{array}$$

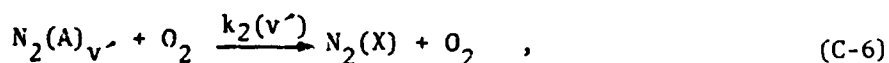
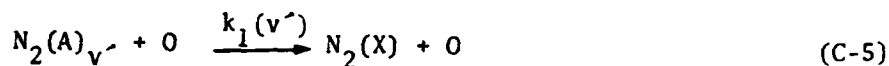
and  $\dot{P}[N_2(C)]$  and  $\dot{P}[N_2^+(X)]$  are the volume production rates of  $N_2(C^3\Pi_u)$  and  $N_2^+(X^2\Sigma_g^+)$ , respectively, by electron bombardment. In Equation C-1, the second term in brackets is the contribution to 1P radiation from C→B cascade. In Equation C-3, the second term in brackets is the contribution to VK emission from B→A cascade. Furthermore, Equations C-1 and C-3 assume (from the ARCTIC code) that

$$\dot{P}[N_2(A^3\Sigma)] \approx 1.15 \dot{P}[N_2(B^3\Pi)]$$

and

$$\dot{P}[N_2(B^3\Pi)] \approx 2.9 \dot{P}[N_2(C^3\Pi)] .$$

The volume emission rate from the Vegard Kaplan bands, represented by Equation C-3, should be reduced to allow for quenching of the A state by atomic and molecular oxygen. Specifically, if the quenching reactions assumed are



then the VK emission should be reduced by the factor, F, where

$$F = \left\{ 1 + \frac{k_1(v')[O] + k_2(v')[O_2]}{\sum_v A_{v'v}} \right\}^{-1} . \quad (C-7)$$

Here,  $A_{v'v}$  is the Einstein transition probability. Since rate constants for quenching of individual vibrational states of  $N_2(A)$  are not known, we use instead the overall rate constants  $k_1$  and  $k_2$  and then approximate Equations C-7 by

$$F \approx \left\{ 1 + (k_1[O] + k_2[O_2])\tau \right\}^{-1} \quad (C-8)$$

where  $\tau$  is the radiative lifetime of the A state ( $\approx 2$  sec). Values for  $k_1$  and  $k_2$  are taken equal to  $1.5 \times 10^{-11}$  and  $6.5 \times 10^{-12} \text{ cm}^3 \text{ sec}^{-1}$ , respectively (References 31, 32, 2 (footnote on p. 108)).

The volume emission rate due to air fluorescence was calculated using the foregoing equations along with the volume production rates  $\dot{P}(\text{N}_2(\text{C}))$  and  $\dot{P}(\text{N}_2^+(\text{B}))$  determined by the ARCTIC code for the drizzle flux shown in Figure 2-8 of Reference 2. The intensity of the air fluorescence was then calculated by integrating the volume emission rate along lines of sight (spherical earth), assuming an unlimited extent of the drizzle region.

#### Starlight + Zodiacal Light + Diffuse Galactic Light

A summary of the contribution from these sources is given in Reference 33, p. 134. We have used the value  $0.7 \text{ R}/\text{\AA}$ . This includes  $0.35 \text{ R}/\text{\AA}$  for the mean sky background due to faint stars. However, on March 21 near midnight at Poker Flat, the galactic pole is at a zenith angle of about  $52^\circ$  toward the north, and the galactic equator (Milky Way) is below the horizon. Thus the value of  $0.35 \text{ R}/\text{\AA}$  is probably too large, especially for sight paths to the north, and our value of  $0.7 \text{ R}/\text{\AA}$  is likely an upper limit.

#### EMISSION FROM NO + O CONTINUUM

At altitudes above about 95 to 100 km, the reaction between NO and O that produces the air afterglow continuum is essentially bimolecular (References 34, 35) with a rate constant over the bands of interest of about  $1 \times 10^{-21} \text{ cm}^3 \text{ sec}^{-1} \text{\AA}^{-1}$ . With this rate constant, the volume emission rate from the continuum was computed for the two wavelength bands using the two different NO profiles shown in Figure 2-11 of Reference 2. One of them corresponds to a "typical" low latitude profile; the other, to the profile inferred for the 1973 Multi event.

## RESULTS

The results are shown in Figures C-1 through C-3. Figure C-1 compares the continuum radiance along a horizontal path with the total background due to air fluorescence + starlight etc. for the 5025Å-5075Å band. About half of the background emission is seen to come from the extra-terrestrial sources. The important point to notice, however, is that if the NO is enhanced as much as assumed, the afterglow continuum should dominate the background by an order of magnitude below 100 km altitude and fall off with increasing altitude much more rapidly than does the background intensity. These two effects should be observable. However, if the NO is not enhanced, but corresponds more to the low-latitude profile, the continuum emission should be masked by the background which should remain fairly constant in intensity with increasing altitude to at least 115 or 120 km.

Figure C-2 is a corresponding comparison, also for the 5025Å-5075Å band, for a vertical sight path rather than a horizontal one. It is clear from this figure that the background emission (mainly extraterrestrial) dominates the afterglow continuum at almost all altitudes, even for the enhanced NO profile. Thus, zenith measurements are clearly inappropriate for purposes of this experiment.

Figure C-3 is another comparison for horizontal sight paths but for the wavelength band 4750Å-4850Å. Also shown in this figure is the computed 3914Å intensity along the same horizontal paths (this curve applies, of course, also to Figure C-1).

Comparison between Figures C-1 and C-3 shows that there is no great advantage of one wavelength band over the other. The wider band provides a greater intensity (factor of 2) for the continuum, but the afterglow intensity drops to background at a slightly lower altitude.

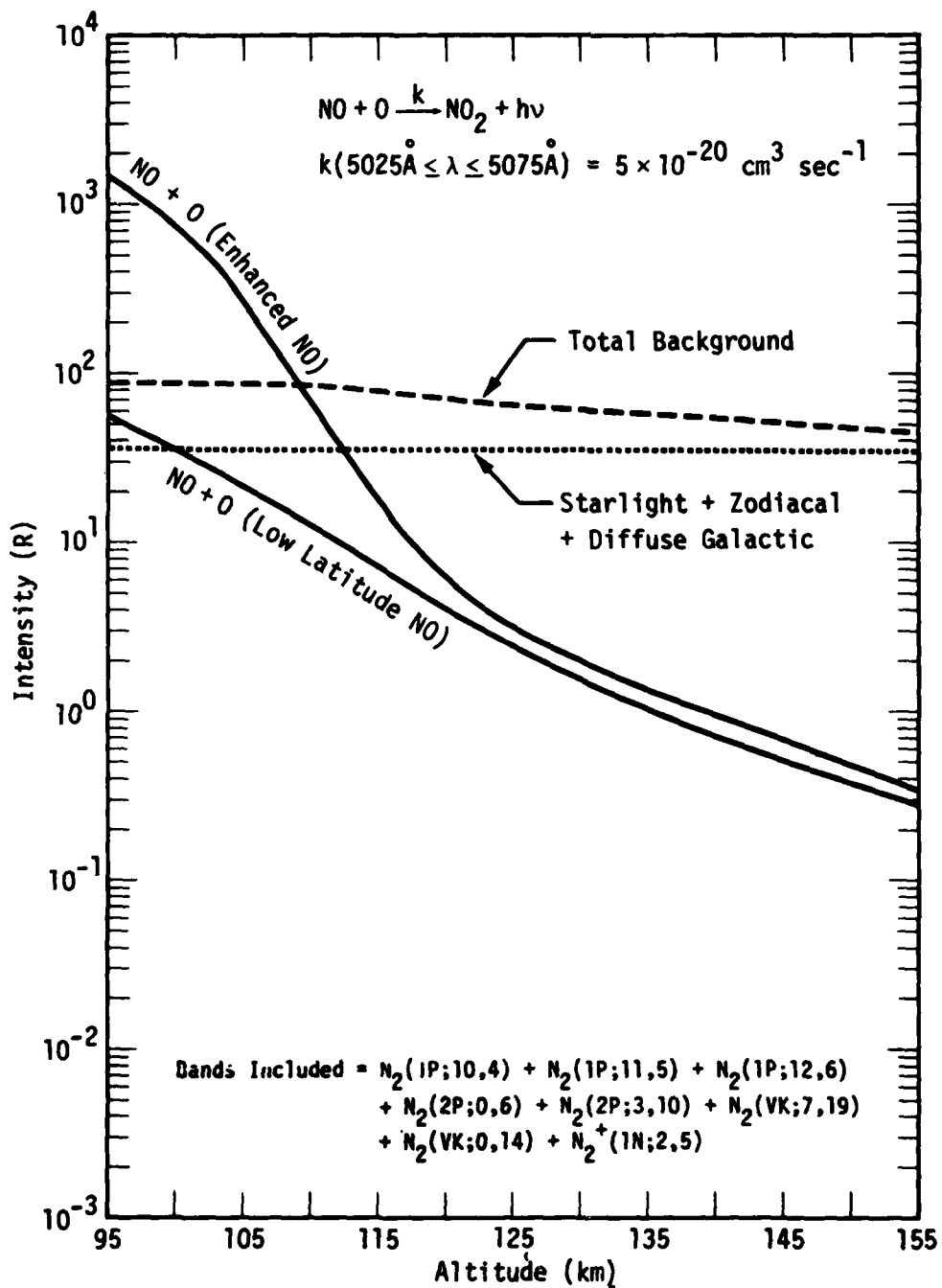


Figure C-1. Calculated intensity in  $5025\text{\AA} \leq \lambda \leq 5075\text{\AA}$  band from  $\text{NO} + \text{O} \rightarrow \text{NO}_2 + h\nu$  continuum compared with auroral drizzle-induced fluorescence from  $\text{N}_2(\text{VK}) + \text{N}_2(1\text{P}) + \text{N}_2(2\text{P})$  bands + starlight + zodiacal light + galactic light (horizontal path).

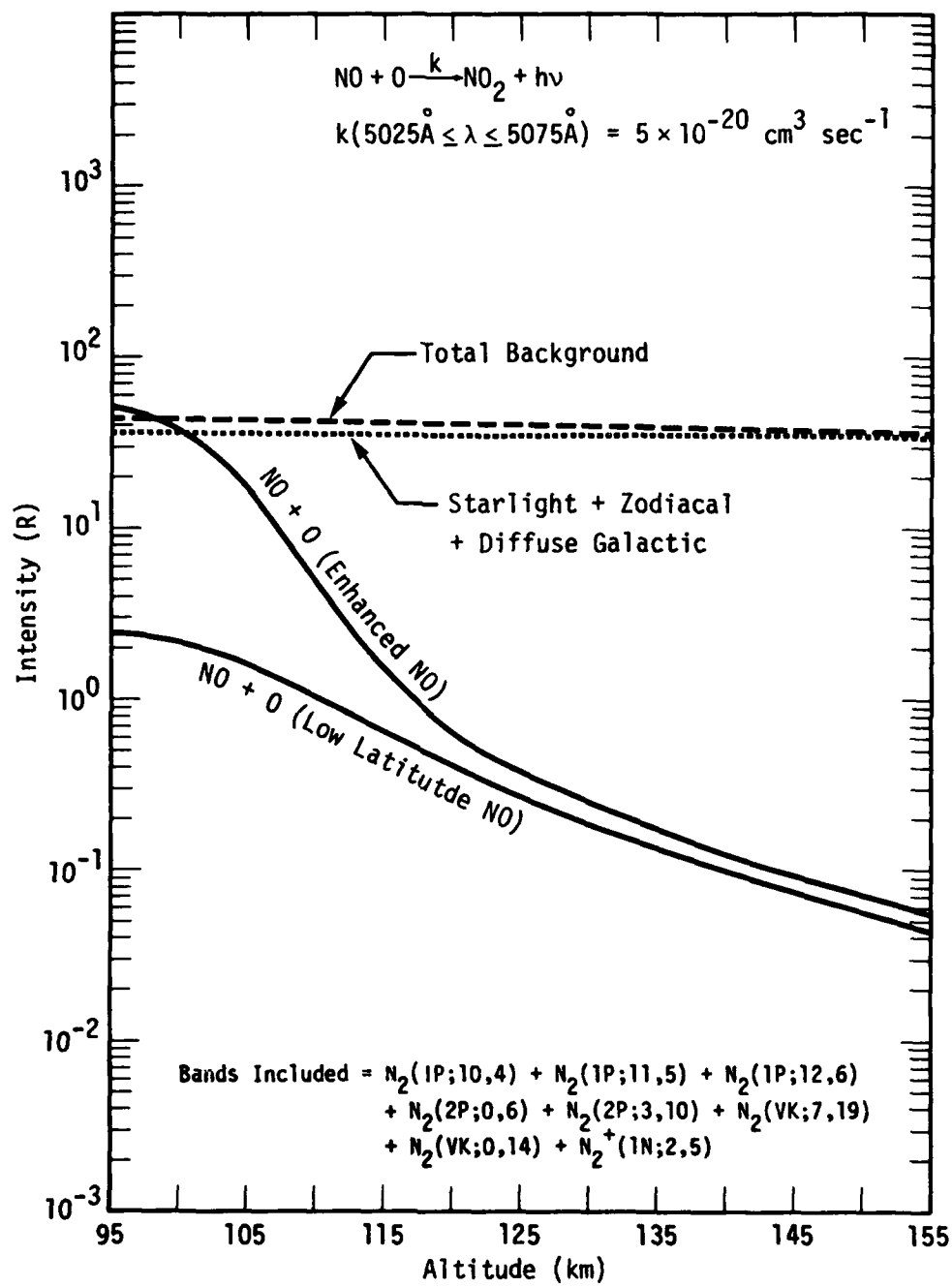


Figure C-2. Calculated intensity in  $5025\text{\AA} \leq \lambda \leq 5075\text{\AA}$  band from  $\text{NO} + \text{O} \rightarrow \text{NO}_2 + h\nu$  continuum compared with auroral drizzle-induced fluorescence from  $\text{N}_2(\text{VK}) + \text{N}_2(1\text{P}) + \text{N}_2(2\text{P})$  bands + starlight + zodiacal light + diffuse galactic light (vertical path).

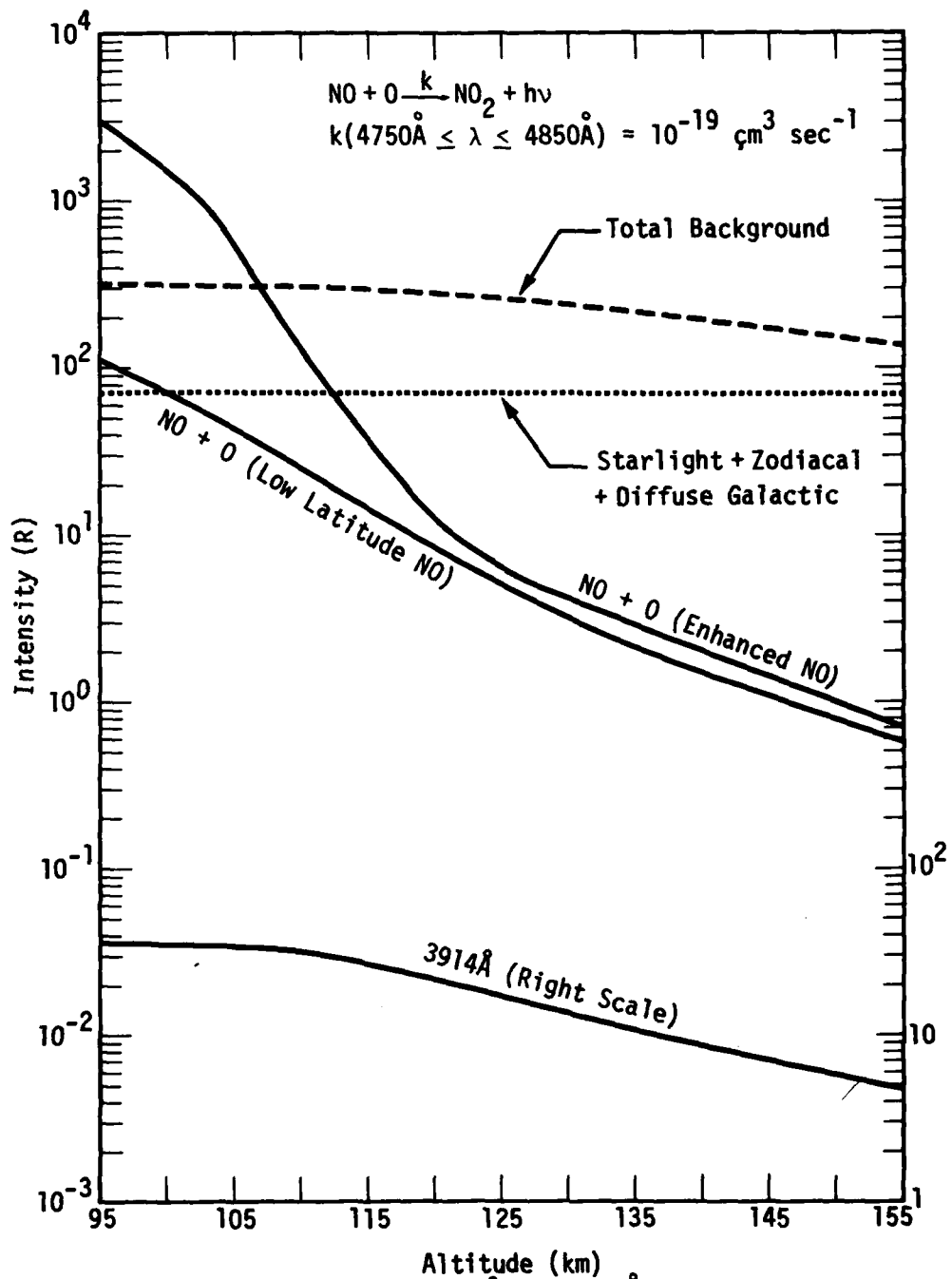


Figure C-3. Calculated intensity in  $4750\text{\AA} \leq \lambda \leq 4850\text{\AA}$  band from  $\text{NO} + \text{O} \rightarrow \text{NO}_2 + h\nu$  continuum compared with auroral drizzle-induced fluorescence from  $\text{N}_2(\text{VK}; 2, 15) + \text{N}_2(\text{VK}; 5, 17) + \text{N}_2(2\text{P}; 2, 8) + \text{starlight} + \text{zodiacal light} + \text{galactic light (horizontal path)}$ .

## CONCLUSIONS

The foregoing considerations suggest that the experiment has merit. However, success would depend on the availability of filters in the appropriate wavelength regions with adequate out-of-band rejection. These are items that we have not addressed.

## DISTRIBUTION LIST

### DEPARTMENT OF DEFENSE

Director  
Defense Advanced Resch. Proj. Agency  
ATTN: LTC W. A. Whitaker  
ATTN: STO, Captain J. Justice  
ATTN: Major Gregory Canavan

Defense Documentation Center  
Cameron Station  
12 cy ATTN: TC

Director  
Defense Nuclear Agency  
ATTN: TISI, Archives  
3 cy ATTN: TITL, Tech. Library  
ATTN: RAEV, Harold C. Fitz, Jr.  
3 cy ATTN: RAAE, Charles A. Blank  
ATTN: DDST

Dir. of Defense Resch. & Engineering  
Department of Defense  
ATTN: S&SS (OS)

Commander  
Field Command  
Defense Nuclear Agency  
ATTN: FCPR

Chief  
Livermore Division, Field Command, DNA  
Lawrence Livermore Laboratory  
ATTN: FCPRL

### DEPARTMENT OF THE ARMY

Commander/Director  
Atmospheric Sciences Laboratory  
US Army Electronics Command  
3 cy ATTN: DRSEL-BL-SY-S

Commander  
Harry Diamond Laboratories  
2 cy ATTN: DRXDO-NP

Commander  
US Army Nuclear Agency  
ATTN: MONA-WE

Commander  
US Army Foreign Science & Tech. Center  
ATTN: R. Jones

### DEPARTMENT OF THE NAVY

Chief of Naval Research  
Navy Department  
ATTN: Code 461

Commander  
Naval Ocean Systems Center  
ATTN: Code 2200, Ilan Rothmuller

Officer in Charge  
Naval Surface Weapons Center  
ATTN: Code WA501, Navy Nuc. Prgms. Off.

### DEPARTMENT OF THE NAVY (Continued)

Director  
Naval Research Laboratory  
ATTN: Code 7700, Timothy P. Coffey  
ATTN: Code 2600, Tech. Lib.  
ATTN: Code 7701, Jack D. Brown  
ATTN: Code 7750, Wahab Ali  
ATTN: Douglas P. McNutt  
ATTN: Code 7750, Paul Julienne  
ATTN: Code 7127, Charles Y. Johnson  
ATTN: Code 7750, Darrell F. Strobel

### DEPARTMENT OF THE AIR FORCE

AF Geophysics Laboratory, AFSC  
5 cy ATTN: OPR, Alva T. Stair  
5 cy ATTN: LKB, Kenneth S. W. Champion  
5 cy ATTN: OPR-I, J. Ulwick  
2 cy ATTN: OPR-I, R. Murphy  
ATTN: LKD, R. Narcisi  
ATTN: OPR-I, J. Kennealy

AF Weapons Laboratory, AFSC  
ATTN: DYT  
ATTN: SUL

Commander  
ASD  
ATTN: ASD-YH-EX, Lt Col Robert Leverette

SAMSO/SZ  
ATTN: SZJ, Major Lawrence Doan

### ENERGY RESEARCH & DEVELOPMENT ADMINISTRATION

Division of Military Application  
US Energy Resch. & Dev. Admin.  
ATTN: Doc. Con. for Major D. A. Haycock

Los Alamos Scientific Laboratory  
ATTN: Doc. Con. for R. A. Jeffries

### OTHER GOVERNMENT AGENCY

Department of Commerce  
Office of Telecommunications  
Institute for Telecom Science  
ATTN: William F. Utlaut

### DEPARTMENT OF DEFENSE CONTRACTORS

AeroDyne Research, Inc.  
ATTN: F. Bien  
ATTN: M. Camac

Aerospace Corporation  
ATTN: Harris Mayer  
ATTN: Thomas D. Taylor  
ATTN: R. D. Rawcliffe  
ATTN: R. Grove  
3 cy ATTN: R. J. McNeal

DEPARTMENT OF DEFENSE CONTRACTORS (Continued)

University of Denver  
Colorado Seminary  
Denver Research Institute  
ATTN: Sec. Officer for Mr. Van Zyl  
ATTN: Sec. Officer for David Murcray

General Electric Company  
TEMPO-Center for Advanced Studies  
ATTN: Warren S. Knapp  
5 cy ATTN: DASIAC

General Research Corporation  
ATTN: John Ise, Jr.

Geophysical Institute  
University of Alaska  
ATTN: T. N. Davis  
3 cy ATTN: Neal Brown

Honeywell Incorporated  
Radiation Center  
ATTN: W. Williamson

Institute for Defense Analyses  
ATTN: Hans Wolfhard  
ATTN: Ernest Bauer

Lockheed Missiles & Space Company, Inc.  
ATTN: Robert D. Sears, Dept. 52-14  
ATTN: J. B. Reagan, D/52-12  
ATTN: Billy M. McCormac, Dept. 52-54  
ATTN: John Kumer  
ATTN: John B. Cladis, Dept. 52-12  
ATTN: Tom James  
ATTN: Martin Walt, Dept. 52-10  
ATTN: Richard G. Johnson, Dept. 52-12

Mission Research Corporation  
ATTN: P. Fischer  
ATTN: M. Scheibe  
ATTN: D. Sappenfield  
10 cy ATTN: D. Archer  
ATTN: Paul W. Tarr

Photometrics, Inc.  
ATTN: Irving L. Kofsky

Physical Dynamics, Inc.  
ATTN: Joseph B. Workman

Physical Sciences, Inc.  
ATTN: Kurt Wray

R & D Associates  
ATTN: Robert E. Lelevier  
ATTN: Forrest Gilmore

DEPARTMENT OF DEFENSE CONTRACTORS (Continued)

R & D Associates  
ATTN: Herbert J. Mitchell

The Rand Corporation  
ATTN: James Oakley

Science Applications, Inc.  
ATTN: Daniel A. Hamlin

Space Data Corporation  
ATTN: Edward F. Allen

Stanford Research Institute  
ATTN: M. Baron  
ATTN: Walter G. Chestnut  
ATTN: Ray L. Leadabrand  
ATTN: C. Rino  
ATTN: D. McDaniel

Stanford Research Institute  
ATTN: Warren W. Berning

Technology International Corporation  
ATTN: W. P. Boquist

Utah State University  
ATTN: Doran Baker  
ATTN: D. Burt  
ATTN: Kay Baker  
ATTN: C. Wyatt

VisiDyne, Inc.  
ATTN: J. W. Carpenter  
ATTN: Henry J. Smith  
ATTN: L. Katz  
ATTN: T. C. Degges  
ATTN: William Reidy  
ATTN: Charles Humphrey